Testing and analysing the material properties of 316L-CuCrZr multi-material manufactured by laser powder bed fusion

Materials Engineering/Faculty of Technology
Master's thesis
Department of Mechanical and Materials Engineering

Author:
Olivia Iizuka

7.12.2025
Turku

The originality of this thesis has been checked in accordance with the University of Turku quality assurance system using the Turnitin Originality Check service.

Master's thesis

Subject: Materials engineering
Author: Olivia Iizuka
Title: Testing and analysing material properties of 316L-CuCrZr multi-material manufactured by laser powder bed fusion
Supervisors: Professor Antti Salminen, D.Sc.(Tech.); Associate Professor Ashish Ganvir, PhD; Associate Professor Milica Todorovic, D.Phil
Advisors: Senior research scientist Heidi Piili, D.Sc.(Tech.); Postdoctoral researcher Nikhil Kamboj, D.Sc(Tech); Assistant professor Mohsen Amraei, PhD
Number of pages: 93
Date: 7.12.2025

Laser powder bed fusion of metals (PBF-LB/M) is a method of additive manufacturing (AM), also known as industrial 3D printing, where metal powder is melted and fused into a solid metal layer by layer. PBF-LB/M is a promising technology in the field of multi-material manufacturing, where components are manufactured with two or more discrete materials. Multi-material AM shows potential in applications where complex geometries are used to optimise the function of the manufactured component. This thesis researches the suitability of 316L stainless steel and CuCrZr alloy in multi-material PBF-LB/M. It provides information on the suitable parameters for PBF-LB/M and post-processing of CuCrZr-316L multi-material. The thesis consists of a literature review and the experimental part. The literature review provides information on the properties and behaviour of the studied materials, and data on the suitable PBF-LB/M, post-processing and material testing parameters and procedures for 316L-CuCrZr multi-material. The experimental part was used to evaluate the material properties of as-built and post-processed PBF-LB/Med 316L-CuCrZr by conducting several material property tests, including: metallographic analysis, microhardness testing, geometrical accuracy measurements, corrosion resistance testing, and thermal and electrical conductivity testing.

The experimental part revealed information about the different material properties and defects, such as cracking and porosity of 316L-CuCrZr manufactured with varying PBF-LB/M and post-process parameters. The metallographic analysis found information on the mixing and bonding of 316L-CuCrZr material during the PBF-LB/M process. Heat treatment was revealed to cause cracking in the 316L-CuCrZr interface, due to differences in thermal expansion coefficients between the discrete materials. The heat-treatment was also observed to increase the microhardness, corrosion rate and thermal conductivity of the 316L-CuCrZr. The increase of microhardness and material conductivity was hypothesised to be a result of precipitation in CuCrZr, whereas the corrosion rate was suspected to have increased due to changed corrosion potential values of the discrete 316L and CuCrZr and the cracking in the 316L-CuCrZr interface. The geometry of the multi-material revealed marginal misalignment between the 316L and CuCrZr geometries, which was most likely caused by horizontal tilting of the 316L material during the material changing in the PBF-LB/M process. Therefore, the thesis was able to research the PBF-LB/M of 316L-CuCrZr multi-material by gathering data on the PBF-LB/M parameters, post-processing and their effect on the material properties of the 316L-CuCrZr multi-material through literature research and empirical experimentation.

Keywords: Additive manufacturing, laser powder bed fusion, multi-material, bimetallic additive manufacturing, 316L, CuCrZr, heat treatment, material

Table of contents

Nomenclature

Abbreviation	Explanation
AM	Additive manufacturing
CAD	Computer-aided design
CCC	Copper contamination cracking
DAH	Direct age hardening
EDS	Energy dispersive X-ray spectroscopy
HT1	Heat treatment done at 370-500 °C for 3.5h
HT2	Heat treatment done at 500 °C for 1.5h
PBF/M	Powder bed fusion of metals
PBF-EB/M	Electron beam powder bed fusion of metals
PBF-LB/M	Laser beam powder bed fusion of metals
SEM	Scanning electron microscope

Symbol	Unit	Explanation
A	mm2	Area
d	mm	Depth
defect-%	%	Defect percentage
E	V	Potential
Ecorr	V	Natural corrosion potential
F	N	Force
HV	HV	Vickers hardness
I	A	Electrical current

Icorr	µA/cm2	Corrosion current density
L	ΩWK^-2	Lorenz number
l	mm	Length
LED	J/mm	Linear energy deposition
OCP	V	Open circuit potential
P	W	Laser power
R	Ω	Electrical resistance
T	K	Room temperature
v	mm/s	Scanning speed
w	mm	Width
wt.-%	%	Weight percentage
λ	W/mK	Thermal conductivity
ρ	Ωm	Electrical resistivity
σ	S/m	Electrical conductivity

1 Introduction

1.1 Background and motivation

Additive manufacturing (AM), also known as industrial 3D printing, is a technology that manufactures products by adding material layer by layer to form a desired shape. AM has mainly been utilised in prototype manufacturing, as it enables rapid on-site production of components based on computer-aided design (CAD) models. AM methods and techniques have increasingly become a subject of scientific research and development, for their potential in wider industrial applications (Javaid et al., 2021). One reason for the growing interest in AM is its ability to manufacture components of complex geometries, which would be challenging or impossible to achieve using subtractive manufacturing methods, such as machining (Javaid et al., 2021). AM also enables the reduction of material waste compared to the other aforementioned manufacturing methods (Javaid et al., 2021). AM has been proven to be applicable in automotive, medical, defence, and aviation industries and many other fields of technology (Javaid et al., 2021).

AM technology includes a wide range of production methods and techniques, which can be used to manufacture materials, such as metals, polymers and even some ceramics and composites (Wang et al., 2022). One of the most widely used AM methods is powder bed fusion (PBF), which is commonly associated with AM of metals. In metal PBF (PBF/M), a metal powder is selectively melted layer-by-layer according to the sliced digital CAD model (Wei et al., 2020). The selective melting in the PBF/M processes is commonly conducted using an electron or laser beam, which corresponds to processes called electron beam-based powder bed fusion (PBF-EB/M) and laser beam-based powder bed fusion (PBF-LB/M), respectively (Wei et al., 2020).

In recent years, research in applying PBF-LB/M in multi-material manufacturing, or manufacturing components of more than one material, has increased (Wang et al., 2022). The multi-material AM would enable the production of more complex and optimised geometries, as well as increase control of adding different desired material properties in strategic locations of the component (Wang et al., 2022). Optimally, this strategic distribution of the various materials within the manufactured component enables better performance than single-material parts, whose performance depends mainly on the properties of the one material needed to satisfy all the needed requirements (Wang et al., 2022).

One of the most researched AMed multi-materials combines stainless steel and copper alloys such as 316L and CuCrZr. 316L is a low-carbon stainless steel known for its high tensile strength and yield strength combined with corrosion resistance (Sharma et al., 2024). In contrast, the copper alloy CuCrZr is known for its high thermal conductivity, as well as excellent wear resistance and good mechanical strength retention in extremely high temperatures (Meyer et al., 2025). The 316L-CuCrZr multi-material is especially beneficial in heat management applications (Martendal et al., 2024). AM allows fabrication of geometries which allow the most optimal heat dissipation (Martendal et al., 2024). The supporting and protective sections of a heat management component could be fabricated with hard, ductile and corrosion-resistant materials such as 316L stainless steel (Martendal et al., 2024). Whereas, the sections required to conduct heat can be manufactured with CuCrZr or other highly conductive alloys (Martendal et al., 2024).

1.2 Objective and scope of research

The thesis was carried out as part of a collaborative Bimetallic research project between the University of Turku, Wärtsilä, Valmet, Bluefors, Patria, and EOS. The project and the thesis aimed to gather a comprehensive perspective on the AM of the 316L stainless steel and CuCrZr copper alloy. The thesis brings scientific relevance by building a foundation for further research and development of PBF-LB/M-based multi-material production and provides insight into the properties of the PBF-LB/Med 316L-CuCrZr multi-material. The thesis discusses methods of manufacturing, post-processing, sample preparation and material testing methods found suitable for the PBF-LB/Med 316L-CuCrZr, which can be used as guides for future research.

The thesis brings industrial relevance by providing a comprehensive information package of PBF-LB/M and its application in multi-material manufacturing. The thesis can also be used to learn about 316L and CuCrZr materials and their suitability and performance in multi-material PBF-LB/M. For companies interested in applying multi-material AM, this thesis can work as a guide to learn about the risks, challenges and benefits of the PBF-LB/Med 316L-CuCrZr multi-material. It also discusses recommendations on the optimisation process of the PBF-LB/M process parameters and post-processes for the 316L-CuCrZr multi-material.

1.3 Research methods and limitations

The thesis is composed of a literature review and an experimental part. The literature review provides an introduction to the 316L and CuCrZr materials, their properties and common

applications in the AM context and outside of it. The literature review also discusses the methods and techniques of 316L-CuCrZr multi-material PBF-LB/M, post-processing, and material testing.

The experimental part is divided into three stages: preliminary PBF-LB/M parameter optimisation testing, PBF-LB/M and post-processing 316L-CuCrZr multi-material parts for material tests and testing different properties of PBF-LB/Med 316L-CuCrZr multi-material, through tests including:

- Metallographic analysis
- Microhardness
- Geometrical accuracy
- Corrosion resistance
- Thermal conductivity

However, further research on the properties of the PBF-LB/Med 316L-CuCrZr multi-material is still necessary. Due to limitations on time and resources, the following material tests were ruled out of the scope of this thesis:

- Dilatometry
    - Ruled out due to difficulties in sample manufacturing and the unavailability of testing machinery.
- Tensile testing
    - Ruled out due to resource limitations, restricting the manufacturing of samples with the required dimensions.
- Wear resistance testing
    - Ruled out due to time restrictions.
- Scanning electron microscopy (SEM) and energy-dispersive X-ray spectroscopy (EDS)
    - Not in the original material testing plan, but would have provided valuable information on the microstructure of the studied multi-material.

1.4 Research questions

The thesis aims to answer the following research questions:

- What does the microstructure and the interface bonding look like in PBF-LB/Med 316L-CuCrZr? What aspects in the PBF-LB/M and post-processing cause the creation of defects in 316L-CuCrZr?
    - Motivation: Microstructure, defects and material bonding between the discrete metals affect the material properties, such as hardness, corrosion resistance and thermal conductivity. (*Metallographic Procedures and Analysis – A Review*, n.d.).
- What are the hardnesses of the PBF-LB/Med 316L-CuCrZr multi-material, and how are they affected by heat treatment?
    - Motivation: Material hardness is an important indicator of the strength of the material by means of resisting mechanical deformation or stress and thus indicates the overall performance of the material in service. (Sundararajan & Roy, 2001)
- What are the corrosion tendencies and corrosion rates of the PBF-LB/Med 316L bulk, CuCrZr bulk and 316L-CuCrZr multi-material, and does heat treatment affect them?
    - Motivation: Corrosion testing provides valuable information on the suitability of the 316L-CuCrZr multi-material in applications where it might be exposed to corrosive environments. (*2019 Department of Defense -Allied Nations Technical Corrosion Conference COMPUTATIONAL CORROSION ANALYSIS GUIDES MATERIAL CHOICE FROM DESIGN THROUGH SUSTAINMENT*, n.d.)
- How accurately does the used PBF-LB/M process manufacture the 316L-CuCrZr material component when compared to the CAD? Does the material change cause an offset in the interface?
    - Motivation: Geometrical accuracy measurements provide information on the manufacturing challenges in multi-material AM, including the effect of material changing during the PBF-LB/M process. (Merz et al., 2023)

- How does heat treatment affect the thermal conductivity of the PBF-LB/Med 316L-CuCrZr?
    - Research on thermal conductivity provides information on the suitability of the 316L-CuCrZr multi-material for heat management applications. (Jadhav et al., 2021)

2 Properties and applications of AMed 316L, CuCrZr and 316L-CuCrZr

2.1 AMed 316L

The 316L stainless steel, also known as 1.4404 and X2CrNiMo17-12-2, is one of the most widely studied austenitic stainless-steel materials (Huang et al., 2022). 316L is well known for its properties, including high resistance to corrosion and oxidation due to its adherent chromium-rich surface film (Sharma et al., 2024). It also exhibits well-balanced mechanical properties such as good ductility, yield strength and plasticity even at high temperatures (Vukkum & Gupta, 2022). Therefore, 316L is usually applied in situations where a long-lasting, high corrosion resistance, especially to acids, chlorine, and hydrogen, is required at a relatively low financial cost (Sharma et al., 2024). These properties are often needed in marine, automotive, pharmaceutical, food processing and chemical industries, as well as in general transportation and biomedical parts (Laleh et al., 2023; Meyer et al., 2025; Sharma et al., 2024). 316L is commonly used in heat exchangers, chemical production and food processing despite its low thermal conductivity (Huang et al., 2022; Laleh et al., 2023).

AMed 316L parts have been experimented with functional applications in biomedical implants as well as engine and nuclear reactor components (Huang et al., 2022; Lodhi et al., 2019; Salman et al., 2019). PBF-LB/Med 316L has also been found to exhibit strength and ductility, which is able to exceed conventionally manufactured 316L. This is suspected to be a result of the unique microstructural aspects, such as the fine grain structure, the fine intergranular dendrite microstructure and high density of low-angle grain boundaries and dislocations, created by the rapid heating-cooling cycles. Li et al. (2023) observed the formation of a columnar grain structure with irregular equiaxed grains containing high amounts of cellular and fibre sub-structures, which were caused by rapid cooling of the molten pool (Li et al., 2023). These microstructures caused the strengthening effect, especially in the build direction. For instance, the yield strength and the ultimate tensile strength of the AMed sample (484 MPa and 627 MPa) outperformed the forged sample (305 MPa and 601 MPa) (Li et al., 2023).

2.2 AMed CuCrZr

CuCrZr is a precipitation hardening copper alloy. Precipitation hardening is a heat treatment method aiming to produce precipitates in the material microstructure, which increases or decreases different material properties based on the size and phase of the precipitation (Kuai et al., 2022; Tang, Chen, Sun, Liu, et al., 2022). In CuCrZr, the Cu_xZr_y, Cr- and Zr-rich precipitates grow to 2.2-47 nm depending on the type of heat treatment (Salvan et al., 2021; Tang, Chen, Sun, Liu, et al., 2022). Similar to other copper alloys, CuCrZr exhibits excellent thermal and electrical conductivity and reflectivity (Tang, Chen, Sun, Liu, et al., 2022). Additionally, CuCrZr has good mechanical properties, including yield strength and hardness (Salvan et al., 2021). CuCrZr is often used in applications where high thermal conductivity is required in extreme environments (Tang, Chen, Sun, Liu, et al., 2022). These applications include the components of combustion chambers and liquid rocket engines, as well as heat exchangers (Kuai et al., 2022; Salvan et al., 2021; Tang, Chen, Sun, Liu, et al., 2022).

In recent years, research on the PBF-LB/M manufacturing of CuCrZr alloy has increased due to the large potential for CuCrZr parts to fill the demand for complex and functional integrated designs in aerospace and other industrial components in the aforementioned applications (Kuai et al., 2022). However, the high reflectivity of the CuCrZr causes low absorption of thermal energy of the laser beam, thus increasing the chance of inefficient melting and a risk of damage to the PBF-LB/M machines (Tang, Chen, Sun, Liu, et al., 2022). The high thermal conductivity of the CuCrZr leads to high thermal gradients and fast heat dissipation in the previously melted material, which makes the melting and solidification process and the resulting metallographic quality challenging to control (Kuai et al., 2022; Tang, Chen, Sun, Liu, et al., 2022). Therefore, the PBF-LB/Med CuCrZr components have poor mechanical properties, such as hardness, tensile and yield strength, when compared to conventionally manufactured counterparts (Kuai et al., 2022).

Despite growing interest in AM of CuCrZr, the research on PBF-LB/M of CuCrZr is still in the preliminary stage, as the majority of the research discusses optimisation of the process parameters, such as laser power and scanning speed (Kuai et al., 2022). One challenge pointed out by Kuai et al. (2022) is that the exact properties of PBF-LB/Med CuCrZr are difficult to replicate, as the differences in the PBF-LB/M machine brands and laser sources affect the mechanical properties of the CuCrZr part sensitively. (Kuai et al., 2022). For this reason,

CuCrZr PBF-LB/M processes require some kind of preliminary parameter optimisation process before conducting any type of characterisation (Kuai et al., 2023).

2.3 AMed 316L-CuCrZr

The combination of 316L-CuCrZr alloys is perfect in heat transfer devices, fusion reactors, conformal cooling channels and other cooling components (Kuai et al., 2023; Meyer et al., 2025). In many of the proposed 316L-CuCrZr components, the 316L is used to fabricate structural supports or protective barriers, whereas the CuCrZr sections are manufactured where the rapid heat dispersion is needed (Kuai et al., 2023; Wang et al., 2022). AM technology has enabled a way to enhance these components, as it can form complex structures which would otherwise be difficult or impossible to achieve through traditional manufacturing methods (Wang et al., 2022). For instance, PBF-LB/M has been gradually applied to manufacture finer structures such as thin-walled internal flow channels, which reduces the weight compared to traditionally manufactured counterparts (Meyer et al., 2025). These weight-reducing innovations are essential to produce, for example, fuel-efficient vehicles in the automotive and aerospace industries. (Kuai et al., 2023; Meyer et al., 2025)

The issue with multi-material PBF-LB/M lies in the defects in the interface, the most common of which are cracks and pores (J. Chen et al., 2019). The cracking of the interface of two discrete materials is often considered to be caused by the mismatch of their thermal properties, such as thermal expansion coefficients (Mao et al., 2022). The differences in the material expansion coefficients create stresses that accumulate in the material interface during extreme temperature changes (Mao et al., 2022). Yang et al. (2019) observed cracking in AMed 316L-CuSn10 multi-material, mainly on the side of 316L. The cracking was suspected to be caused by the mismatch of thermal expansion of the two materials, which would, after laser scanning, cause accumulation of residual stresses on the side of 316L near the interface (J. Chen et al., 2019).

Pores are often caused by the improper energy input from the laser scanning process (Wang et al., 2022). Material processing using too high an energy input can cause keyhole porosity by trapping gases inside the melt pool (Wang et al., 2022). Too low energy input can cause incomplete melting of the powder, which leaves the spaces between the powder particles inside the structure, thus creating lack-of-fusion porosity (Wang et al., 2022). As the thermal properties and reflectivities of the 316L and CuCrZr materials are different, the transition of the process energy input during the manufacturing of the interface can cause a mismatch of the

optimal energy inputs for the materials and thus create either keyhole porosity in the 316L side or lack-of-fusion porosity on the CuCrZr side (Wang et al., 2022).

Another aspect contributing to the defect formation in the 316L-CuCrZr interface of the 316L is the natural immiscibility of Fe- and Cu-based materials (Mao et al., 2022). This reluctance of CuCrZr and 316L mixing can be explained by the binary Cu-Fe diagram, which shows that iron and copper can mix in the liquid state but are immiscible upon solidification (Meyer et al., 2025; Zhou et al., 2022) due to their different crystal structures (Han et al., 2017). Figure 1 illustrates the phenomena present during the processing of the 316L-CuCrZr interface (Kuai et al., 2023).

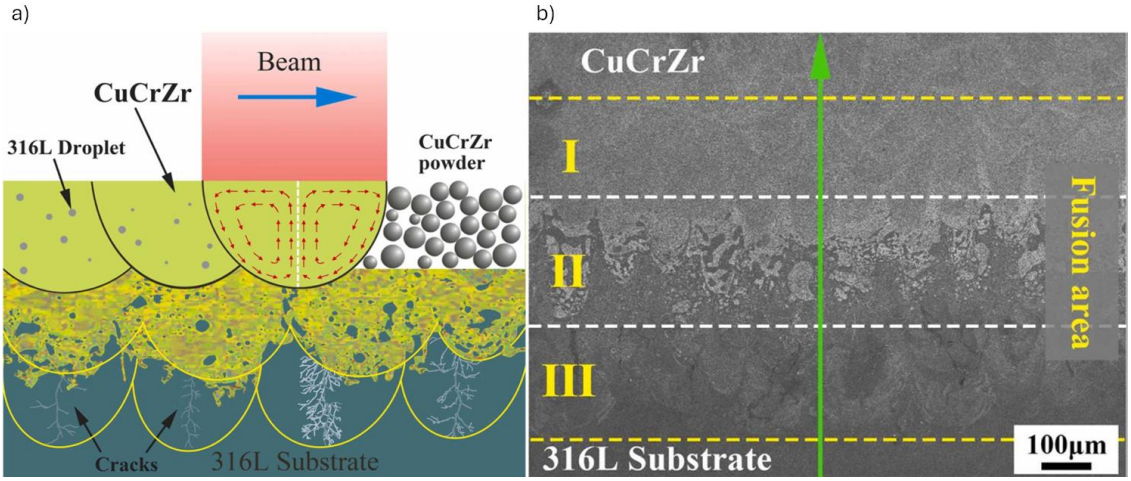

Figure 1. (a) formation mechanism of PBF-LB/Med 316L-CuCrZr (b) regions of 316L-CuCrZr interface. Reproduced and modified from Kuai et al., 2023, which is under an open access Creative Common CC BY licence.

Figure 1 shows how cooling of the liquid 316L-CuCrZr mixture causes the formation of separate Fe- and Cu-rich phases, instead of a new homogenous alloy or a gradiental material change (Kuai et al., 2023). The liquid copper penetrating the steel can increase the risk of the liquid metal embrittlement phenomenon, where a metal, such as stainless steel, loses its ductility after being in contact with another liquid metal, such as molten copper alloy (Wei et al., 2020). This specific type of liquid metal embrittlement can cause copper contamination cracking (CCC) (Deillon et al., 2024). In CCC (see Figure 1a), liquid copper penetrates the grain boundaries of steel, thus leading to intergranular cracking when subjected to high tensile stresses in the steel (Deillon et al., 2024).

Kuai et al. (2023) divided the 316L-CuCrZr interface into three regions, as shown in Figure 1b. Region I consists of CuCrZr with irregular fine Fe-rich phases. Region II marks the transition of 316L to CuCrZr. It consists of island-like Cu-rich areas embedded in the 316L material. These Cu-rich areas consist of large phases reminiscent of the meltpool of CuCrZr that penetrated the 316L substrate and smaller droplet-like phases caused by the material mixing. These Cu-rich phases encase small (radius smaller than 2µm) spherical 316L particles. These particles form when 316L, which has a higher melting point than CuCrZr, starts to solidify before surrounding CuCrZr. During solidification, the reduction in surface energy causes 316L to aggregate into spherical shapes. Region II (see Figure 1b) often exhibits cracking of the 316L, usually starting from Cu-rich phases and often reaching region III. These cracks are suspected to be induced by the thermal stress during the dissimilar solidification rates of the 316L and CuCrZr materials. The 316L cracks created during the PBF-LB/M process are filled with Cu-rich material, still in the liquid state. Region III consists mainly of 316L based regions, with occasional small cracking from region II. (Kuai et al., 2023)

3 AM and post-processing of 316L-CuCrZr

3.1 Classifications of material transitions and AM methods

AM allows the fabrication of different types of material transitions or interfaces between the discrete materials in multi-material components (Meyer et al., 2023). The types of material transitions in AM technology are shown in Figure 2.

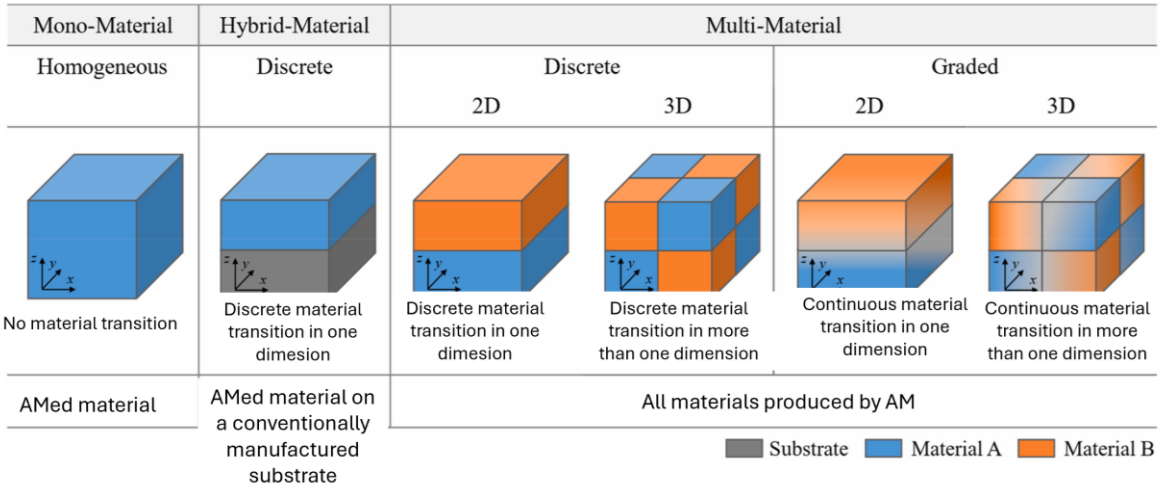

Figure 2. Classification of material transitions AM. Reproduced and modified from Meyer et al., 2023, which is under an open access Creative Common CC BY licence.

Figure 2 shows that the material transition types can vary based on the number and directions of the material transitions, as well as the amount of manufacturing methods utilised in the production. The types of material transitions can be categorised into mono-materials, hybrid-materials and multi-materials. AMed components consisting of one material are called mono-materials (Meyer et al., 2023). The manufacturing of hybrid-materials combines conventional non-AM methods, like casting and machining, with AM (Meyer et al., 2023). For instance, Kuai et al. (2023) manufactured a hybrid-material by AMing copper alloy onto a wrought stainless steel substrate, which was then machined into a preferred shape. Multi-materials are combinations of at least two discrete materials, which are both manufactured using AM. As Figure 2 illustrates, the multi-material transition zones can be oriented in either one or multiple directions and be either discrete or graded over volume (Hu et al., 2023; Meyer et al., 2023; Wang et al., 2022). Multi-materials where the transition of material happens gradually over volume are also called functionally graded materials (FGMs) (Hu et al., 2023).

Currently, three main strategies for PBF-LB/M of hybrid or multi-materials are recognised (Meyer et al., 2023). These strategies are shown in Figure 3.

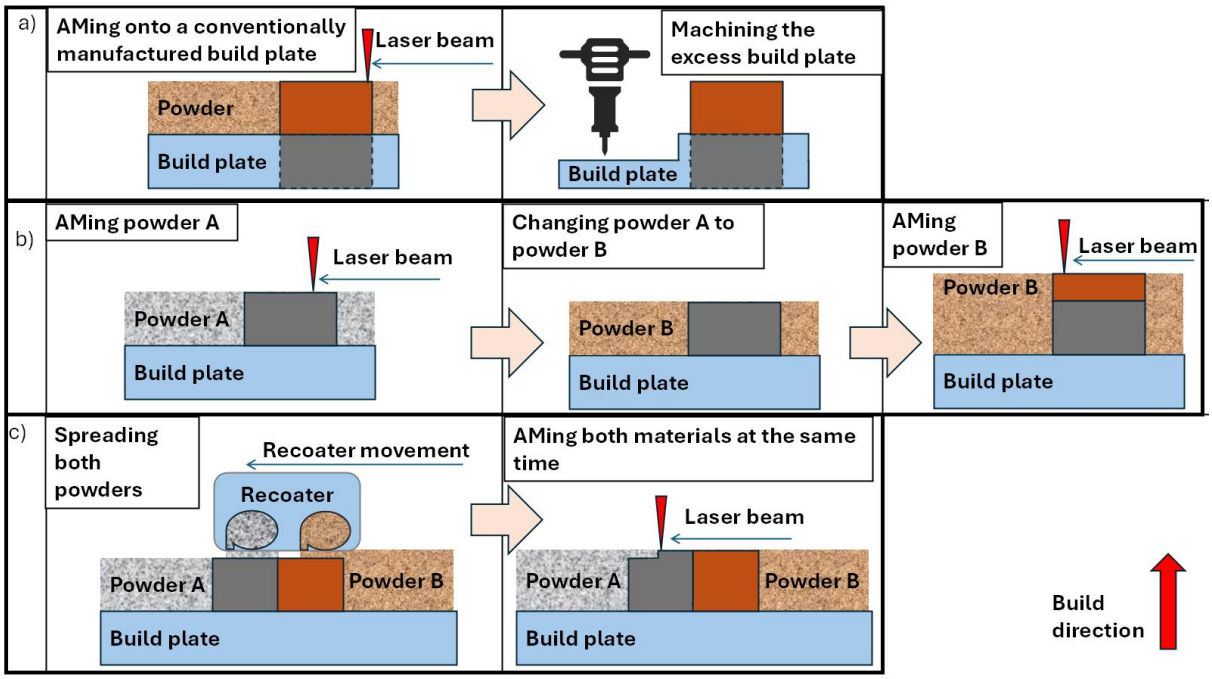

Figure 3. Hybrid or multi-material PBF-LB/M strategies: (a) hybrid-material manufacturing, (b) multi-material manufacturing, (c) multi-material manufacturing using a specialised recoater (inspired by the Aerosint powder deposition system).

As seen in Figure 3, the first strategy (see Figure 3a) composes a hybrid-material component using PBF-LB/M fabricating material B on a substrate or a build plate made of material A, which is then machined into the wanted design (Meyer et al., 2023). In the second method (see Figure 3b), a discrete material change happens in the build direction by first manufacturing material A, after which the powder feedstock is changed into material B, which is used to AM on top of the existing part (Meyer et al., 2023). The last strategy (Figure 3c) exploits a modified powder feeding and spreading system, which enables the precise placement of the discrete powders in one layer. This allows the AM of material transitions in multiple directions (see Figure 2) (Wang et al., 2022). At the time of composing this thesis, this type of multi-material powder feeding and spreading system was patented by the Aerosint company ("Schaeffler Aerosint - Multi-Material L-PBF," n.d.).

3.2 Selection of PBF-LB/M process parameters for 316L-CuCrZr

Optimising the PBF-LB/M process parameters, with the focus on the laser power and scanning speed, used for AM of CuCrZr material on top of a 316L substrate, has been the subject of

multiple articles (J. Chen et al., 2022; Deillon et al., 2024; Kuai et al., 2023; Liu et al., 2014; Mao et al., 2022; Martendal et al., 2024; Salvan et al., 2021; Wen et al., 2024). Due to the differences in material behaviour and AM machinery, optimisation of the PBF-LB/M process parameters is required to achieve a dense and defect-free product (Kuai et al., 2023). Gathering data and comparing the process parameters from previous studies increases the efficiency of the parameter optimisation process.

The process parameters can be compared by the individual values of laser power and scanning speeds. However, this fails to take into account the energy density produced by combining these parameters. For instance, an equivalent melting outcome could be achieved by combining higher laser power with quicker scanning speed or by combining lower laser power with slower scanning speed. Therefore, comparing process parameter combinations by computing their linear energy density (*LED*) is a more efficient way to evaluate suitable process parameter values for each application. *LED* is calculated as shown in Equation 1, by dividing the laser power, P (W), by scanning speed, v (mm/s).

$$LED = \frac{P}{v} \tag{1}$$

Besides comparing LED values, it is also necessary to account for the specific AM machine employed, the material transition type (see Figure 2), the material being processed, and the material serving as the substrate when conducting parameter comparisons.

Table 1 shows the *LED* values, materials and machines used in found publications about PBF-LB/M of CuCrZr on top of a 316L substrate or 316L-CuCrZr FGM.

Table 1. LED values, materials and AM machinery used in the articles.

Material order	**Material transition type**	**Machine**	***LED* [J/mm]**	**Reference**
CuCrZr on 316L	Discrete 2D	Aconity MIDI+	0.33-0.91	(Meyer et al., 2023)
CuCrZr on 316L	FGM	Suzhou XDM	0.54-1.00	(Mao et al., 2022)
CuCrZr inside 316L	Discrete 3D	Aconity MIDI+	0.91	(Deillon et al., 2024)
CuCrZr on 316L	Discrete 2D	Aconity MIDI+	0.88	(Martendal et al., 2024)

AMed CuCrZr on hot-rolled 316L substrate	Hybrid-material 2D	Beijing Eplus E-M150	0.46	(Kuai et al., 2023)

As seen from the

Table 1, the *LED* values of the PBF-LB/M process parameters used to manufacture CuCrZr on top of 316L, or the 316-CuCrZr FGM, vary from 0.33 to 1.00 J/mm. The high values of *LED* are necessary when manufacturing CuCrZr material, due to its high reflectivity and melting point (Meyer et al., 2025).

Deillon et al. (2024), Martendal et al. (2024) and Meyer et al. (2023) used Aconity MIDI+ in their studies. Martendal et al. (2024) fabricated samples by using a ring-shaped laser beam in PBF-LB/M. Deillon et al. (2024) used a couple hot pressing to increase the interface bonding quality in their samples. Meyer et al. (2023) provided rough design guidelines for PBF-LB/Med 316L-CuCrZr multi-material. According to the results by Meyer et al. (2023), the most homogenous melt pool joining zone could be achieved using the laser power of 400 W and scanning speed of 600 mm/s, amounting to an *LED* value of 0.667 J/mm.

Besides parameter optimisation, other laser scanning strategies, such as remelting, have also been proposed for increasing the interfacial bonding and decreasing the porosity or crack formation. Meyer et al. (2023) also conducted remelting or laser scanning of the CuCrZr layers multiple times without recoating to reduce cracking formation, porosity and relieve residual stress in the interface and simultaneously increase the density (Meyer et al., 2023). A remelting strategy can also remove oxide films from the processed and solidified surface and promote melting of material which has high reflectivity or melting point (Wang et al., 2022).

3.3 Post-processing of PBF-LB/Med 316L-CuCrZr

PBF-LB/M exposes the material to quickly changing heating and cooling cycles, which often cause non-optimal material properties, such as low tensile strength and microhardness (Laleh et al., 2023). The mechanical properties of the material are largely determined by the microstructure of the metal, which includes grain size, grain morphology, the character of grain boundaries, constituent phases, dislocation density and residual stresses, each affecting the properties of AMed metals (Laleh et al., 2023).

Heat treatment refers to a post-processing procedure done after the metal manufacturing process. It aims to improve the microstructure and other properties of the metal by exposing it to different heating and cooling cycles (Laleh et al., 2023). The most common effects of heat treatments include controlling the grain size, stress relief, changing the crystal structure, dissolving undesired secondary phases and encouraging precipitation of desired secondary phases (Laleh et al., 2023).

The mixture of columnar and equiaxed grains, typically produced by the rapid heating and cooling cycles in AM, promotes either anisotropic or isotropic material properties (Kuai et al., 2023). Larger grain size as well as high dislocation density decrease ductility while increasing the strength of the material (Kuai et al., 2023). The characteristics of grain boundaries affect the movement of the dislocations, increasing strength but, in some cases, promoting cracking and corrosion (Laleh et al., 2023). Heat treatments generally have increasing effects on the grain sizes, thus decreasing the amount of grain boundaries (Laleh et al., 2023).

Rapid thermal cycles in AM can initiate the formation of metastable phases or unintended phase transformation, which alters the hardness, corrosion resistance and toughness of the metal (Laleh et al., 2023). Depending on the application, material and the manufacturing process, some heat treatment is usually needed to reach the required material properties. (Laleh et al., 2023)

CuCrZr is traditionally heat-treated using solution annealing and age hardening techniques. Solution annealing is a heat treatment method which is usually carried out at high temperatures (980-1000 °C) followed by quenching, i.e. rapid cooling, to produce supersaturated metal (Meyer et al., 2025). Age hardening is usually done at lower temperatures (450-500 °C), which causes precipitation of Cu_xZr_y, Cr- and Zr-rich phases (Wallis & Buchmayr, 2019). These precipitates enhance the mechanical properties, corrosion resistance, thermal and electrical conductivity of the material (Meyer et al., 2025). Depending on the PBF-LB/M parameters, the microhardness tends to peak at a certain point during the ageing process, whereas the thermal and electrical conductivity improve continuously (Wallis & Buchmayr, 2019). Therefore, the optimal heat treatment of CuCrZr methods and techniques vary based on the intended application and property requirements (Meyer et al., 2025).

PBF-LB/Med CuCrZr tends to be supersaturated in its non-heat-treated as-built form (Meyer et al., 2025). The supersaturation may be caused by the rapid heating and cooling the material experiences during the PBF-LB/M process (Wallis & Buchmayr, 2019). Therefore, performing

only age hardening, which is also called direct age hardening (DAH), to PBF-LB/Med CuCrZr could reach similar properties as the standard solution annealing + age hardening combination (Meyer et al., 2025; Wallis & Buchmayr, 2019).

Wallis et al. (2019) tested material hardnesses and thermal conductivity properties from PBF-LB/Med CuCrZr, which were post-processed with different methods. The hardness and thermal conductivity values obtained with different heat treatment processes are listed in Table 2.

Table 2. Hardness and thermal conductivity of PBF-LB/Med CuCrZr before and after heat treatment by Wallis and Buchmayr et al. (2019).

Sample	**Hardness [HV1]**	**Thermal conductivity [W/mK]**
As-built	88 ± 2	100 ± 2
Solution annealing	77 ± 2	192± 4
Solution annealing + age hardening	126 ± 3	297 ± 6
DAH (450°C / 2h)	185 ± 2	239 ± 4

As seen from Table 2, performing only the solution annealing decreased the hardness by 10 HV1, while increasing the conductivity by 92 W/mK. Both solution annealing + age hardening and DAH increased both properties significantly. Solution annealing + age hardening increased the hardness by 38 HV1 and the thermal conductivity by 197 W/mK. The DAH increased the hardness by 97 HV1 (see Table 2) and the thermal conductivity by 139 W/mK. Therefore, performing DAH would be more beneficial for heat-treating CuCrZr. (Wallis & Buchmayr, 2019)

AMed 316L stainless steel does not benefit from heat treatment due to its austenite crystalline structure and the small grain structure that PBF methods can produce (Laleh et al., 2023). Conventionally manufactured 316L benefits from solution annealing, performed in a temperature range of 1010-1120 °C, which restores good corrosion resistance if it has been affected during the manufacturing process (Laleh et al., 2023). Laleh et al. (2023) found a general trend indicating that heat treatment decreases the hardness of 316L, especially when exposed to temperatures above 800 °C. Figure 4 illustrates how different hardness values are affected by different heat treatment temperatures (Laleh et al., 2023).

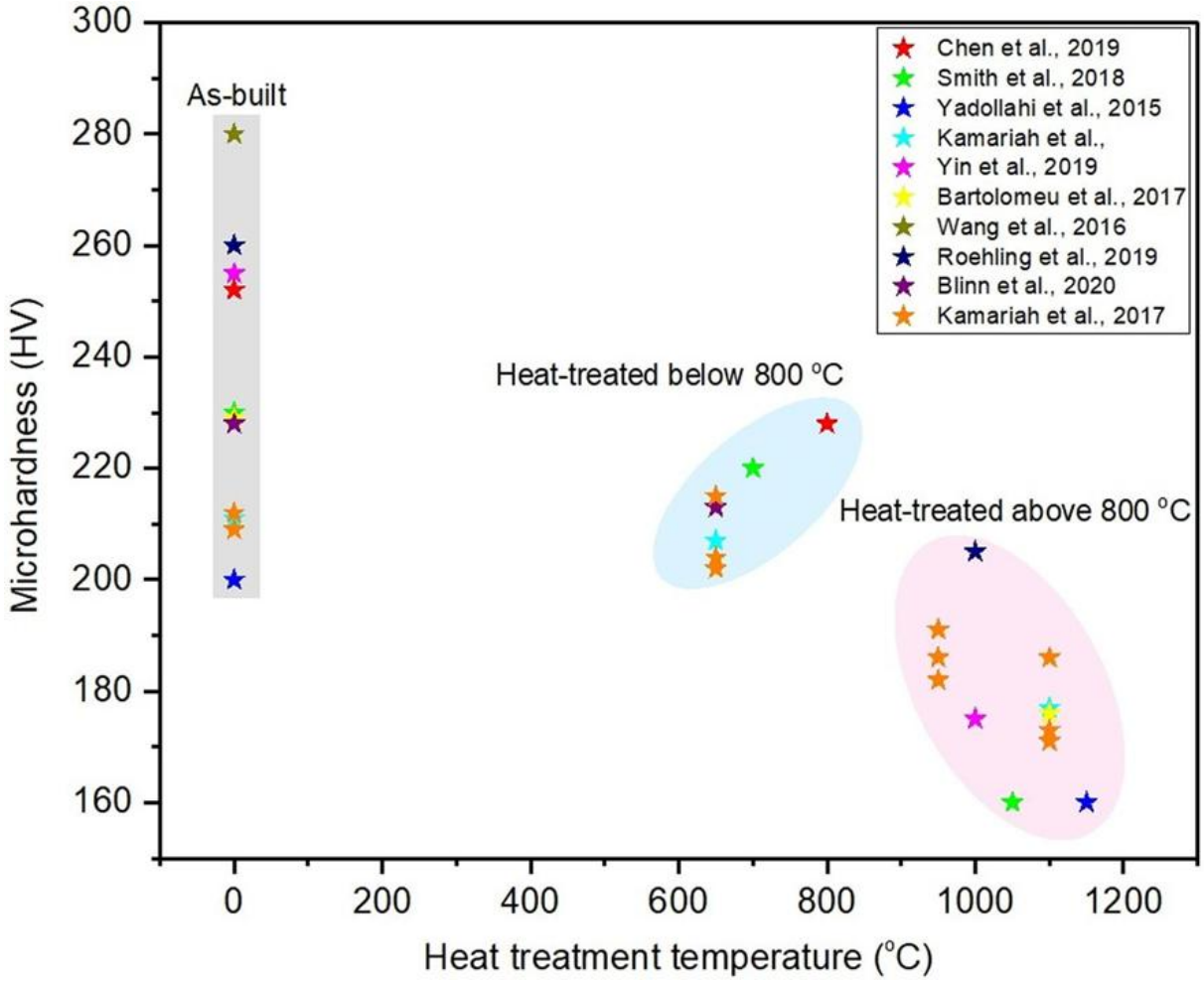

Figure 4. Vickers Hardness of austenitic stainless steels affected by different heat treatment strategies. Reproduced from Laleh et al., 2023, which is under an open access Creative Common CC BY licence.

Figure 4 shows the Vickers microhardness values of austenitic stainless steels (y-axis) in relation to the exposed heat treatment temperature (x-axis). Microhardness achieved in the as-built state in austenitic stainless steels varies between 300-200 HV. When heat-treated at temperatures between 600-800 °C, the microhardness values drop to between 240-200 HV. The austenitic steels heat-treated in temperatures above 800°C (800-1200 °C) have a microhardness between 210-150 HV (see Figure 4). This decrease in microhardness could be explained by the disappearance of dislocations, which are known for increasing the microhardness, after a heat treatment at high temperatures.

Therefore, when treating PBF-LB/Med 316L-CuCrZr multi-material, solution annealing and heating above 800 °C should be avoided to minimise the negative influence on the microhardness of 316L. However, the CuCrZr material in the multi-material system could benefit largely from low-temperature (400-500 °C) DAH (Laleh et al., 2023). In the study made

by Meyer et al. 316L-CuCrZr part manufactured by PBF-LB/M was treated using the DAH method at 500 °C for 1.5 h (Meyer et al., 2025). This procedure was done in an argon atmosphere to prevent scaling (Meyer et al., 2025).

4 Material testing of AMed 316L-CuCrZr

4.1 Metallographic analysis

Metallographic analysis, or analysis of the microstructure of metals, is one of the main ways to evaluate the quality of the studied material (*Metallographic Procedures and Analysis – A Review*, n.d.). Main aspects studied during metallographic analysis are different material phases as well as shapes and sizes of grains and defects, such as cracks and pores (J. Chen et al., 2022). The metallographic analysis research includes several stages: material preparation, imaging and analysis of the results (*Metallographic Procedures and Analysis – A Review*, n.d.). In the material preparation stage, the surface roughness of the samples is removed through grinding and polishing, allowing better visibility of microstructure and defects. The commonly used grinding and polishing standards and sequences vary with different materials, which can cause challenges when preparing multi-materials (Wei et al., 2020). To the knowledge of the author, no article was found that mentioned the exact grinding and polishing protocol for 316L-CuCrZr multi-material. The material preparation can also include etching, which highlights grain boundaries in the inspected material (Kuai et al., 2023). Etching protocol of the 316L-CuCrZr was mentioned in the articles by Kuai and Mao et al. (2022) to be conducted using $FeCl_3$ + HCl solutions for 3-10 s. However, this etching protocol affected only the CuCrZr material (Kuai et al., 2023; Mao et al., 2022).

Common metallographic analysis techniques applied in the articles included imaging methods such as optical microscopy, SEM and EDS (Liu et al., 2014). Optical microscopy is used to observe features, such as interface bonding, as well as defects such as cracking and porosity (Liu et al., 2014). Analysis of grains can also be conducted with optical microscopes from etched samples (Liu et al., 2014). These defects in multi-material samples can be caused by many aspects, including improper process parameters, such as laser power and scanning speed or heat treatment (see Chapter 2.3) (Riener et al., 2020).

4.2 Microhardness test

Hardness measurements have been a common material testing procedure mentioned in many publications studying multi-material AM of metals (Kuai et al., 2023; Liu et al., 2014; Mao et al., 2022; Meyer et al., 2025; Wen et al., 2024). In Vickers microhardness tests, the material is pressed using a small diamond pyramid indenter with a chosen load. The load ranges from a few grams to several kilograms, with 200 g being a common value with Fe-Cu multi-materials

(Meyer et al., 2025; Sundararajan & Roy, 2001). The resulting Vickers hardness (*HV*) value is calculated as shown by Equation 2 by dividing the applied load *F* (N) by the area *A* of the resulting hole (mm^2) (Sundararajan & Roy, 2001).

$$HV = \frac{F}{A} \tag{2}$$

Usually, with multi-material AM samples, the microhardness characterisation is conducted by testing the hardness linearly across the interface (Liu et al., 2014). This method allows the visualisation of the evolution of the material properties as the material itself changes (Liu et al., 2014).

A recurring observation of the publications measuring material hardnesses was that the microhardness was higher on the 316L material and decreased on the CuCrZr material side. This observation follows the previous knowledge on the differences in the microhardness properties of the 316L and CuCrZr. (Kuai et al., 2023; Liu et al., 2014; Mao et al., 2022; Meyer et al., 2025; Wen et al., 2024) An increasing effect on the microhardness of the CuCrZr side on the 316L-CuCrZr multi-material was also noticed after DAH, which causes the formation of hardness-increasing precipitation (see Chapter 3.3) (Laleh et al., 2023; Meyer et al., 2025).

Kuai et al. (2023) tested microhardness across the CuCrZr-316L interface using a 1.96 N load. The resulting HV0.2 values and images of the measurement indentations are depicted in Figure 5.

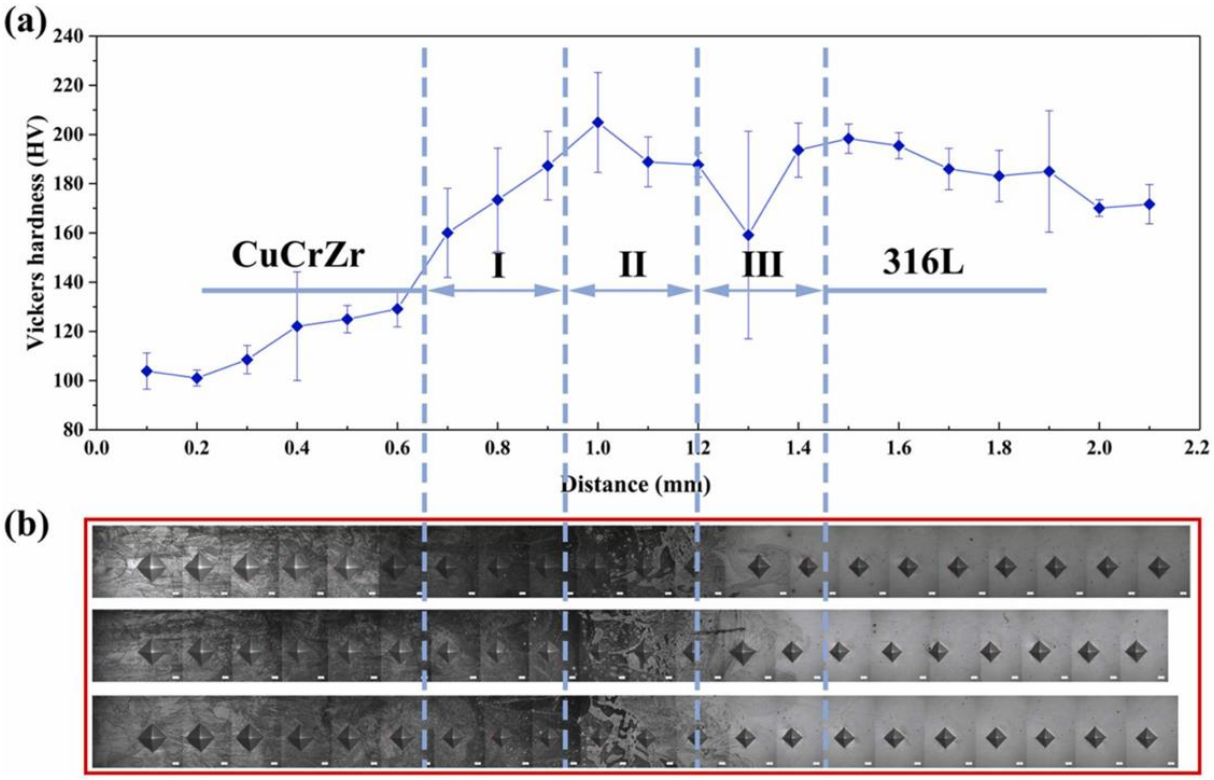

Figure 5 (a) Microhardness (HV0.2) values in relation to the locations of the measurement points (b) microscopic photos of the microhardness measurement points across the 316L-CuCrZr sample interface. Reproduced from Kuai et al., 2023, which is under an open access Creative Common CC BY licence.

As shown in Figure 5, the microhardnesses measured in the range of 200-270 HV0.2 with the PBF-LB/Med 316L (Kuai et al., 2023). The microhardnesses ranged between 80-130 HV0.2 with as-built PBF-LB/Med CuCrZr, which correlated to the CuCrZr microhardnesses measured in other studies (Kuai et al., 2023; Mao et al., 2022; Meyer et al., 2025). Meyer et al. (2025) observed that the microhardness of CuCrZr increased from 110 HV0.2 to 230 HV0.2 after DAH treatment, presumably caused by the precipitation formation.

As Figure 5 shows, the microhardness values are closer to the microhardnesses of 316L than CuCrZr in the 316L-CuCrZr multi-material interface. The 316L-CuCrZr interface microhardness values had a lot of variability, which could be caused by the separate Cu and Fe-rich phases, especially in region II. As the 316L-CuCrZr interface consists of separate Cu and Fe-rich phases (see Chapter 2.3), the hardness value taken from this region may depend on the location of the measurement point. (Liu et al., 2014).

4.3 Geometrical accuracy measurements

Geometrical accuracy tests aim to find a numerical evaluation method for comparing the precise geometry of the AMed component to the initial CAD model. The geometry of the AMed component will vary from the CAD model due to, for instance, warping caused by residual stresses in the part or unpredictable material melting behaviour. According to the literature review by Krasniqi et al. (2025), these geometrical differences can be affected by optimising laser power, scanning speed and the scanning pattern. In multi-material components, the most notable cause of geometrical inaccuracy is the misalignment between the materials, caused by part or build plate movement during the PBF-LB/M process. This misalignment is most visible at the interface and appears as offsetting of the materials (Krasniqi et al., 2025)

Geometrical accuracy can be measured using multiple methods. Macroscopic dimensional alterations can be measured using calipers or other high-resolution measuring tools such as commercial 3D scanners (Krasniqi et al., 2025). Microscopic alteration can be measured using CT systems (Krasniqi et al., 2025), such as tomoscopes or other high-precision 3D measuring devices able to generate a point cloud of the AMed component, which can then be compared computationally with the original CAD file (Merz et al., 2023).

4.4 Corrosion resistance test

Galvanic corrosion is a type of electrochemical corrosion of a metal when it is in electrical contact with another dissimilar metal and an electrolyte (Ye et al., 2024). Unintentional galvanic corrosion often occurs when two different metals are exposed to a liquid, which causes the less noble metal to dissolve into it (Ye et al., 2024). Galvanic corrosion is therefore a relevant phenomenon to take into account when using multi-materials in applications with water exposure, such as in marine hulls and heat exchangers, or any liquid pipelines (Ye et al., 2024).

Galvanic corrosion can be tested using numerous electrochemical analysis methods, and the set-ups may vary based on the objective and desired output of the test (Ye et al., 2024). The corrosion measurement set-up usually consists of a liquid medium, often a 3.5 wt.-% NaCl water solution, where the working electrode, i.e. the sample, the reference electrode, and the counter electrode are submerged (Fathi et al., 2021). The electrodes are connected to a potentiostat, which can be used to compute useful values and measurements, such as open corrosion potential (*OCP*) and Tafel extrapolation (Ye et al., 2024).

OCP is the steady state voltage, or the potential, that the tested material creates when no external current is applied and is a common way to evaluate the corrosion behaviour of a material (Fathi et al., 2021). A more positive *OCP* value indicates a more passive material, whereas a more negative *OCP* value means higher corrosion potential (Fathi et al., 2021).

Tafel plots are derived by electrochemical kinetics measurement or Tafel extrapolation, where the potential is scanned around the *OCP* value, while measuring the caused electrical current (Hemmasian Ettefagh & Guo, 2018). The resulting potential (*E)* is then plotted as a function of logarithmic current *log(I)* (Hemmasian Ettefagh & Guo, 2018). An example Tafel plot is shown in Figure 6.

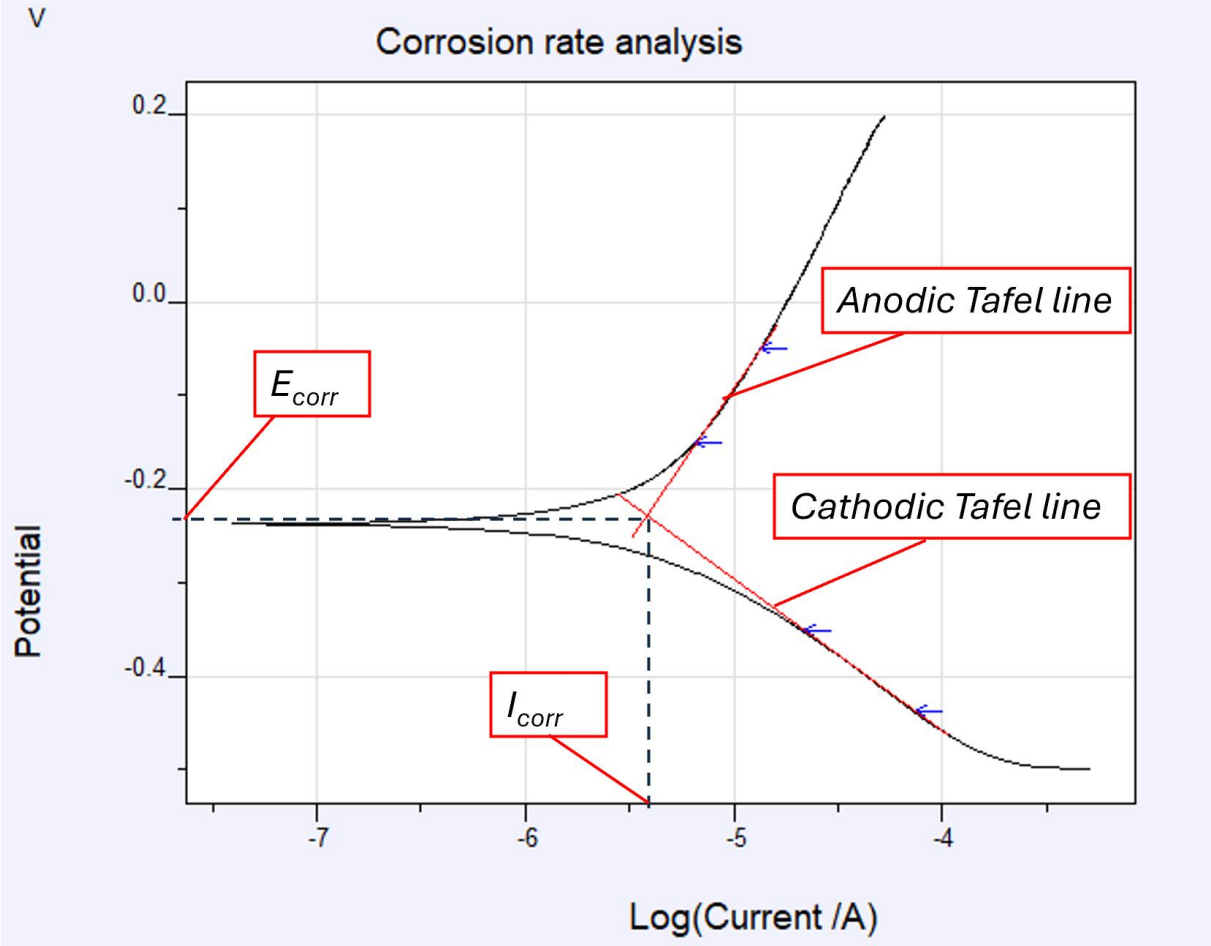

Figure 6. Example Tafel-plot schematic demonstrating the anodic and cathodic Tafel lines, natural corrosion potential and corrosion rate.

As Figure 6 shows, the Tafel graph can be used to derive anodic and cathodic Tafel lines, which can be used to derive theoretical values such as natural corrosion potential (E_{corr}), corrosion current density (I_{corr}) (Hemmasian Ettefagh & Guo, 2018). E_{corr} is derived from the intersection

of anodic and cathodic Tafel lines. Similar to *OCP,* E_{corr} describes the corrosion potential of the measured material. However, *OCP* is experimentally measured potential in no current conditions, whereas E_{corr} is the theoretical corrosion potential where rates of anodic and cathodic reactions are equal. Although they often have similar values, *OCP* and E_{corr} may differ if the measured system has not reached steady state or if surface reactions affect the potential. (Hemmasian Ettefagh & Guo, 2018). I_{corr} is derived similarly to the E_{corr} from the intersection of the cathodic and anodic Tafel lines (see Figure 6), and it can be used to compute the corrosion rate (mm/y) of the measured material.

Table 3 shows $E_{corr,}$ I_{corr} and *OCP* values of the PBF-LB/Med as-built 316L, heat-treated 316L and as-built CuCrZr, as reported in the literature.

Table 3. $E_{corr,}$ I_{corr} and *OCP* values of PBF-LB/Med 316L and CuCrZr reported in the literature

Material	***Ecorr* [V]**	***Icorr* [µA/cm^2]**	***OCP* [V]**	**Reference**
As-built 316L	-0.37	0.21	-0.13	(Bedmar et al., 2022)
As-built 316L	-0.36	1.29	-	(Hemmasian Ettefagh & Guo, 2018)
Heat-treated (400°C/4h) 316L	-0.37	1.33	-0.17	(Bedmar et al., 2022)
Heat-treated (650°C/2h) 316L	-0.35	0.67	-0.04	(Bedmar et al., 2022)
Heat-treated (800°C/2h) 316L	-0.35	1.14	-	(Hemmasian Ettefagh & Guo, 2018)
As-built CuCrZr	-0.43	23.0	-	(Dongfang et al., 2024)
As-built CuCrZr	-	-	-0.19	(Kwok et al., 2009)

Table 3 shows corrosion measurement data of PBF-LB/Med 316L and CuCrZr materials sourced from literature. The results of the effect of the heat treatment on the E_{corr}, I_{corr} and *OCP* vary. Hemmasian Ettefagh & Guo (2018) found that heat treating 316L at 800 °C for 2 h decreases its E_{corr} and I_{corr} values. This decrease was suspected to be caused by the elimination of residual stresses and the ability to produce a more stable protective layer. However, Bedmar et al. (2022) found that heat treatment at 400 °C for 4 h and 650 °C for 2 h had decreased or had no effect on the corrosion potential, i.e. the E_{corr} values, and increased the corrosion current, i.e. I_{corr} values of the 316L. These variations in E_{corr} values were hypothesised by Bedmar et al.

(2022) to be caused by differences in "oxygen limit current density" from measurements being conducted on the aerated water solutions in stagnant conditions. The changes in the I_{corr} value indicate that heat treatment causes a slight increase in corrosion resistance of 316L due to eliminating residual stresses, which can create a more stable passive oxidation film. (Hemmasian Ettefagh & Guo, 2018)

Bedmar et al (2022) measured the 316L *OCP* value in 3.5% NaCl solution to be -0.13 V in as-built 316L, -0.17 V when 316L was heat-treated at 400 °C for 4 h and -0.04 V when 316L was heat-treated at 650 °C for 2 h (Bedmar et al., 2022). The increase in the *OCP* values of 316L bulk materials after heat treatment at 650 °C for 2 h suggests the creation of new phases, especially MnS, which improves the formation of Cr Cr-based passive layer.

Dongfang et al. (2024) measured the electrochemical characteristics of PBF-LB/Med CuCrZr material. The study revealed that CuCrZr had an E_{corr} of -0.43 V and an I_{corr} of 23.3 μA/cm^2. As Table 3 shows, Kwok et al. (2009) measured the CuCrZr *OCP* value of -0.19 V (Kwok et al., 2009). To the knowledge of the author, no previous research exists on the effects on corrosion resistance of CuCrZr or stainless steel-CuCrZr multi-material by heat treatment.

4.5 Thermal conductivity test

CuCrZr, alongside other Cu-based materials, is often used in thermal management components, which is why the conductive properties are relevant to investigate when studying CuCrZr-316L multi-materials (Tang, Chen, Sun, Li, et al., 2022). Thermal or electrical conductivity, i.e. material-specific properties describing the flow of thermal energy or electrons in the metallic structure, can be disrupted by defects such as cracks and pores (Jadhav et al., 2021). In multi-material components, the interface of the discrete materials causes a scattering effect of the flowing electrons or thermal energy, due to sudden phase changes in the metallic structure, which also decreases the thermal conductivity of the material (Ibrahim et al., 2016).

Table 4 lists data on thermal conductivity measurement methods and results found in the literature.

Table 4. Thermal conductivity measurement methods and results of 316L and CuCrZr materials, reported in the literature

Material	Measurement method	Result [W/mK]	Reference
As-built CuCrZr	Eddy-current conductivity &	125	(Tang, Chen,

	Wiedemann-Franz law		Sun, Li, et al., 2022)
As-built CuCrZr	Eddy-current conductivity & Wiedemann-Franz law	100	(Xie et al., 2023)
Heat-treated (500°C/1h) CuCrZr	Eddy-current conductivity & Wiedemann-Franz law	255-307	(Xie et al., 2023)
Heat-treated (500°C/1h) CuCrZr	Eddy-current conductivity & Wiedemann-Franz law	266	(Tang, Chen, Sun, Li, et al., 2022)
Heat-treated (500°C/2h) CuCrZr	Eddy-current conductivity & Wiedemann-Franz law	325	(Tang, Chen, Sun, Li, et al., 2022)
Heat-treated (500°C/2h) CuCrZr	Laser Flash method	329	(X. Chen et al., 2024)
As-built 316L	Frequency domain thermoreflectance	10.4-19.8	(Simmons et al., 2020)

As seen from Table 4, thermal conductivity has been researched far more for CuCrZr than for 316L, due to the former material being common in thermal management applications (Tang, Chen, Sun, Li, et al., 2022). The thermal conductivity of the as-built CuCrZr measured 100-125 W/mK and increased to 255-329 W/mK after heat treatment. Thermal conductivity can be positively affected by the length of the heat treatment. Heat treatment at 500 °C for 1 h produces CuCrZr with thermal conductivity between 255-307 W/mK, whereas heat treatment at 500 °C for 2 h produces CuCrZr with thermal conductivity between 325-329 W/mK. The lower conductivity of the as-built CuCrZr is caused by a high dislocation density from the cooling-solidification frequency of the PBF-LB/M process. The increase in the conductivity after heat treatment is caused by the precipitation of Cr and Zr atoms from the Cu matrix. The increased heat treatment length allows more sufficient Cr and Zr precipitation, thus reducing the scattering effect created by the supersaturated Cu-based solid solution (Tang, Chen, Sun, Li, et al., 2022).

Table 4 also compares methods of measuring thermal conductivity. X. Chen et al. (2024) calculated the thermal conductivity of CuCrZr material by using a laser flash method. Simmons et al. (2020) tested the thermal conductivity of 316L material using an experimental frequency domain thermoreflectance method. Tang, Chen, Sun, Li, et al.(2022) and Xie et al.(2023)

determined the thermal conductivity of the material from the electrical conductivity of the material. The electrical conductivity was measured using an eddy-current conductivity meter. This value was then converted to a theoretical thermal conductivity using the Wiedemann-Franz law. In the Wiedemann-Franz law, the thermal conductivity λ (W/mK) is calculated as shown in Equation 3 by multiplying the constant Lorenz number L of 2.44×10^{-8} ($\Omega W K^{-2}$) with an absolute temperature T (K) and multiplying the result by the electrical conductivity σ (Ωm) or dividing it the electrical resistivity ρ (Ωm). (OLAFSSON et al., 1997)

$$\lambda = LT\sigma = \frac{L\,T}{\rho} \tag{3}$$

5 Aim and purpose of the experimental part

The experimental part of this thesis aims to gather information on the PBF-LB/M manufacturing and material properties of 316L-CuCrZr multi-material through empirical research. The experimental part of the thesis is conducted as shown in Figure 7.

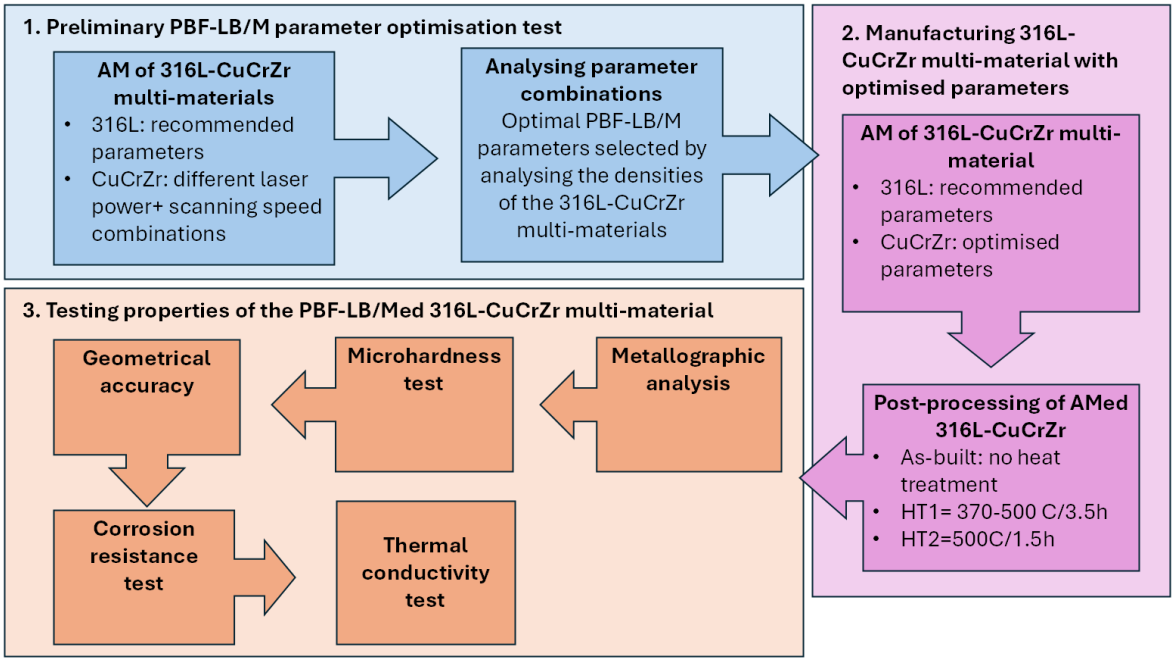

Figure 7. Flow chart of the procedure of the experimental part.

As shown in Figure 7, the experimental part of the thesis consists of three parts. In the first part, a preliminary PBF-LB/M parameter optimisation test is conducted. This stage aims to determine a laser power and scanning speed parameter combination for AMing CuCrZr on top of 316L PBF-LB/Med material. In the second stage of the experimental part, a 316L-CuCrZr multi-material is AMed using the optimised parameter combination. The 316L-CuCrZr multi-material is then post-processed in three separate ways shown in Section 2 in Figure 7. In the last stage, the 316L-CuCrZr materials are tested using a metallographic analysis, microhardness testing, geometrical accuracy measurements, corrosion resistance testing and thermal conductivity testing.

6 Experimental set-up

6.1 PBF-LB/M machinery

The experimental part of this thesis used an Aconity MIDI+ PBF-LB/M machine. The machine produces a laser beam with a maximum laser power value of 400 W. The samples were manufactured on a circular 316L build plate. The machine is shown in Figure 8.

Aconity MIDI+ machine and the components inside the machineAconity MIDI+ machine and the components inside the machine

Figure 8. Aconity MIDI+ machine and the components inside the machine.

Figure 8 shows the Aconity MIDI+ machine from the outside and the build plate, powder chamber and the recoater inside the machine.

6.2 Powders

The 316L powder was sourced from Nikon SLM solutions (*Nikon SLM Solutions Steel-Based Alloys*, n.d.). The chemical composition of the used powder is in Table 5.

Table 5. Chemical composition of the Nikon SLM Solutions 316L powder (*Nikon SLM Solutions Steel-Based Alloys*, n.d.)

Element	Fe	Cr	Ni	Mo	Mn	Si	P	C	S	N
wt.-%	Bal.	16.00-18.00	10.00-14.00	2.00-3.00	0.00-2.00	0.00-1.00	0.00-0.045	0.00-0.030	0.00-0.030	-

As shown in Table 5, 316L is an Fe-based steel with several alloying elements, the most notable of which are Cr, Ni and Mo with 16-18 wt.-%, 10-14 wt.-% and 2-4 wt.-%, respectively. Other elements include Mn, Si, P, C, S and N. The SEM image of the powder particles of the 316L powder is shown in Figure 9.

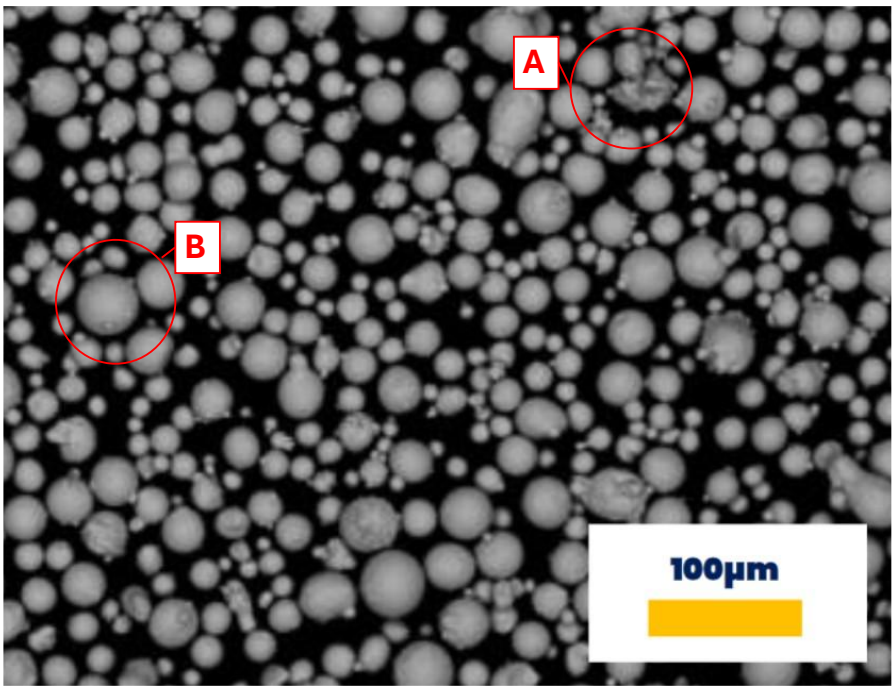

Figure 9. SEM image of the Nikon SLM Solutions 316L powder. Reproduced and modified from (*Nikon SLM Solutions Steel-Based Alloys*, n.d.) material data sheet.

As shown in Figure 9, the 316L powder consists of mostly spherical particles. However, the SEM image shows a few particles which differ from this standard. The particle marked as A is irregular in its shape, not conforming to the rounder morphology of the rest of the particles (Chu et al., 2021). The particle cluster marked as B exhibits a satellite particle, which is are smaller particle fused on the surface of a larger particle (Chu et al., 2021). The particle sizes of the 316L powder fall in the range of 10-45 µm, and the mass density of the powder is in the range of 7.9 g/cm³ (*Nikon SLM Solutions Steel-Based Alloys*, n.d.).

The CuCrZr material was sourced from EOS. The precise chemical composition of the CuCrZr powder used in this project is shown in Table 6.

Table 6. Chemical composition of the EOS CuCrZr powder (*MDS EOS CopperAlloy CuCrZr*, n.d.)

Element	Cu	Cr	Zr	Fe	Si

wt.-%	Bal.	0.45-1.15	0.05-0.25	0.00-0.08	0.00-0.01

As seen from Table 6, the primary alloying constituents of CuCrZr are Cr and Zr, with 0.45-1.15 wt.-% and 0.05-0.25 wt.-% compositions, respectively. Additionally, CuCrZr has small amounts of Fe and Si. The SEM image of the EOS CuCrZr powder particles is provided in Figure 10.

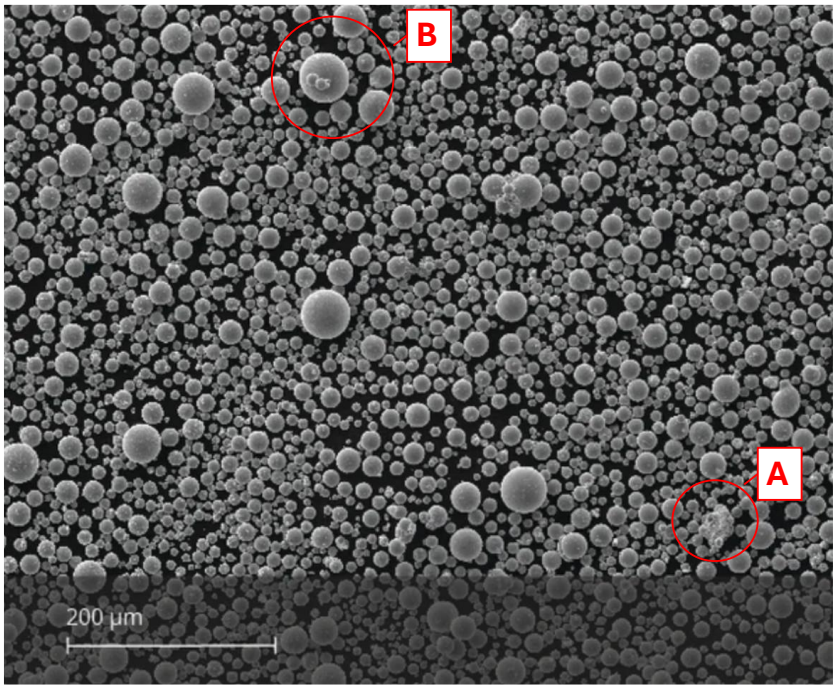

Figure 10. SEM image of the EOS CuCrZr powder. Reproduced and modified from (*MDS EOS CopperAlloy CuCrZr*, n.d.) material data sheet.

As shown in Figure 10, the CuCrZr powder consists of mostly spherical particles, with a few exceptions to this standard morphology. In Figure 10, the particle marked as A is irregular in its shape (Chu et al., 2021). The particle marked as B shows a satellite particle system with a few smaller particles fused onto the surface of the larger particle (Chu et al., 2021). The particle size distribution of the CuCrZr powder is in the range of 15-45 µm (*MDS EOS CopperAlloy CuCrZr*, n.d.).

6.3 CAD and slicing software

The CAD models of the multi-material components were done using Creo CAD software. Autodesk Netabb software was then used for slicing the CAD model into horizontal layers and for toolpath generation of the laser scanning movement.

6.4 Equipment and materials used in post-processing and pre-test preparation of 316L-CuCrZr

Figure 11 shows machinery and equipment used in post-processing and preparing the PBF-LB/Med 316L-CuCrZr for material tests.

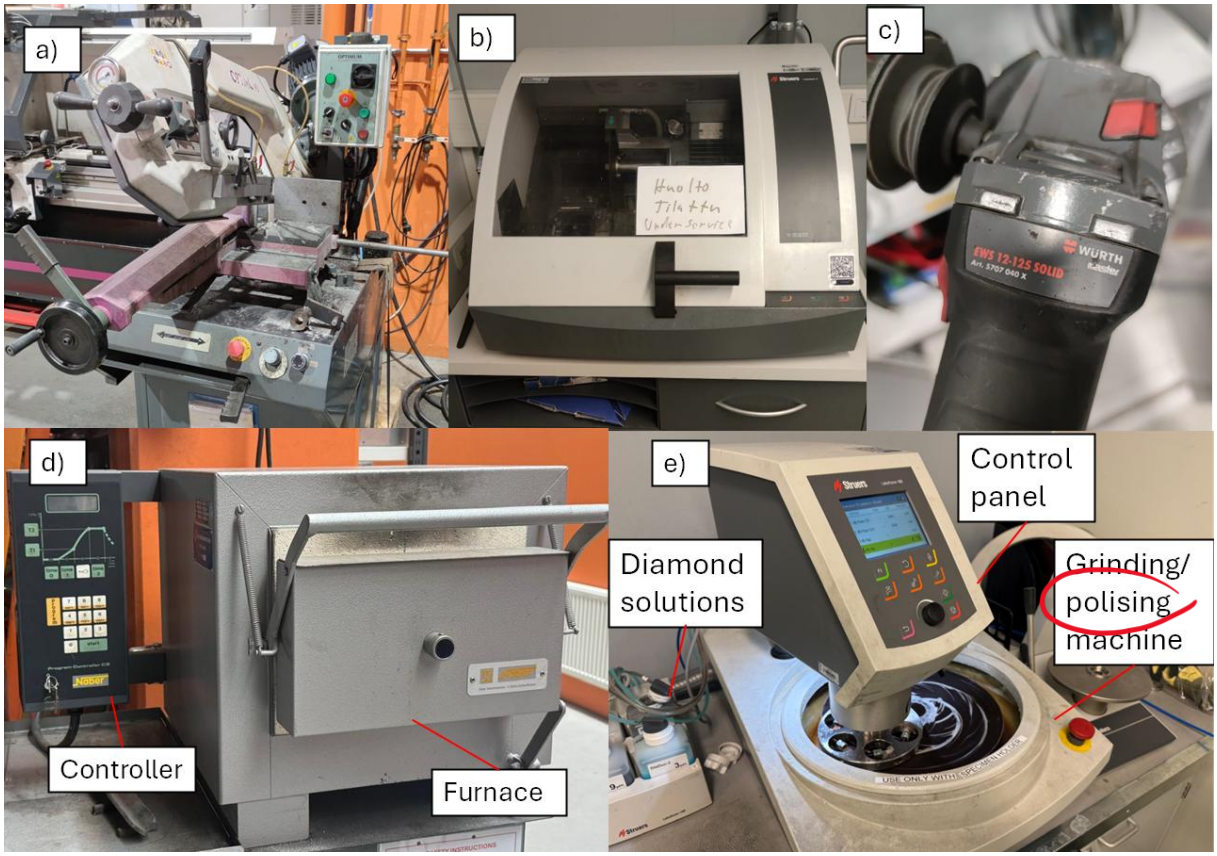

Figure 11. Images of machinery used to cut, heat treat, grind and polish 316L-CuCrZr material: a) metal bandsaw, b) cut-off machine, c) angle grinder, d) heat treatment machinery, e) grinding and polishing equipment.

Figure 11 shows the machinery used to cut the 316L-CuCrZr multi-material. An Optimum OPTI S 290 G, metal bandsaw (see Figure 11a) was used to cut the PBF-LB/Med 316L-CuCrZr off the base plate after the PBF-LB/M. For thermal conductivity tests, the 316L-CuCrZr was further cut using a Stuerts Labotom-5 cutting machine (see Figure 11b) and a Wurth EWS 12-125 solid angle grinder (see Figure 11c). Heat treatment of the 316L-CuCrZr was conducted

using the Nabertherm N7 furnace, which was operated with the Nabertherm program controller C5 (see Figure 11d).

316L-CuCrZr multi-materials used in metallographic analysis, microhardness and corrosion tests were embedded in epoxy resin, which was mixed using Stuers VersoCit-2 powder and liquid. The 316L-CuCrZr was ground and polished using the Struers LaboSystem machine, consisting of a Struers LaboPol-30 grinding and polishing machine equipped with LaboForce-100 control panel and specimen mover unit (see Figure 11e). Table 7. Surfaces and solutions used in the grinding and polishing of 316L-CuCrZr. Table 7 shows the combinations of surfaces and liquid solutions used in the grinding and polishing of 316L-CuCrZr.

Table 7. Surfaces and solutions used in the grinding and polishing of 316L-CuCrZr.

Grinding and polishing surfaces, Grit	**Solution**
Struers MD Piano, 220#	Tap water
Struers MD Piano, 600#	Tap water
Struers MD Piano, 1200#	Tap water
Struers MD Nap	Struers, DiaDuo-2 9µm
Struers MD Nap	Struers, DiaDuo-2 3µm
Struers MD Nap	Struers, DiaDuo-2 1µm

As shown in Table 7, the 316L-CuCrZr material was ground using Struers MD Piano grinding surfaces with grit sizes of 220#, 600# and 1200#. In the grinding process, tap water was used for cooling and lubrication. In polishing 316L-CuCrZr, Struers MD-Nap polishing cloth disks were combined with Struers DiaDuo-2 diamond solutions with particle sizes of 9µm, 3µm and 1µm. A Kramfors Tools ultrasonic cleaner was used to clean the 316L-CuCrZr parts during the grinding and polishing process.

316L-CuCrZr multi-materials used in metallographic analysis were etched using a self-mixed etching solution. The etching solution consisted of 98 *ml* of purified water, 2 *ml* of HCl and 3 *g* of $FeCl_3$. The liquid HCl concentration was 30 % sourced from VWR chemicals. The powder $FeCl_3$ was supplied by Thermo Scientific.

6.5 Equipment used in the analysis of material properties of PBF-LB/Med parts

In the preliminary PBF-LB/M process parameter optimisation test and metallographic analysis, a Motic AE200MET optical microscope was used for imaging the 316L-CuCrZr multi-material. The microscope images were captured using RisingView Software from a laptop connected to the microscope. An image of the metallographic analysis set-up can be seen in Figure 15.

The microhardness tests were conducted using an Innovatest Falcon 600 measurement machine. The microhardness testing machine was operated using Innovatest IMPRESSIONS software. An image of the microhardness test set-up can be seen in Figure 16.

Geometrical accuracy tests were conducted using an Alicona Bruker InfiniteFocus G6 optical 3D machine (see Figure 17) and Alicona LaboratoryMeasurementModule software. Corrosion resistance measurements were done using a beaker with 3.5 wt.-% NaCl solution, an Ag/AgCl reference electrode and a graphite rod. The electrodes were connected to an Ivium VERTEX potentiostat/galvanostat. The schematic illustration of the corrosion resistance test set-ups can be seen in Figure 19. The results were analysed using IviumSoft software.

Thermal conductivity measurements were done using a HIOKI RM 3545 four-terminal resistance meter (see Figure 20).

7 Experimental Procedure

7.1 Preliminary PBF-LB/M parameter optimisation test

7.1.1 Layout and dimensions of 316L-CuCrZr parameter optimisation parts

In the preliminary PBF-LB/M process parameter optimisation test, twelve 316L-CuCrZr parts were PBF-LB/Med with varying laser power and scanning speed parameter combinations for CuCrZr material. Dimensions and the PBF-LB/M layout of the 316L-CuCrZr parts are shown in Figure 12.

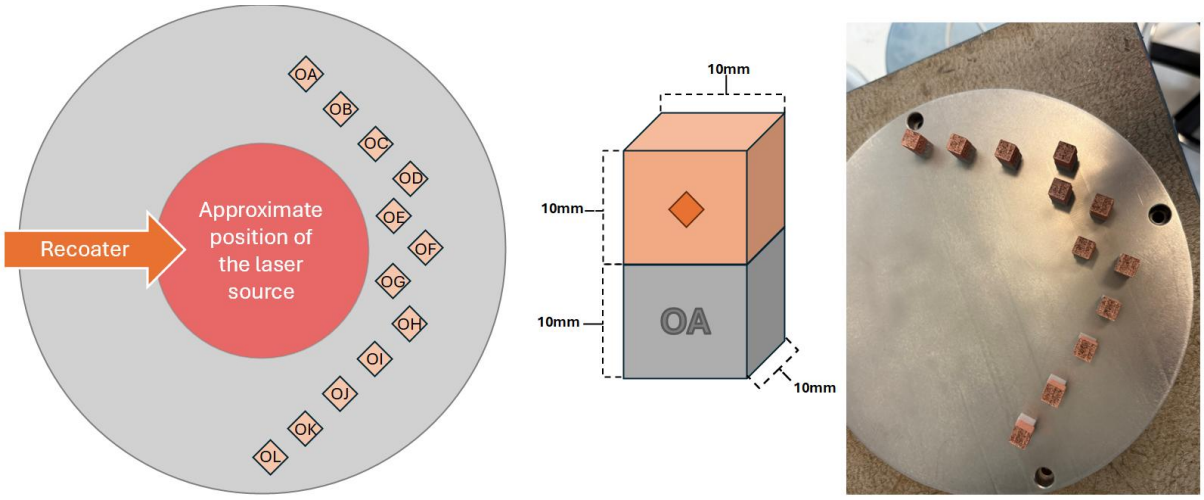

Figure 12. Layout and dimensions of the 316L–CuCrZr parts used in the preliminary PBF-LB/M parameter optimisation test.

As Figure 12 shows, the 316L-CuCrZr parts were manufactured in a half-circular shape, around the position of the laser source to prevent the backscattering of the laser from reflective CuCrZr powder. The 316L–CuCrZr parts were oriented at a 45° angle relative to the recoater to minimise the area of impact between the samples and the recoater during powder spreading. This orientation helps to prevent uneven powder distribution across the surface of the part and reduces the risk of material accumulation on one side of the surface (Reijonen et al., 2024). Figure 12 also shows the build dimensions of the 316L-CuCrZr parts, which were composed of two stacked 10 mm x 10 mm x 10 mm cubes. Each of the parts was embedded with different lettering on the surface, ranging from OA to OL alphabetically, to help distinguish them from each other. The extrusion height of the lettering and the diamond shape from the surface of the part was 0.3 mm.

7.1.2 Manufacturing of 316L-CuCrZr parameter optimisation parts

The parameter optimisation 316L-CuCrZr parts were fabricated as shown in Figure 13.

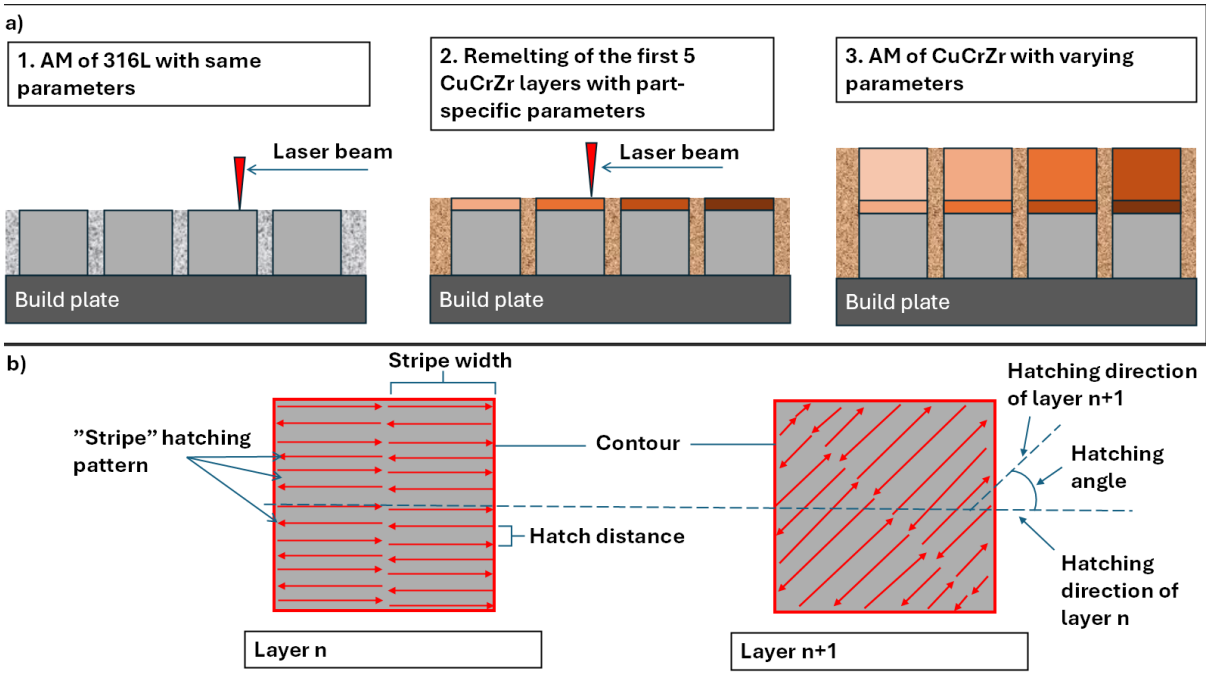

Figure 13. a) Schematic illustration of the multi-material PBF-LB/M process methodology and b) defining layer toolpathing terminology used in the AMing of the preliminary parameter optimisation test and the material testing 316L-CuCrZr parts.

As shown in Figure 13a, the 316L material was PBF-LB/Med first on the build plate using the same PBF-LB/M process parameters. The CuCrZr material was then manufactured on top of the 316L with varying process parameters used in each part. The first five CuCrZr layers from the interface were remelted using the part-specific parameters (see Table 8). Figure 13b illustrates important toolpath parameters, which determine the scanning methodology of individual layers. Each layer consists of a contour outlining and a hatching area inside the contour. The hatching pattern was selected to be "stripe", which consists of straight scanning tracks, seen as red points in Figure 13b. The parameter hatching angle, which was set to 67 degrees for both materials, defines the angle at which the stripe pattern is rotated between layers. The stripe widths or the maximum lengths of the individual laser scan tracks were set to 5 mm with 316L and 6mm with CuCrZr. The hatch distances, meaning the distances between the centre points of the scan tracks, were set to 0.08mm with 316L and 0.12 mm with CuCrZr. The layer thicknesses of both materials were set to 0.03 mm.

The varying parameters and their corresponding *LED* values (see Equation 3) used to manufacture the 316L-CuCrZr parts for preliminary parameter optimisation are listed in Table 8.

Table 8. PBF-LB/M process parameters used in manufacturing the 316L-CuCrZr parts for the preliminary parameter optimisation test.

Processed material	***P* [W]**	***v* [mm/s]**	***LED* [J/mm]**
316L hatching	150	900	0.17
316L contour	130	600	-
CuCrZr hatching OA	370	590	0.63
CuCrZr hatching OB	370	620	0.60
CuCrZr hatching OC	370	650	0.57
CuCrZr hatching OD	370	680	0.54
CuCrZr hatching OE	380	615	0.62
CuCrZr hatching OF	380	645	0.59
CuCrZr hatching OG	380	675	0.56
CuCrZr hatching OH	380	705	0.54
CuCrZr hatching OI	390	625	0.62
CuCrZr hatching OJ	390	655	0.60
CuCrZr hatching OK	390	685	0.57
CuCrZr hatching OL	390	715	0.55
CuCrZr contour	300	1200	-

Table 8 shows *P, v* and *LED* parameter combinations used for manufacturing the 316L and CuCrZr for each PBF-LB/Med part. It also lists the material-specific parameter combination for the contours, which are the outlines of the melted layers (see Figure 13b). The parameters for 316L, as well as the contours of both materials, were chosen based on the recommendations from the supplier of the used PBF-LB/M machine. The CuCrZr OA-OL parameter combinations were based on findings by Meyer et al. (2023), who observed that the *P* of 400W and *v* of 600 mm/s, with resulting *LED* of 0.67 J/mm, was able to produce the densest 316L-CuCrZr interface with the Aconity MIDI+ AM machine. However, the Aconity MIDI+ machines used by Meyer et al. (2023) and in this thesis have different maximum *P* values of 500 W and 400 W, respectively. Using the maximum *P* value during the PBF-LB/M was not

used to reduce the risk of harming the AM machine. Therefore, the *P* values in the range of 370-390 W were used in the optimisation process. The *v* values were therefore chosen to produce *LED* values similar to the 0.67 J/mm found by Meyer et al. (2023).

7.1.3 Sample preparation and parameter optimisation analysis

The 316L-CuCrZr parts were removed from the base plate using a belt saw, after which they were washed with tap water. The belt was a little misaligned from the base plate, which caused some of the samples to lose more material than others. However, this difference did not affect the parameter optimisation as the parts were studied mainly from the interface of the 316L and CuCrZr, which was not affected by the saw.

The grinding process used grinding disks and water, progressing from 220# (for 4 min), 600# (for 6 min), to 1200# (for 6 min) grit. The polishing was done using a cloth, polishing disks with 9 µm (for 5 min), 3 µm (for 5 min) and 1 µm (for 5 min) particle-sized diamond solutions. The polished 316L-CuCrZr parts were cleaned in a water-filled ultrasonic cleaner at 30 C° for 3 min. The polished surfaces were inspected and photographed with an optical microscope set-up (see Figure 15). The microscopic imaging concentrated on the interface of CuCrZr and 316L, and was conducted with 2.5x magnification.

A homebrew defect analysis Python program developed by the author and used to analyse the microscope images. The program recognised the defects based on the darkness of the pixels and compared them to a manually set threshold value. The percentages of the pixels under the threshold value were recognised as defects. This data is then used to calculate the defect percentage (*defect-%*) of the analysed images and to produce images with highlighted areas where defects were. A more precise explanation of the defect analysis program can be found in Appendix 1 Homebrew defect analysis program. The *defect-%* values were used to evaluate the density and the quality of the 316L-CuCrZr multi-material produced by each parameter combination. The parameter combination which produced the densest multi-material was chosen for manufacturing the 316L-CuCrZr used in the material testing.

7.2 Manufacturing the 316L-CuCrZr parts for testing material properties

7.2.1 Layout, dimensions and manufacturing of the material test parts

Twelve 316L-CuCrZr multi-material parts were PBF-LB/Med for the material testing. Figure 14 shows the multi-material part dimensions and the layout of the parts on the build plate during the PBF-LB/M.

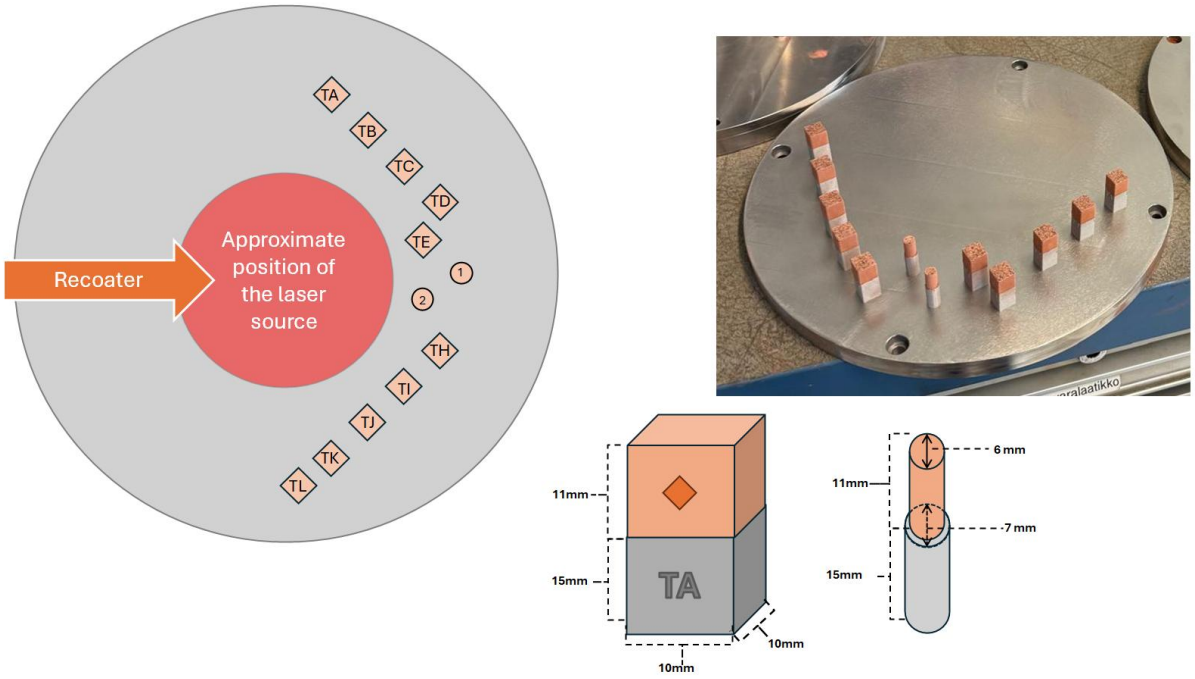

Figure 14. Layout and dimensions of the 316L-CuCrZr parts AMed for the material testing.

Figure 14 shows that the placements and orientations of the 316L-CuCrZr multi-material parts were the same as in the parameter optimisation parts. Overall, ten cuboid and two cylindrical multi-material parts were manufactured for material testing. The cuboid parts had dimensions of 15 mm x 10 mm x 10 mm of the 316L side and of 11 mm x 10 mm x 10 mm of the CuCrZr side. The cylindrical parts had a diameter of 6 mm and a height of 11 mm on the CuCrZr side, and a diameter of 7 mm and a height of 15 mm on the 316L side. Each of the parts was embedded with different lettering on the surface, namely TA-TE and from TH-TL alphabetically, apart from the cylindrical dilatometry samples. The placements of the AMed parts and the lettering are shown in Figure 14. The extrusion height of the lettering and the diamond shape on the surfaces of the parts was 0.3 mm.

The toolpathing parameters (see Figure 13b), including layer thickness, hatching angle and hatching pattern, were set to 0.03 mm, 67 ° and “stripe”, respectively, for both materials. For 316L, the hatch distance and stripe width were set to 0.08 mm and 5 mm. For CuCrZr, the hatch distance and stripe width were set to 0.12 mm and 6 mm. The *P*, *v* and their corresponding *LED* values used to AM the 316L-CuCrZr parts for material testing are shown in Table 9.

Table 9. Parameter combinations used to manufacture the 316L-CuCrZr multi-material parts for material tests.

Processed material	***P* [W]**	***v* [mm/s]**	***LED* [J/mm]**
316L hatching	150	900	0.17
316L contour	130	600	-
CuCrZr hatching	370	590	0.63
CuCrZr contour	300	1200	-

Table 9 shows PBF-LB/M process parameter combinations used to produce the 316L-CuCrZr parts for material testing. The 316L material was AMed using a *P* of 150 W and a *v* of 900 mm/s. CuCrZr material was AMed using *P* of 370 W and *v* of 590 mm/s, which were determined to be able to produce the densest 316L-CuCrZr interface out of the other tested parameter combinations (see Chapter 7.1.2). The contours of 316L and CuCrZr were manufactured using the process parameters recommended by the supplier of the AM machine.

7.2.2 The post-processing of the material test parts

After the PBF-LB/M, the 316L-CuCrZr material test parts were removed from the build plate using the metal bandsaw, similarly to the parameter optimisation parts. DAH heat treatment, similar to the one conducted in the study by Meyer et al. (2025), was then conducted on some of the 316L-CuCrZr specimens. The procedure was conducted by heating the 316L-CuCrZr parts to 500 °C and holding at this temperature for 1.5 h, followed by air cooling. However, during the heat treatment process, approximately 14 minutes after the temperature reached 500 °C, the heating was accidentally paused for 76 minutes. When this error was noticed, the furnace temperature had decreased to 370 °C, after which the DAH process was started and run again immediately and kept at 500 °C for 1.5 h, followed by air-cooling. Overall, this 1st heat treatment lasted approximately 3,5 h.

A 2nd post-processing round was then conducted with new as-built 316L-CuCrZr parts, which were successfully heat-treated at 500 °C for 1.5 h. The material heat-treated in the 1st heat treatment round was used in the material tests, as it was found that similar 316L-CuCrZr material has been processed for longer times in the temperature range of 370-500 °C (Wallis & Buchmayr, 2019). Therefore, the heat-treatment at 500-370 °C for 3.5 h is referred to as HT1, and the heat-treatment at 500°C for 1.5 h is referred to as HT2 in this thesis.

7.3 Testing material properties

7.3.1 Metallographic analysis

The metallographic analysis was executed with the as-built and the HT1 and HT2 316L-CuCrZr parts. The 316L-CuCrZr parts were embedded in cold epoxy, after which they were ground and polished, following the same procedure as in the parameter optimisation (see Chapter 7.1.3) until a mirror-finish surface. The set-up used for the metallographic imaging is depicted in Figure 15.

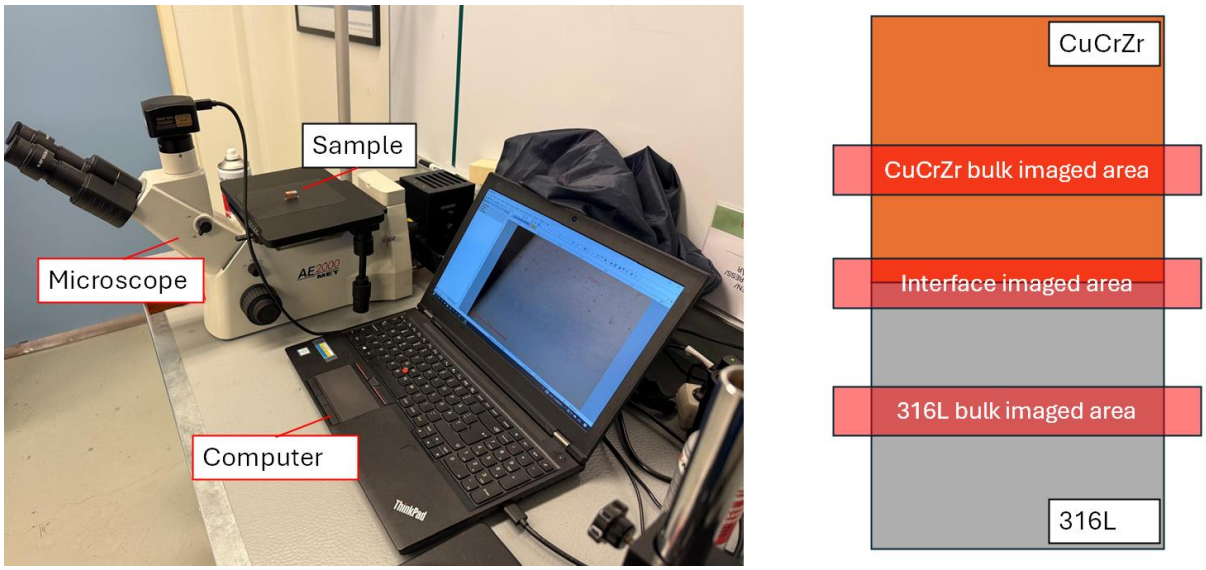

Figure 15. Set-up of the metallographic tests and schematic illustration of the imaged areas.

As Figure 15 shows, the optical microscope was connected to a computer, which was used to capture and export images. The 316L-CuCrZr parts were imaged from the interface and the bulk sections of the CuCrZr and 316L material (see Figure 15) with different magnifications. The bulk materials were imaged using 2.5x magnification, and the interface was imaged using 5x magnification. The samples were then etched in FeCl3 + HCl solution for 3 seconds, which

stained the CuCrZr material. The etched samples were then microscopically examined at the material interface with 5x and 10x magnification. The results were exported and analysed using the same defect analysis program as during the parameter optimisation (see Appendix 1 Homebrew defect analysis program).

During the analysis of the images of the as-built, HT1 and HT2 bulk 316L, bulk CuCrZr and 316L-CuCrZr interface, it was noticed that they had variances in saturation and lighting conditions. Additionally, 316L bulk, CuCrZr bulk, and the interface of 316L and CuCrZr exhibited different types of defects (such as cracking or porosity), which affected the precision of the defect analysis program. Therefore, all the microscopic images were run through the image analysis program in nine groups: as-built 316L bulk, as-built CuCrZr bulk, as-built 316L-CuCrZr interface, HT1 316L bulk, HT1 CuCrZr bulk, HT2 316L-CuCrZr interface, HT2 316L bulk, HT2 CuCrZr bulk and HT2 316L-CuCrZr interface images. The pixel darkness threshold in each analysed image group was adjusted to a value which would compute *defect-%* as accurately as possible. A more precise explanation of the threshold adjustment process and image analysis is provided in Appendix 1 Homebrew defect analysis program.

7.3.2 Microhardness test

The microhardness testing was conducted with ground and polished as-built, HT1 and HT2 316L-CuCrZr parts. A Vickers microhardness HV0.2 test, using a 1.96 N load with a dwell time of 10 seconds, was chosen as the hardness testing method for this thesis. Each 316L-CuCrZr part was set to the hardness measurement machine and measured from 10 measurement points across the interface, as shown in Figure 16.

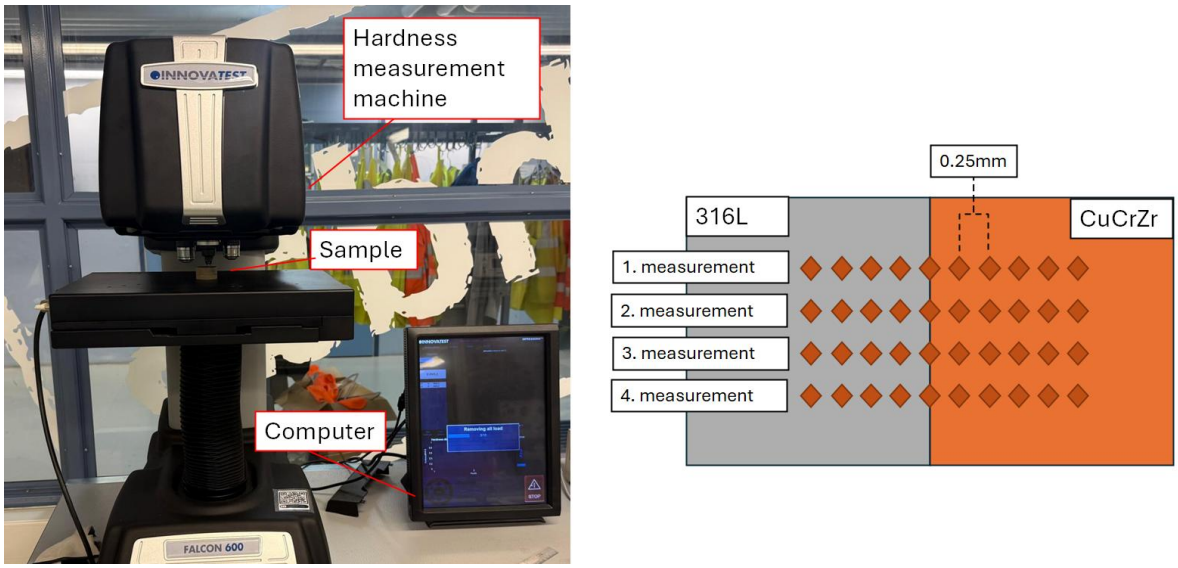

Figure 16. Microhardness measurement set-up and a schematic illustration of the Vickers hardness test plan on the 316L-CuCrZr part. The relative sizes and dimensions of the visualised multi-material parts geometry and the measurement points are oversaturated.

Figure 16 shows the set-up of the hardness measurement equipment as well as the schematic illustration of the hardness measurement point layout across the 316L-CuCrZr interface. The distance between the measurement points was 0.25 mm, with the 5th point being directly in region II of the interface (see Chapter 2.3). The sizes and the hardness values of each of the dents were then measured and calculated manually from the computer (see Figure 16). Overall, four hardness measurement lines were performed on each of the tested materials (as-built, HT1 and HT2). After each measurement, the results were exported and analysed using Microsoft Excel.

7.3.3 Geometrical accuracy measurement

Geometrical accuracy was measured from the as-built and HT1 316L-CuCrZr parts. At the time of the geometrical accuracy measurements, the used multi-material parts had not gone through any drastic shape-altering operation apart from separation from the build plate. The measurements were conducted using an Alicona optical coordinate measuring system depicted in Figure 17.

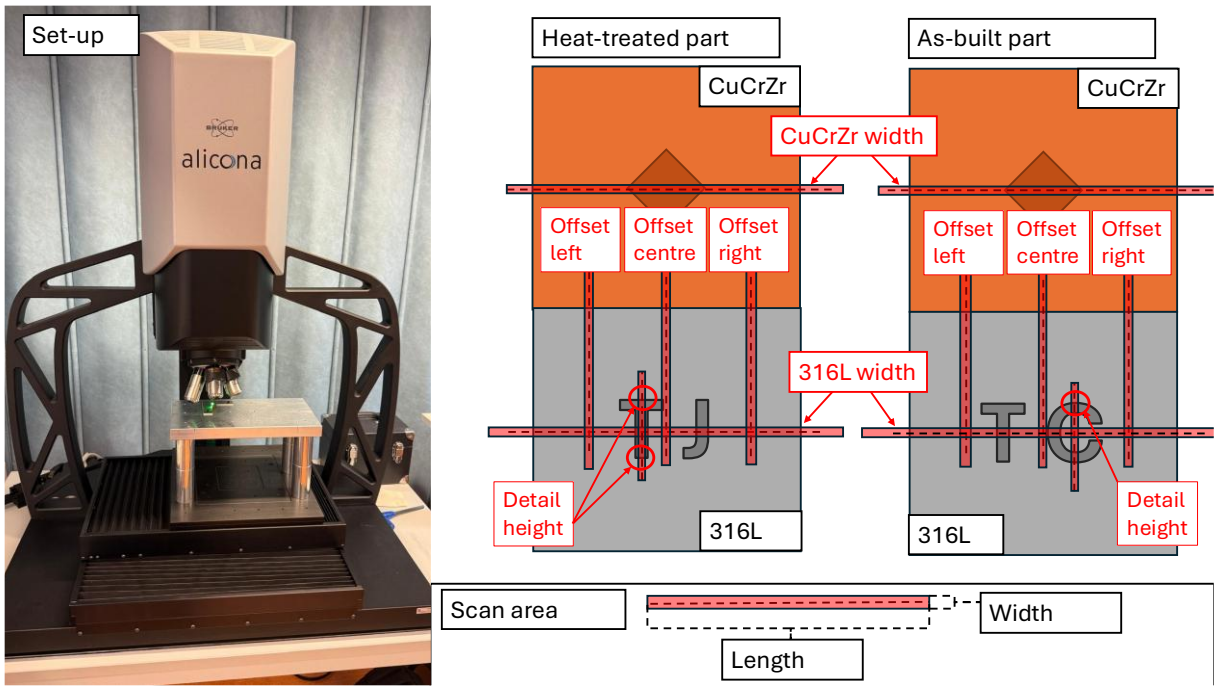

Figure 17. Geometrical accuracy measurement set-up and a schematic illustration of the scanned areas in the geometrical analysis.

Figure 17 shows the Alicona measurement set-up used to conduct the geometrical accuracy measurements and the illustrations of the analysed surfaces and measured features of the multi-material parts. Overall, six features on the surfaces of the 316L-CuCrZr parts were measured:

- The height evolution of the lettering on the surface of the parts
    - Provides information on the ability of the PBF-LB/M to produce overhanging surface details with precision.
- The widths of CuCrZr and 316L materials
    - Provides information on whether the PBF-LB/M causes size differences between 316L and CuCrZr.
- The offset height and width between the discrete materials from left, right and centre of the part.
    - The offset heights provide information on the possible alignment differences between 316L and CuCrZr.

- The offset width provides information on the amount of CuCrZr layers needed to stabilise from the overhang caused by the alignment differences.

The measurements of these features were conducted by scanning selected linear areas, shown as the red rectangles in Figure 17. The scanning resulted in a detailed point cloud of the scanned surfaces. Each scan area covered a width of 100 µm with varying lengths. The point cloud of each measured area was converted to a line graph illustrating height evolution across the length of the scanned area. The line graphs were plotted by computing the average altitude values across the widths of each linear scan areas.

The locations of each height measurement of the surface details are marked with red circles. In the as-built material, the letter "C" with the height measurement being done at the upper side of the lettering. In the heat-treated material, the letter "T" was scanned, with the height measurements being done on both upper and lower sides of the geometry of the letter.

7.3.4 Corrosion resistance test

Corrosion resistance measurements were done for as-built, HT1 and HT2 316L-CuCrZr parts, which were cut into three sections shown in Figure 18.

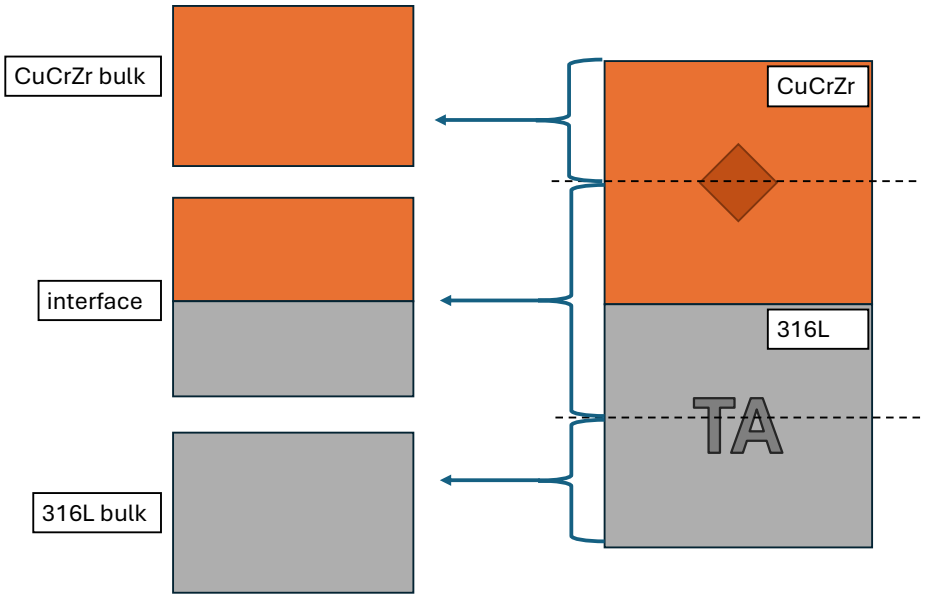

Figure 18. Schematic illustration of the sample cutting procedure for corrosion resistance and thermal conductivity tests.

As shown in Figure 18, the as-built, HT1 and HT2 316L-CuCrZr parts were cut into three separate parts: CuCrZr bulk, 316L-CuCrZr interface and 316L bulk sections, thus producing overall nine materials for corrosion measurements. Copper wires were then soldered into the cut parts using melted tin. The soldered parts were embedded in epoxy such that only one surface was left exposed. The exposed surfaces were polished using 4000# grit polishing paper. The illustrations on the left side of Figure 18 show how each material was exposed during the corrosion resistance testing.

The corrosion resistance measurements, namely *OCP* and electrochemical kinetics, were measured using the set-ups seen in Figure 19.

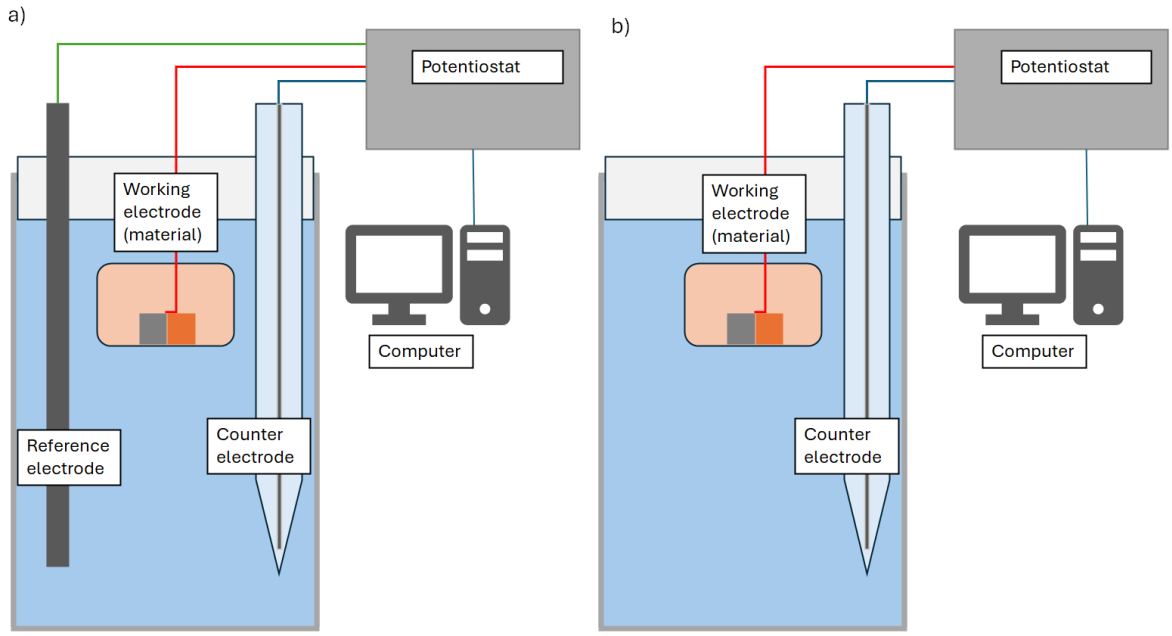

Figure 19. Schematic illustration of the a) electrochemical kinetics testing and b) *OCP* measurement set-ups.

As shown in Figure 19, two different set-ups were used to measure the *OCP* and electrochemical kinetics. The *OCP* of each epoxied 316L bulk, interface and CuCrZr bulk material parts were measured first using the set-up shown in Figure 19b. The tested material (working electrode) was put in a solution with a counter electrode, which were both connected to a potentiostat. The *OCP* measurements were run for 1h. Electrochemical kinetics of each material were then measured using the set-up shown in Figure 19a. The tested material (working electrode) was put in a solution with an Ag/AgCl counter electrode and a graphite reference electrode. All the electrodes were connected to the potentiostat. Before each electrochemical

kinetic measurement, a short 10-minute *OCP* measurement was done to verify the potential range from which the electrical currents were measured. After each electrochemical kinetic measurement, Tafel plots were plotted, and $E_{corr,}$ I_{corr} and corrosion rate values were derived with the software.

7.3.5 Thermal conductivity test

For thermal conductivity measurements, as-built, HT1 and HT2 316L-CuCrZr multi-materials were cut into 3 different sections: CuCrZr bulk, 316L bulk and 316L-CuCrZr interface (see Figure 18), thus producing a total of nine materials for tests. The thermal conductivity values of the materials were calculated from their electrical conductivity properties, namely, electrical resistance. The electrical resistances of the materials were tested using a resistance meter, as shown in Figure 20.

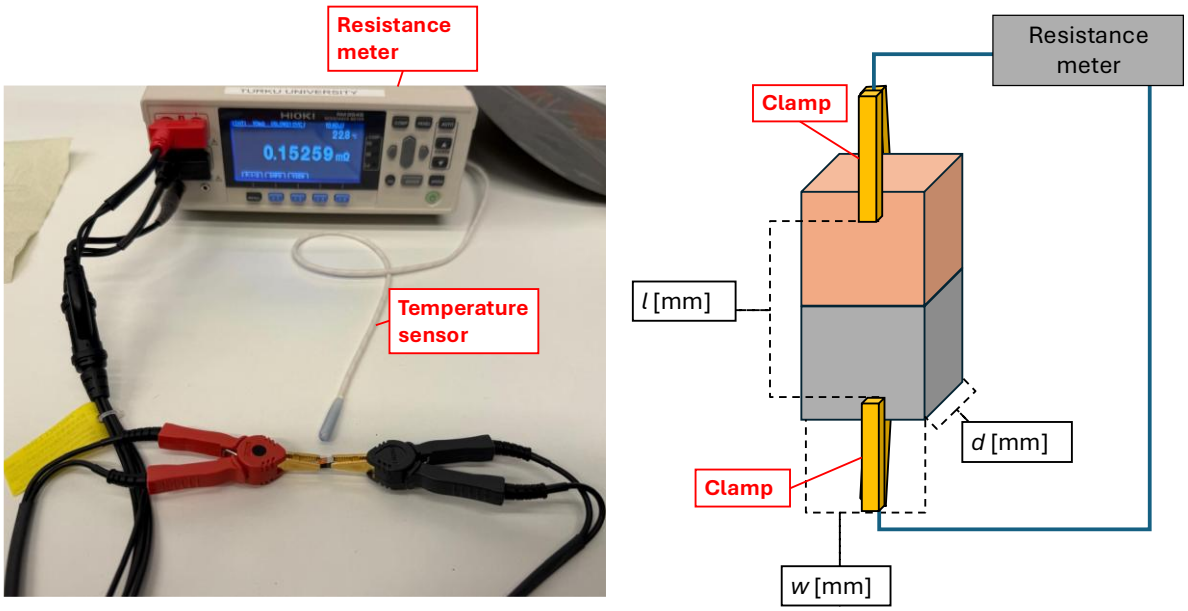

Figure 20. Image and schematic illustration of the thermal conductivity measurement set-up.

As Figure 20 shows, the electrical resistance test set-up consisted of a resistance meter, a temperature sensor and two clamps. The clamps were placed at both ends of the tested material part, and the temperature sensor was placed nearby to measure the room temperature. The resistance meter was then able to measure the electrical resistance of the connected material. Electrical resistance measurement was repeated five times on each material by readjusting the clamps to the part. Data on the following aspects were gathered on each measurement:

- Electrical resistance R (Ω)
- The room temperature T (K)
- The length of the material between the clamps l (mm)
- The width of the tested part w (mm)
- The depth of the tested part d (mm)

The data gathered from the measurements were then used to calculate the electrical resistivity ρ using Equation 4, where electrical resistance R, depth d and width w of the material part are multiplied and divided by the length between the clamps l (Lowrie & Fichtner, 2020).

$$\rho = R\frac{d * w}{l} \qquad (4)$$

The Wiedemann-Franz law was then used to calculate the theoretical thermal conductivities λ (W/mK) of the measured materials (see Equation 3). A more precise explanation and demonstration of the thermal conductivity calculations is provided in Appendix 2 Example calculations of thermal conductivity.

8 Results and Discussion

8.1 Parameter optimisation results

After ultrasonic cleaning, the 316L-CuCrZr parts manufactured using parameter combinations of *P* of 390W and *v* of 625 W, as well as *P* of 380 W and *v* of 675 mm/s (see Table 8), started to show visible roughness and porosity on the polished CuCrZr surface. This damage was suspected to be caused by the ultrasonic cleaning, and these parts were discarded as a result. However, the causation of this material-damaging effect needs further study.

The *defect-%* values of the microscopically imaged 316L-CuCrZr interfaces, AMed by each parameter combination, calculated by the defect analysis program, can be seen in

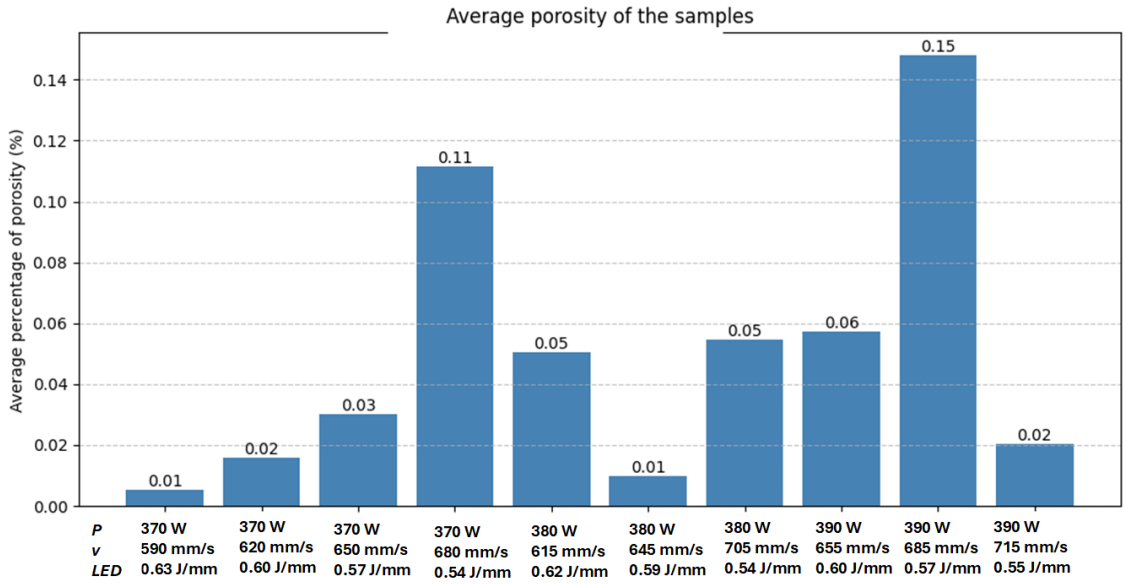

Figure 21.

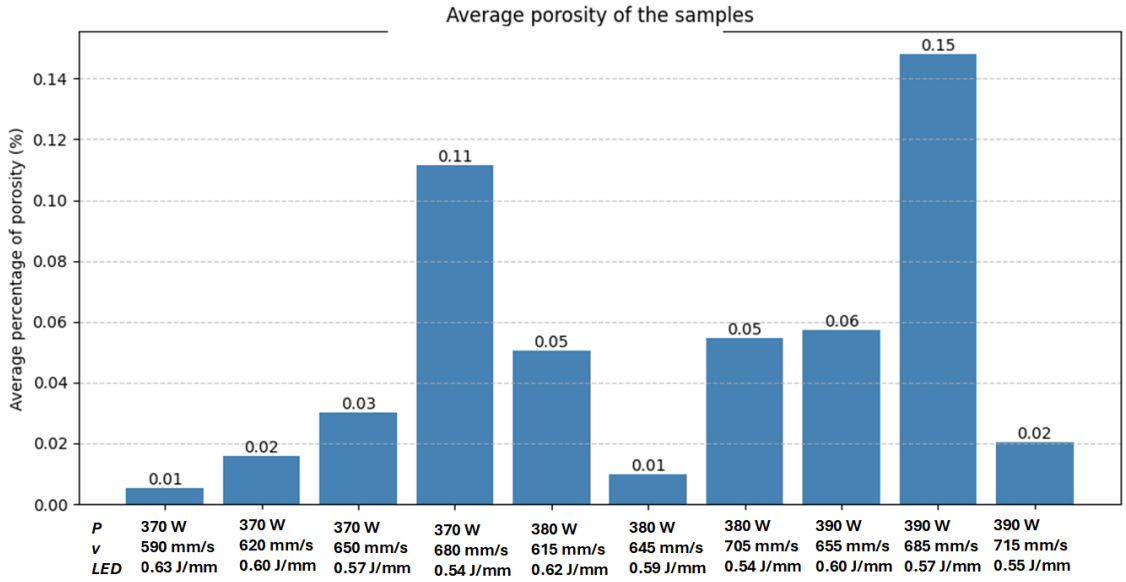

Figure 21. Average *defect-%* values of all different parameter combinations (*P*, *v* and *LED*) of PBF-LB/Med 316L-CuCrZr.

As shown in

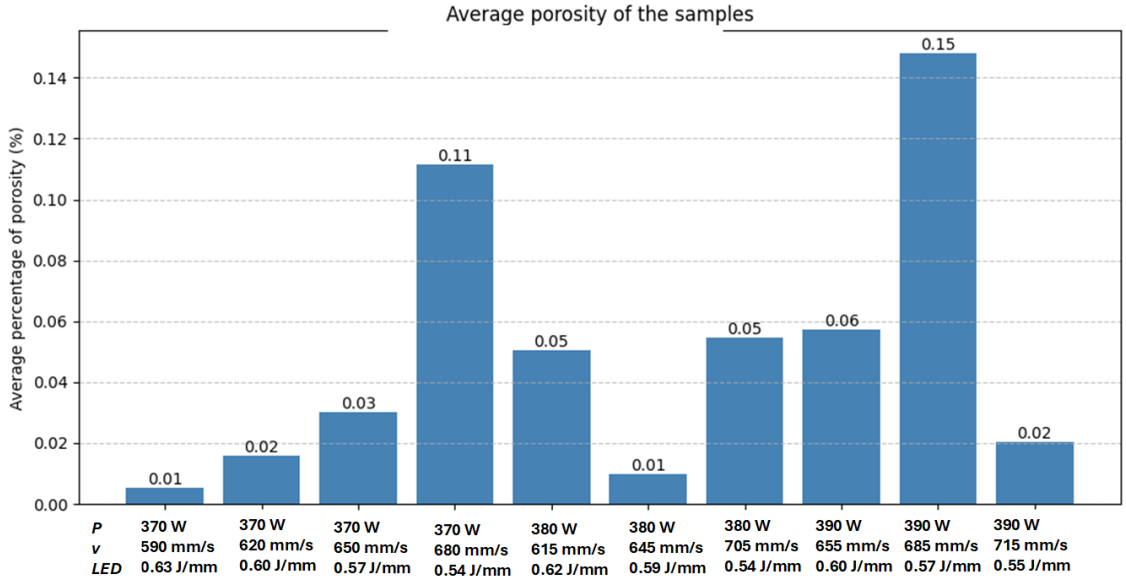

Figure 21, no clear correlation between the perceived defects, mainly porosity, and the process parameters or the energy density can be observed. However, when the *P* was constant at 370 W, the porosity seemed to increase with the scanning speed. The increase in porosity could have been a result of imperfect powder particle melting of the highly reflective CuCrZr material, due to a decrease in energy density. The rest of the parameter combinations using

constant *P* values of 380 W and 390 W do not show any linear increase or decrease in measured porosity for unknown reasons, which require further study. As

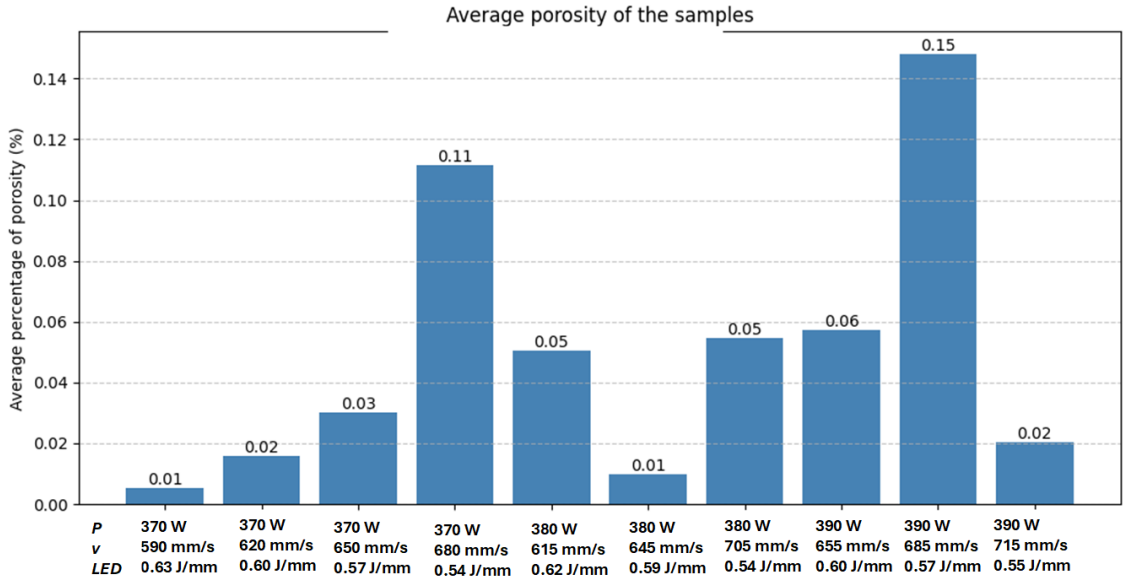

Figure 21 shows, the parameter combination of *P* of 370 W and *v* of 590 mm/s had the lowest porosity of 0.01 % and was therefore chosen for the manufacturing of the material testing samples.

Example images of the parameter combinations with the least and the most detected defects, i.e. with the lowest and the highest *defect-%* values, in the 316L-CuCrZr interface are shown in Figure 22.

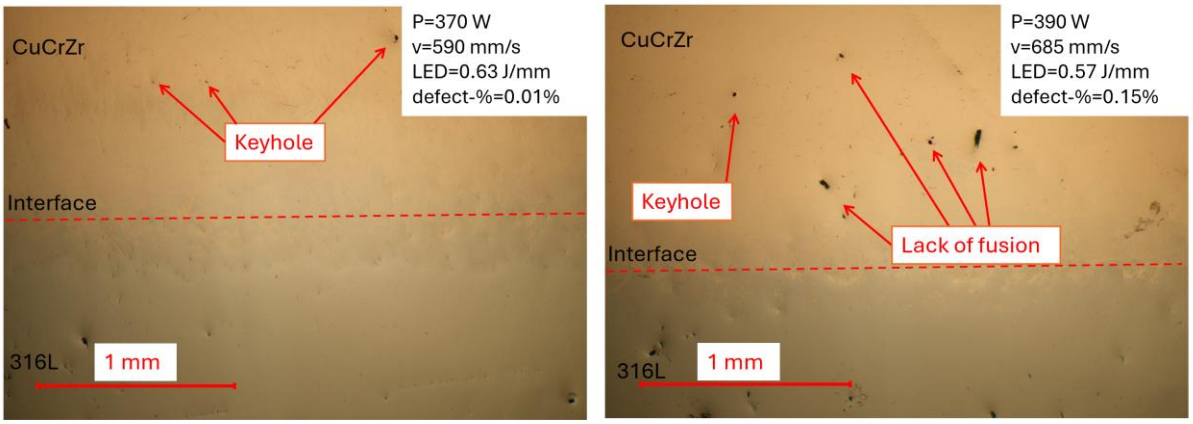

Figure 22. Example microscope images of the 316L-CuCrZr interface parameter combinations with the lowest (left) and highest (right) *defect-%* values.

Figure 22 shows the example microscopic images of the 316L-CuCrZr interfaces manufactured using the parameter combinations which had the smallest amount (left) and largest amount (right) of detected defects. The interface of 316L and CuCrZr of any parameter combination did not show visible cracking in the 316L side, which was an improvement over the results expected based on the literature review (see Chapter 2.3). The parameter combinations of *P* of 370 W and *v* of 590 mm/s (see Figure 22, left image) produced mostly dense material with a few small and spherical pores. Due to the visual characteristics of these pores as well as the high energy density of the parameter combination, it was hypothesised that these pores were keyhole porosity. The parameter combination of *P* of 390 W and *v* of 685 mm/s (see Figure 22, right image) produced CuCrZr material with more visible porosity. These pores were larger than the keyhole pores and irregular in size, and were therefore hypothetised to be lack of fusion porosity by the author. In conclusion, using PBF-LB/M combinations with a high *LED* around 0.63 J/mm is likely to produce a denser interface of 316L-CuCrZr due to the reflectivity and thermal conductivity of CuCrZr.

8.2 Material testing results

8.2.1 Metallographic analysis

Example microscope images and their defect-analysed counterparts of as-built, HT1 and HT2 316L bulk materials are collected in Figure 23.

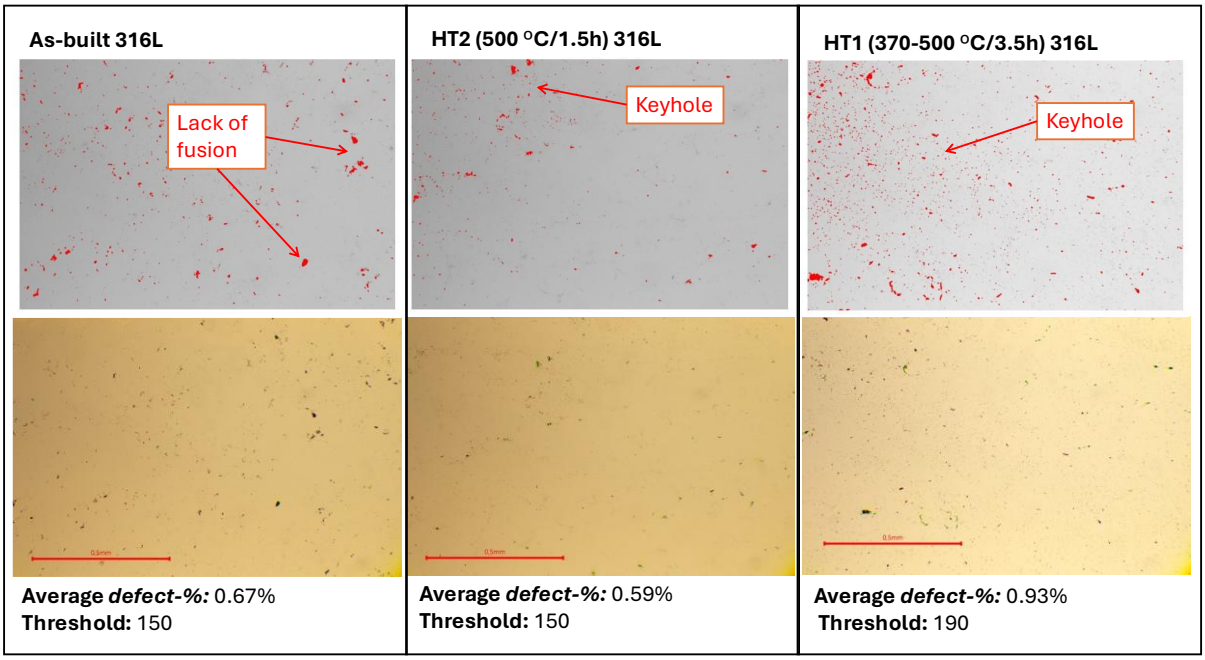

Figure 23. 316L bulk microscope images (lower), their defect analysed versions (higher) and average *defect-%* values of as-built (left), HT2 (middle) and HT1 (right) materials. The scale bar in the microscope images shows a length of 0.5 mm.

As shown in Figure 23, the 316L bulk images exhibit both keyhole and lack of fusion porosity, which are commonly caused by either too high or too low energy density of the process parameters. It is therefore hypothesised by the author that these pores could be caused by old and oxidised 316L powder, as the *LED* values being simultaneously too high and too low is unlikely. The average *defect-%* value of HT1 316L bulk is 0.26-0.34% higher than as-built and HT2 316L bulk materials, which had *defect-%* values of 0.67% and 0.59%. Bedmar et al. (2022) noted a similar increase in porosity in their PBF-LB/Med and heat-treated 316L. This phenomenon was hypothesised to be caused by the expansion of the trapped gas in the material during the heat treatment process (Bedmar et al., 2022). In conclusion, the as-built and HT2 316L bulk exhibited some lack of fusion and keyhole porosity, the exact causation for which is not known apart from perhaps improper process parameters or oxidised 316L powder. However, the high amount of keyhole-type porosity in HT1 316L bulk could have been caused by thermal expansion of gases trapped in the material.

Example CuCrZr bulk microscope images and their defect-analysed counterparts of the as-built, HT1 and HT2 are collected in Figure 24.

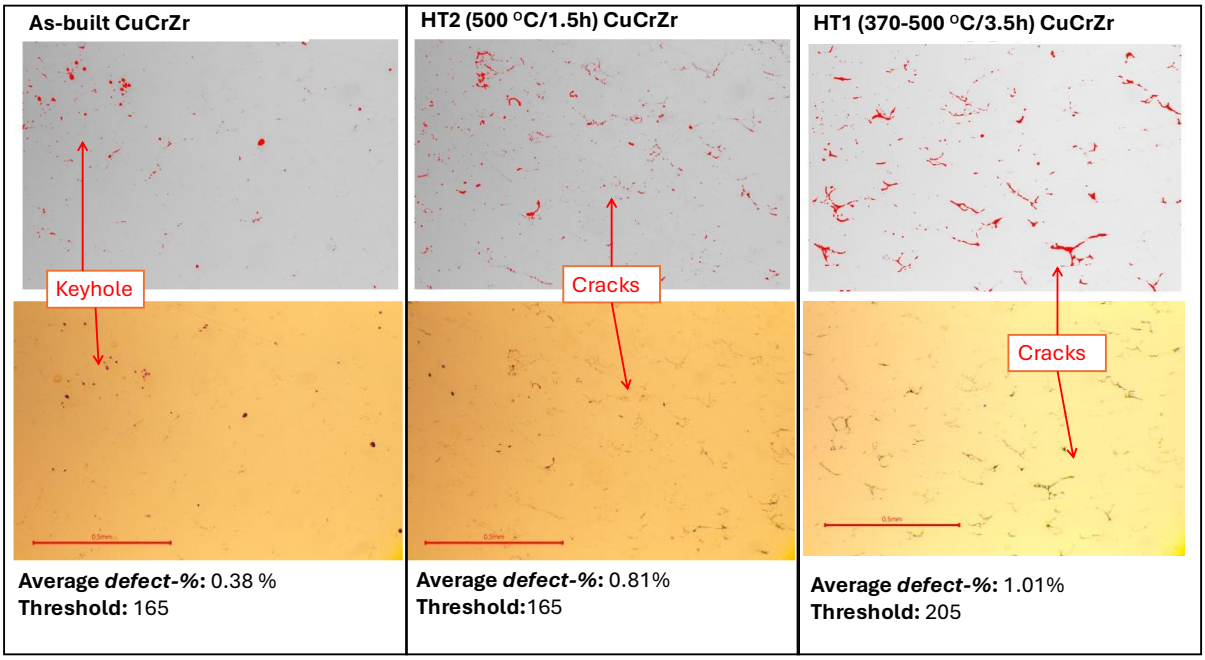

Figure 24. CuCrZr bulk microscope images (lower), their defect analysed versions (higher) and average *defect-% values* of as-built (left), HT2 (middle) and HT1 (right) materials. The scale bar in all of the microscope images shows a length of 0.5 mm.

As Figure 24 shows, the CuCrZr bulk *defect-%* values increase the longer the material is heat-treated, due to cracking. The image in the as-built CuCrZr bulk shows mainly small and circular keyhole porosity, computing to an average *defect-%* value of 0.38%. The amount of porosity is not affected by the heat treatment; however, this requires further study, as the image analysis program is not able to distinguish cracking from porosity. The *defect-%* values of the CuCrZr images in TH1 and TH2 CuCrZr bulk are 0.81% and 1.01% respectively. The cracking is suspected to be caused by the expansion and shrinkage of the material during heat treatment (Wallis & Buchmayr, 2019). The cracking could also be caused by the release of residual stresses left in the CuCrZr bulk material from too high *LED* process parameters, which were optimised mainly for the 316L-CuCrZr interface.

Example microscope images of the 316L-CuCrZr interfaces of as-built, HT1 and HT2 materials, and their defect-analysed versions are collected in Figure 25.

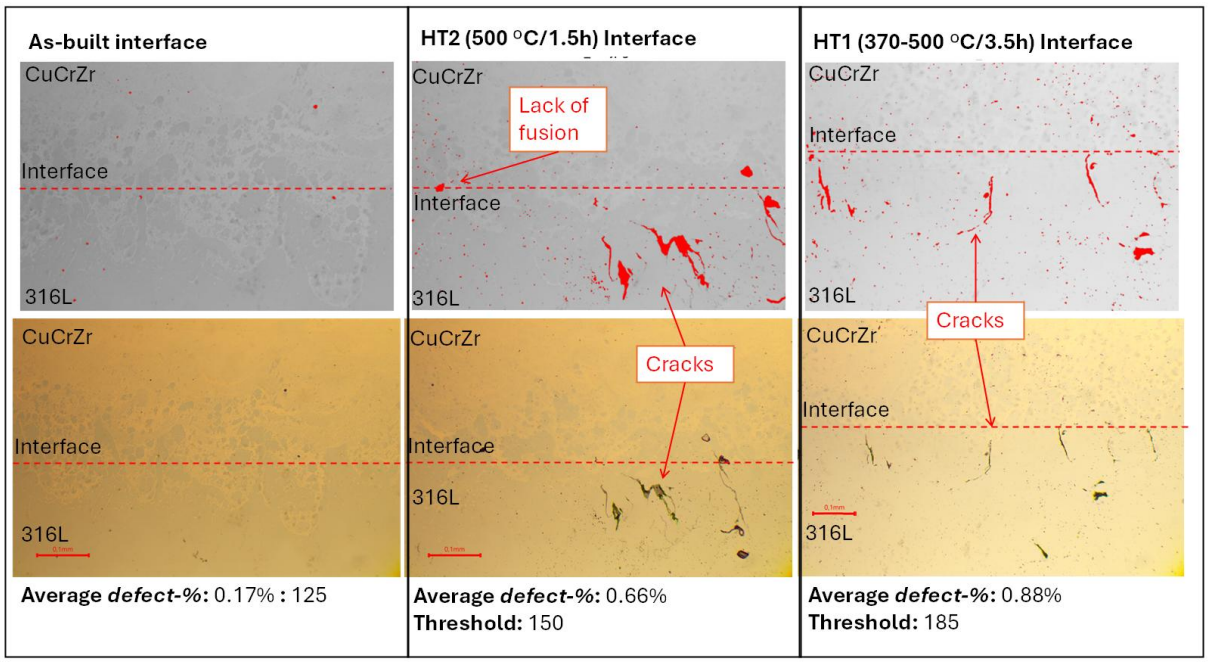

Figure 25. Microscope images (lower), their defect analysed versions (higher) and average *defect-%* of as-built (left), HT2 (middle) and HT1 (right) 316L-CuCrZr interfaces. The scale bar in the microscope images shows a length of 0.1 mm.

Figure 25 shows that the microscope images of the as-built 316L-CuCrZr interface exhibit a solid, crack-free material bonding, which is assumed to be a result of a high enough energy density in the process parameters. The defect analysed version of the as-built interface image exhibits small circular red areas, which are hypothetised to be keyhole pores by the author due to their small and circular sizes. This indicates that the selected process parameters can produce high-density material bonding between 316L-CuCrZr, as the high-energy density enables proper mixing of 316L and CuCrZr. The images of the HT2 and HT1 316L-CuCrZr interface show a higher amount of porosity as well as cracking on the side of 316L. Based on these observations, the cracking of the 316L-CuCrZr interface happens during or after heat treatment. The most probable cause of cracking is suspected to be the stresses caused by the materials expanding at different rates during the heat treatment process (Meyer et al., 2025).

Etching of the samples revealed interesting microscopic patterns on the CuCrZr, such as formations reminiscent of laser scan tracks (see Figure 26).

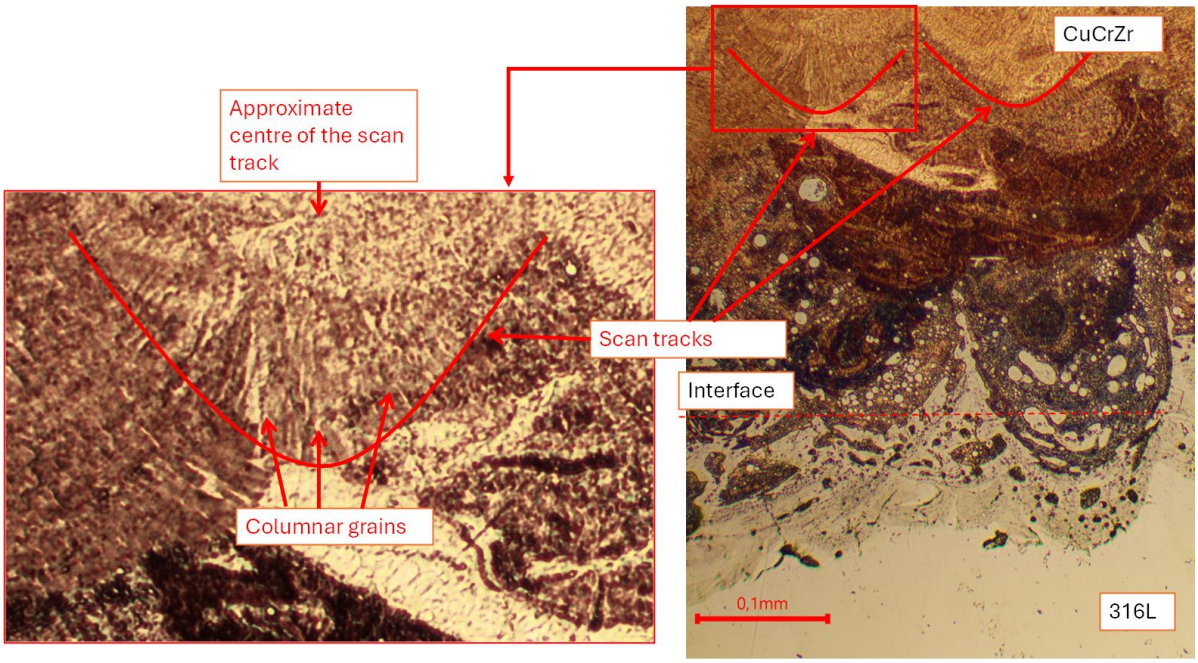

Figure 26. A scan track and the columnar grains inside it in the etched HT1 multi-material. The scale bar in the original microscope image (right) shows a length of 0.1 mm.

As seen in Figure 26, the scan tracks consist of columnar subgrains that have formed in the build direction and turn slightly towards the centre of the scan track grain (Liu et al., 2014). This phenomenon is caused by the tendency of the molten material to solidify in the direction of the thermal gradient, which is, in this case, increasing towards the upmost centre of the scan track (see Figure 26), where the laser beam hits the material. These columnar grains seem to appear most clearly a few layers from the interface. Liu et al. (2014) studied the microstructural characteristics of AMed stainless steel-copper alloy interface and noticed that the interface had smaller grains, which exhibited more random growth direction. It would seem that the results of this thesis follow the same pattern. However, further research with SEM or electron backscatter diffraction (EBSD) imaging would be required to confirm this.

Inspection of the etched 316L-CuCrZr interface revealed information on the material bonding of 316L and CuCrZr and other phenomena present in their interface during the PBF-LB/M process (see Figure 27)

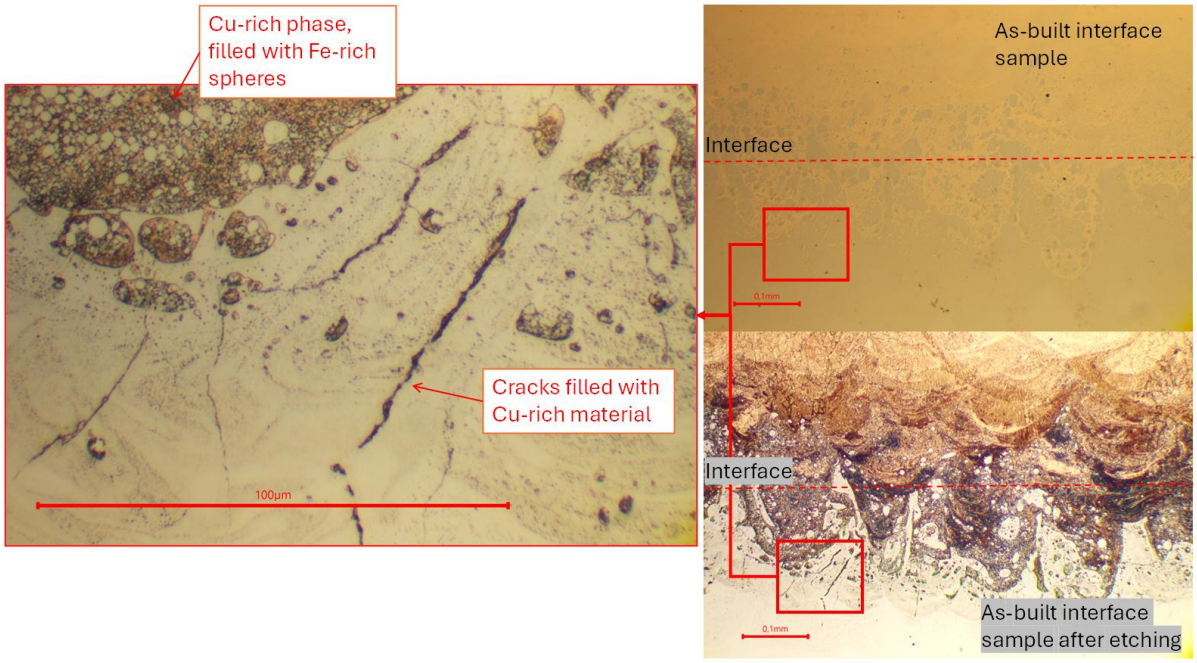

Figure 27. Material bonding and phase distribution in the 316L-CuCrZr interface

Figure 27 shows the discrete CuCrZr and 316L phase distribution in the interface region II (see Chapter 2.3). In the high magnification image, Fe-rich spherical phases in Cu-rich matrix are revealed. This precipitation-type behaviour is probably caused by the different solidification rates of 316L and CuCrZr (Kuai et al., 2023). After melting the CuCrZr powder onto a 316L surface, the materials momentarily mix into a semi-homogeneous substance (Kuai et al., 2023). As the melt pool starts to solidify, the Fe atoms in the Cu-rich material start to condense into Fe-rich spheres (Kuai et al., 2023). These images also showed crack-like areas in the Fe-rich areas, usually starting from a Cu-rich phase (see Figure 27). These crack-like areas were shaped similarly to cracks seen in the interfaces of the heat-treated materials. These crack-shaped areas were filled with Cu-rich material, which is hypothesised by the author to be the reason why they weren't visible before etching. To the knowledge of the author, no similar phenomenon has been reported in the literature at the time of writing the thesis. It is hypothesised that these crack-like, Cu-rich features formed during the PBF-LB/M process. A liquid Cu-rich phase, trapped within the solidified 316L matrix, likely induced cracking in the surrounding material and subsequently filled the resulting voids. Cracking of the 316L material near the interface is

also hypothetised to be caused by CCC, where the molten CuCrZr had penetrated the 316L between the grains and caused cracking (Deillon et al., 2024).

8.2.2 Microhardness test

Figure 28 shows the results of the microhardness tests of the as-built 316L-CuCrZr multi-material.

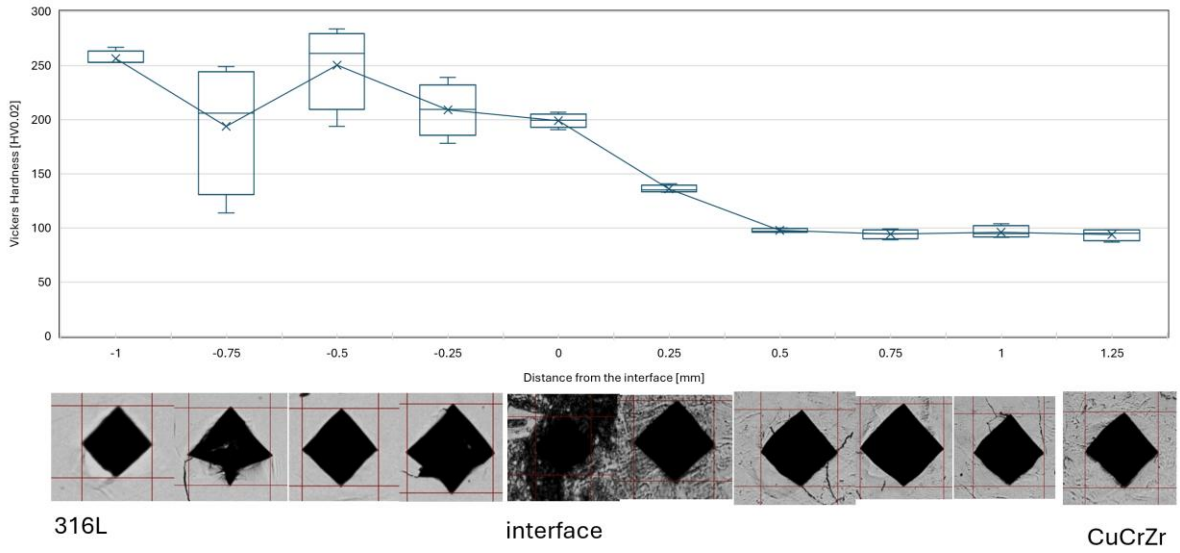

Figure 28. Microhardness results and measurement point images of the as-built 316L-CuCrZr.

Figure 28 shows the variance between the microhardness results of the as-built 316L-CuCrZr part. On average, the hardness results are similar to the values achieved in the study by Meyer et al. (2025), whose measured hardnesses for as-built CuCrZr and 316L were 80-130 HV0.2 and 220-260 HV0.2, respectively (see Chapter 4.2). The microhardness of the 316L measured around 225 HV0.2, varying in the 125-280 HV range. The reason for the variance in the microhardness of 316L is uncertain and requires further studies. However, it is suspected that the variance could be caused by defects, including the porosity observed in the metallographic analysis (see Chapter 8.2.1). Figure 28 shows that CuCrZr microhardness values measured consistently near 100 HV0.2, apart from the measurement point at 0.25 mm from the interface, which measured around 140 HV0.2. The increase in microhardness at this particular point near the interface is suspected to be caused by the remelting of the first five CuCrZr layers from the interface (see Figure 13a). The heat deposition of the remelting could have caused precipitation, therefore strengthening the remelted CuCrZr material. In conclusion, the microhardnesses of the as-built 316L-CuCrZr multi-material were measured to perform similarly to the studies

Meyer et al. (2025). The microhardness values were suspected to be affected by metallographic defects on the side of 316L and remelting on the side of CuCrZr.

Figure 29 shows the results of the microhardness tests of the HT1 316L-CuCrZr multi-material.

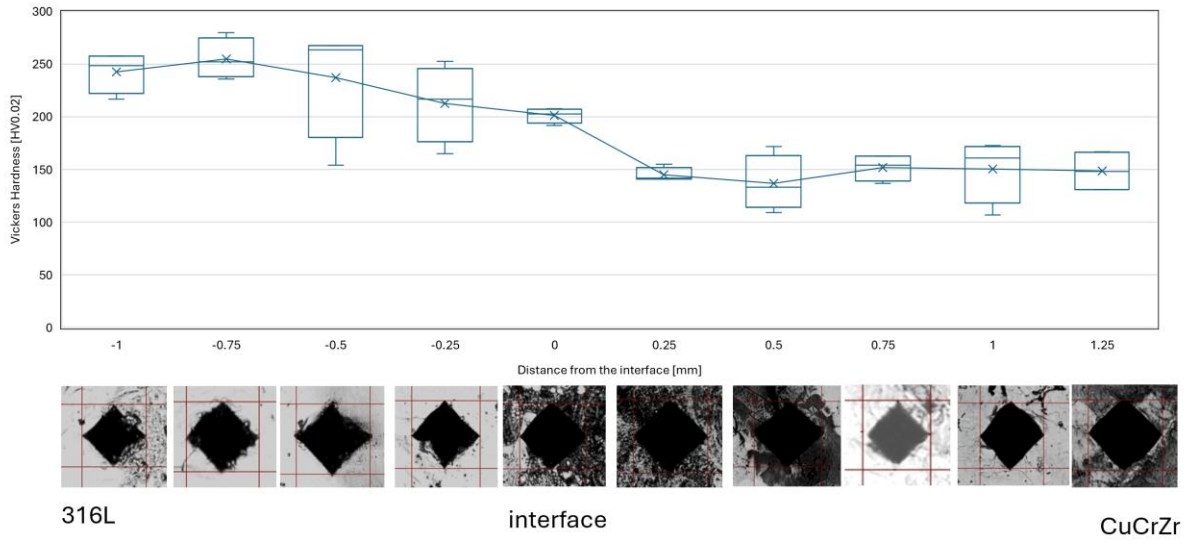

Figure 29. Microhardness results and images of the HT1 316L-CuCrZr multi-material.

As Figure 29 shows, the microhardness values of CuCrZr have increased from 100 HV0.2 to 150 HV0.2 after the heat treatment HT1. This increase in CuCrZr microhardness values follows the same pattern as was observed in previous studies by Meyer et al. (2025), in which the microhardness of CuCrZr increased from 80-130 HV0.2 to 110-230 HV0.2 after DAH heat treatment (see Chapter 4.2). The increase in CuCrZr microhardness is hypothesised by the author to be caused by the precipitates formed during the heat treatment process. The microhardness of 316L was not affected by the heat treatment, and the average hardness stayed 225 HV0.2. This is also consistent with the results by Meyer et al. (2025), whose 316L microhardness values remained 220-260 HV0.2 before and after the heat treatment. In conclusion, HT1 increased the microhardness of the CuCrZr by approximately 50 HV0.2 without affecting the microhardness of the 316L.

Figure 30 shows the results of the microhardness tests of the HT2 316L-CuCrZr multi-material.

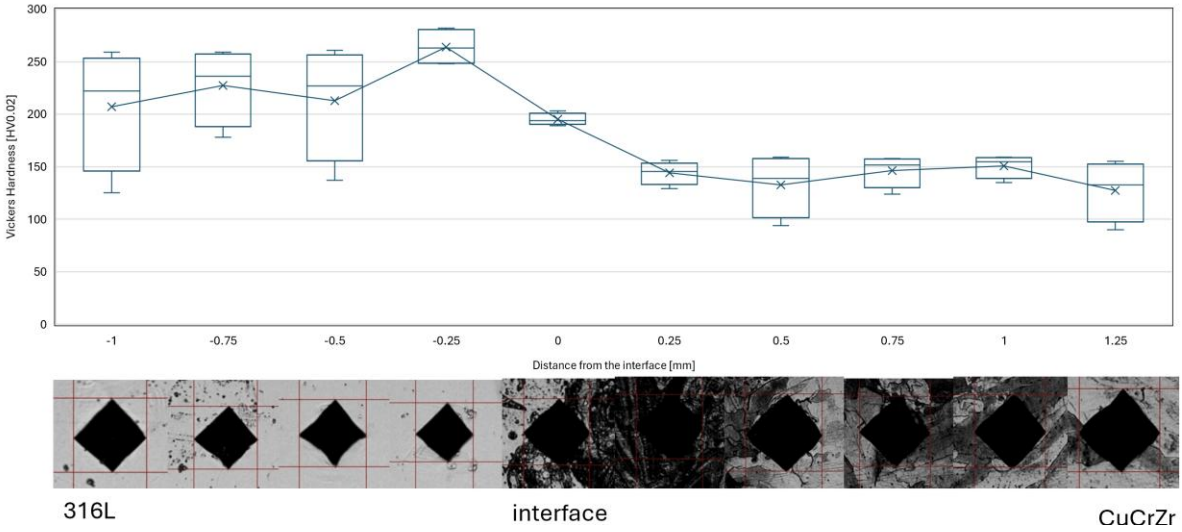

Figure 30. Microhardness results and measurement point images of the HT2 316L-CuCrZr multi-material.

Figure 30 shows the microhardness results of the HT2 316L-CuCrZr multi-material, whose microhardness values are very similar to the corresponding results of the HT1 316L-CuCrZr (see Figure 29). The average microhardness values of the 316L and CuCrZr are around 225 HV0.2 and 150 HV0.2, respectively, which again follow the observations of CuCrZr microhardness increase after DAH from the research by Meyer et al. (2025) (see Chapter 4.2). The average microhardnesses in the interface (0 mm from the interface) of the as-built, HT1 and HT2 316L-CuCrZr multi-materials measured around 200 HV0.2 with slight variability. In conclusion, HT2 increased the microhardness of the CuCrZr by approximately 50 HV0.2 without affecting the microhardness of the 316L.

8.2.3 Geometrical accuracy measurement

In the original CAD of the sample, both materials were planned to be manufactured in the same alignment, directly on top of each other, thus having no offset between the discrete materials. Each of the three offset measurements calculated the height (y-axis) and the width (x-axis) of the offset. The centre offset measurement of the as-built multi-material failed and was therefore discarded, as the measurement points were placed in the wrong places. Offset measurements of the as-built 316L-CuCrZr multi-material are depicted in Figure 31.

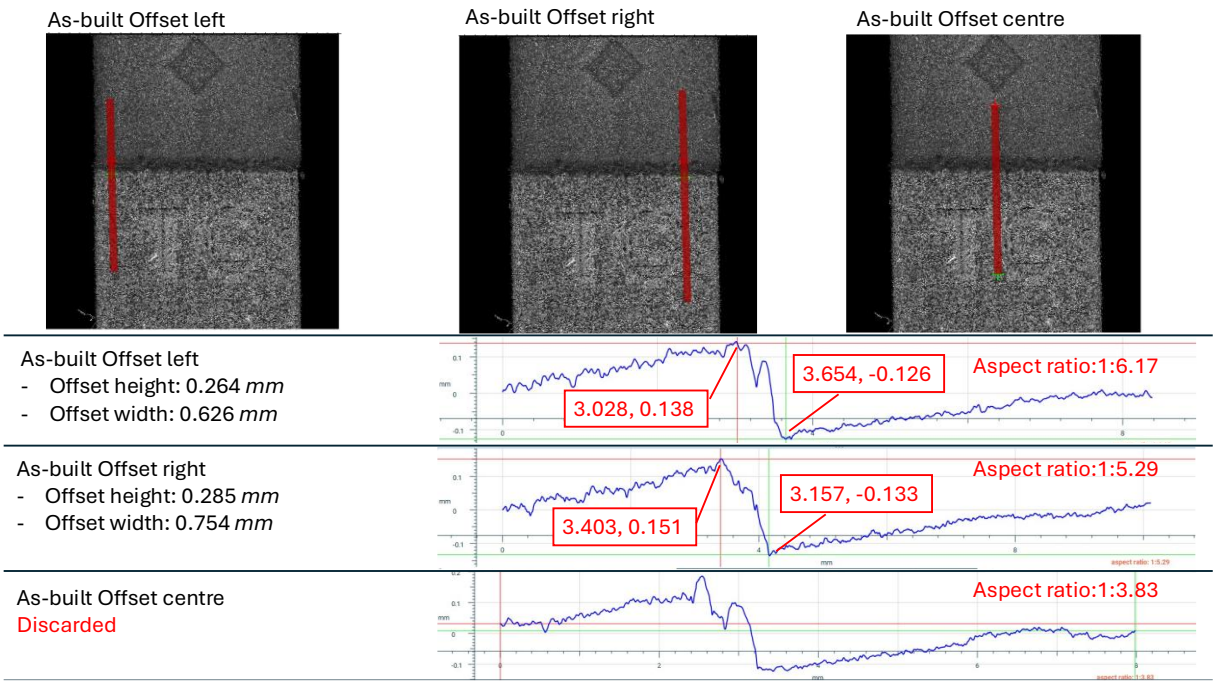

Figure 31. Geometrical accuracy measurements of the material interface offset in the as-built 316L–CuCrZr parts (top), and corresponding line graphs showing the scanned profiles and measured offset height and width values (bottom).

Figure 31 shows that the as-built 316L-CuCrZr multi-material had a slight variation in the material interface offset, visible in the surface roughness graphs. The measurement coordinates are marked in the boxes with red outlines. The offset heights of the left and right measurement areas were 0.26 mm and 0.29 mm, respectively, with the total difference of the two values being 0.02 mm. This offset difference is hypothesised by the author to be caused by a marginal rotation of the build plate during the material changing process in PBF-LB/M of the 316L-CuCrZr parts.

The offset widths of the right and left as-built offset measurements were 0.63 mm and 0.75 mm, respectively. The offset widths indicate the amount of material built before the stabilised CuCrZr material and are defined as the distance between the points where the straight build-directional 316L surface ends and where the CuCrZr material starts to stabilise after the offset. The layer thickness during manufacturing was 0.03 mm, which would suggest that the stabilisation of the CuCrZr offset took approximately 21-25 layers.

The offset measurements of the heat-treated 316L-CuCrZr interface are collected in Figure 32.

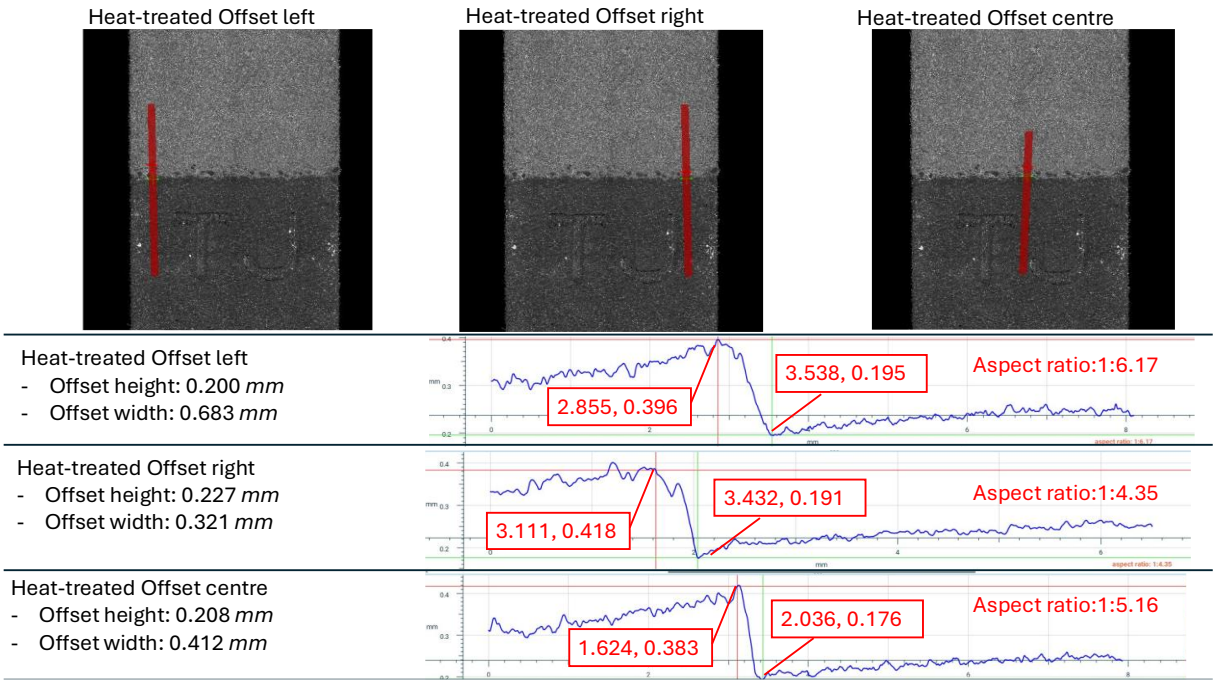

Figure 32. Geometrical accuracy measurements of the material interface offset in the HT1 316L–CuCrZr parts (top), and corresponding line graphs showing the scanned profiles and measured offset height and width values (bottom).

Figure 32 shows the geometrical accuracy measurements of the material offset in the heat-treated material. The measured offset heights in the left, centre and right areas were 0.20 mm, 0.21 mm and 0.23 mm, respectively. These results in the offset height measurements align with the hypothesis that the gradually increasing offset height could be caused by unintentional build plate rotation during the material changing process in the PBF-LB/M of 316L-CuCrZr parts. Widths of the left, right and centre offset measurements were 0.68 mm, 0.32 mm and 0.41 mm, respectively, which would suggest that the stabilisation of the overhanging CuCrZr offset took approximately 16-34 layers in the heat-treated material.

The results of the width measurements of the as-built CuCrZr and 316L geometries can be seen in Figure 33.

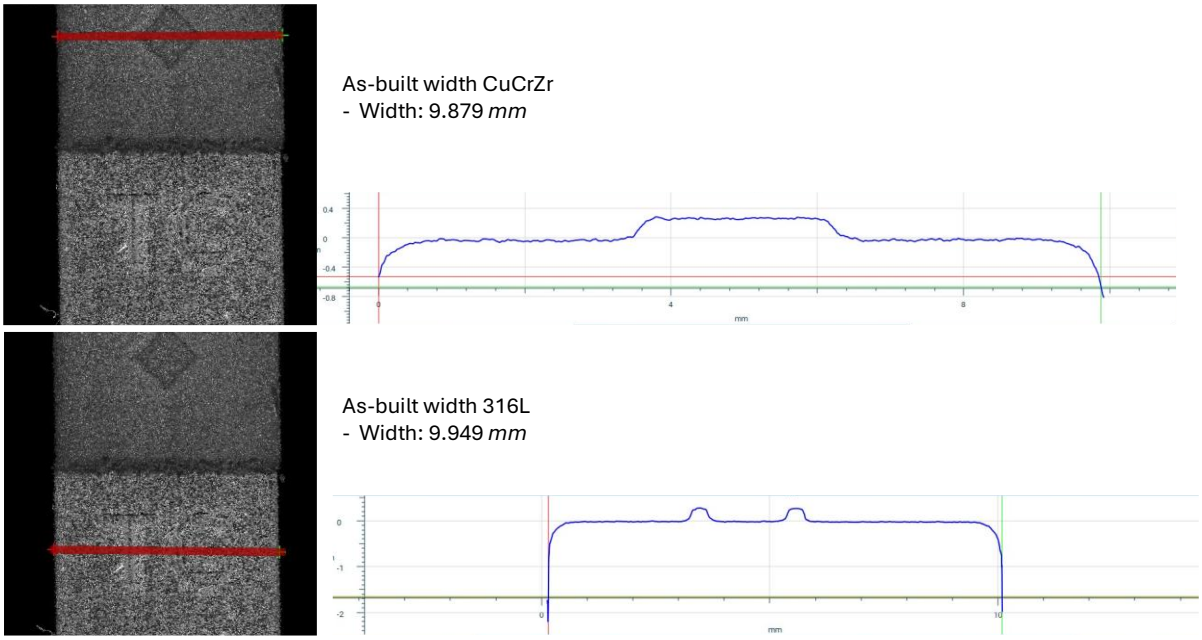

Figure 33. Geometrical accuracy measurements of the widths of the as-built CuCrZr and 316L(left top and left bottom), and corresponding line graphs showing the scanned profiles and measured width values (right top and right bottom).

Figure 33 shows the width measurements of the as-built 316L and CuCrZr materials. The dimensions of the CuCrZr and 316L cuboids were designed to be 10 mm. The width measurements of the CuCrZr and 316L were 9.88 mm and 9.95 mm, respectively. The differences in the real-life widths to the original CAD were 0.12 mm with the CuCrZr and 0.05 mm for the 316L.

The width measurements of the heat-treated 316L and CuCrZr geometries are visualised in Figure 34.

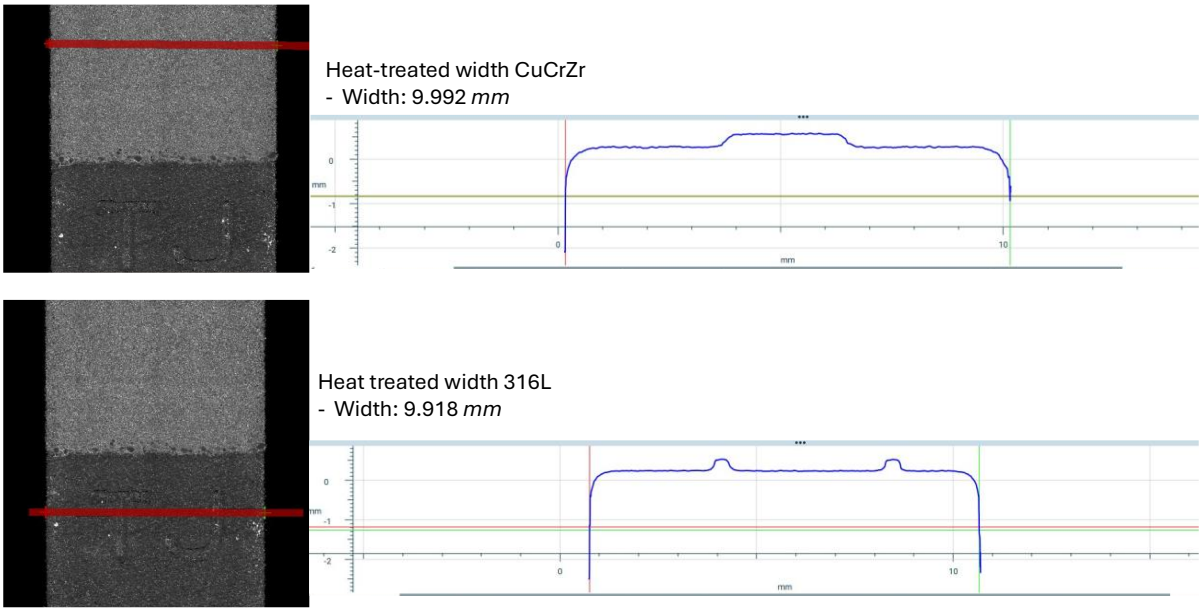

Figure 34. Geometrical accuracy measurements of the widths of the HT1 CuCrZr and 316L(left top and left bottom), and corresponding line graphs showing the scanned profiles and measured width values (right top and right bottom).

Figure 34 shows the width measurements of the heat-treated multi-material. The dimensions of the CuCrZr and 316L cuboids were designed to be 10 mm. The measurements of the CuCrZr and 316L were 9.99 mm and 9.92 mm, respectively. Both widths were very close to the original CAD design, with a 0.008 mm difference with the CuCrZr and 0.081 mm difference with the 316L, with the difference of the CuCrZr material cuboid being 0.074 mm larger than the 316L. The shrinkage of the manufactured materials was hypothetised by the author to be caused by a volumetric difference between the powder and the melted material. The laser scans the powder bed based on the dimensions of the CAD. As the powder melts, the material solidifies into a denser and slightly smaller component.

The measurements of the height of the lettering manufactured on the multi-material surface are depicted in Figure 35.

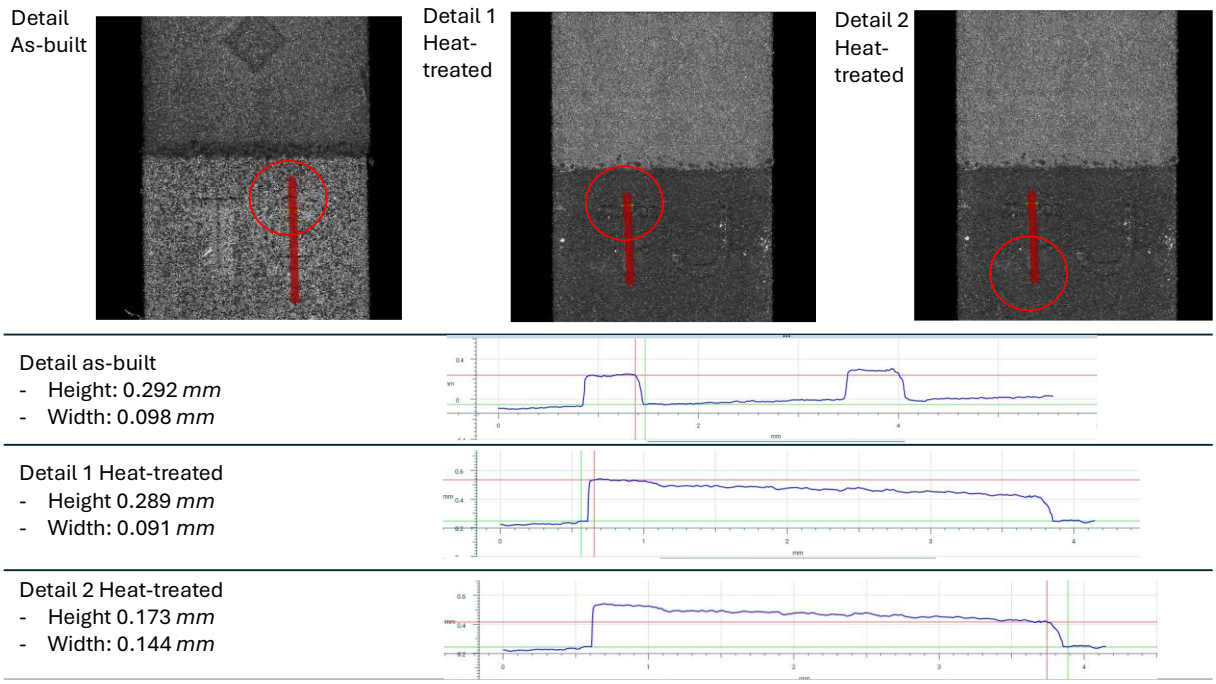

Figure 35. Geometrical accuracy measurements of the heights of the lettering of the as-built and HT1 316L, with circled area where height measurements were taken (top), and corresponding line graphs showing the scanned profiles and measured height values (bottom).

Figure 35 shows the surface graph of the areas over the letterings on the as-built and heat-treated materials. As the lettering in the heat-treated material was measured at two points, the measurements were marked as Detail 1 and Detail 2 (see Figure 35). The locations of each height measurement are marked with red circles. The offset in the material interface caused a slight tilting of the measured surface, which can be seen in the surface maps. The height of the lettering in the CAD was 0.30 mm from the surface. The measured height of the as-built Detail was 0.29 mm, and the heights of the heat-treated Details 1 and 2 were 0.29 mm and 0.17 mm, respectively (see Figure 35). The difference between the lettering heights of the as-built Detail and the heat-treated Details 1 and 2 to the CAD account to 0.01 mm, 0.01 mm and 0.13 mm, respectively. This accuracy, especially of the as-built Detail and the heat-treated Detail 1, could be enabled by the relatively small scale of the lettering. In the heat-treated Detail 1 measurement point, the geometry was sharp and highly accurate, as the lower sections of the letter functioned well as the supporting surface for the material melting (see Figure 35). However, the lower sections of the letter “T”, namely the heat-treated Detail 2, had a 0.12 mm decrease in height compared to the heat-treated Detail 1. This decrease could be explained either by the challenges in the material melting without supports or by the tilted measuring area, which covers an increasing amount of flat surface, thus lowering the surface average in the surface graph.

8.2.4 Corrosion resistance test

The *OCP* graphs and values of the as-built and HT1 and HT2 316L bulk are collected in Figure 36.

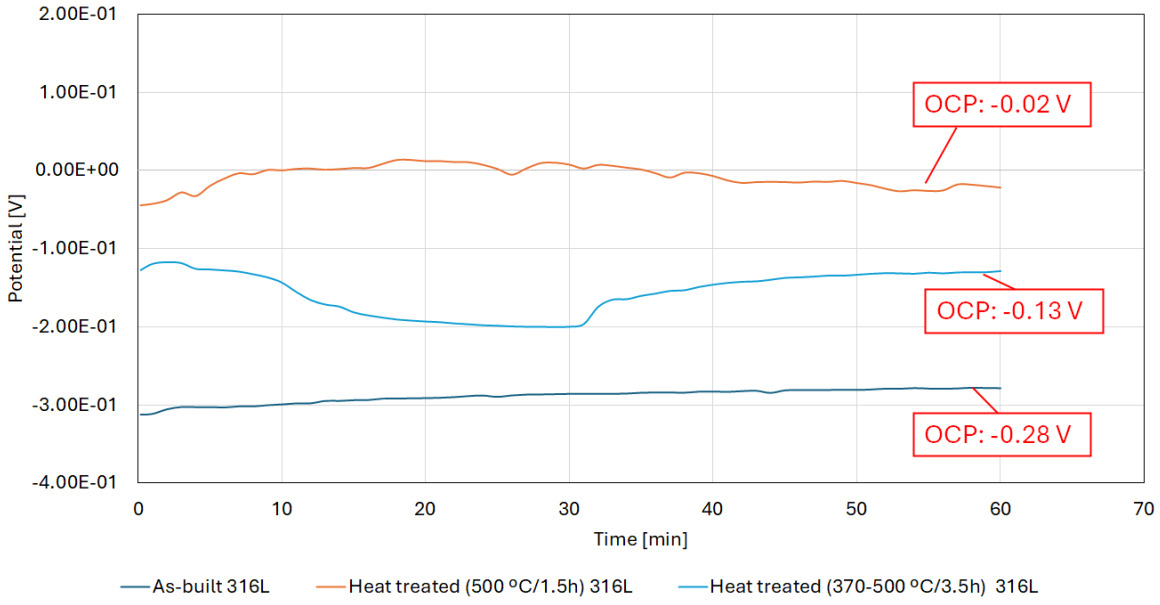

Figure 36. *OCP* graphs and values of as-built, HT1 and HT2 316L bulk materials.

As seen in Figure 36, the *OCP* values of the 316L bulk vary depending on the post-processing they had received. The as-built 316L bulk measured a -0.28 V *OCP* value, which increased to -0.13 V after HT1 and to -0.02 V after HT2. The increase in the *OCP* values could be caused by the phase changes in the 316L microstructure. These changes in the *OCP* values indicate a significant improvement in the corrosion resistance of the 316L after heat treatment, as the corrosion potentials moved closer to 0 V. The *OCP* values of the heat-treated 316L are similar to the values from a study by Bedmar et al. (2022), who measured *OCP* values of -0.04 V and -0.17 V, after heat treating 316L at 650 °C for 2 h and at 400 °C for 4 h (see Table 3), respectively. The *OCP* value measured by Bedmar et al. (2022) of the as-built 316L was -0.13 V, which varied the most from the *OCP* value of -0.28 V of the as-built 316L measured in this thesis. The reason for this difference is unknown to the author and therefore requires more research, although it is suspected that the differences could be caused at least partially by the differences in the *OCP* measurement set-up and procedure, such as the materials used or the immersion time.

The *OCP* values of the as-built and both heat-treated CuCrZr bulk materials are collected in Figure 37.

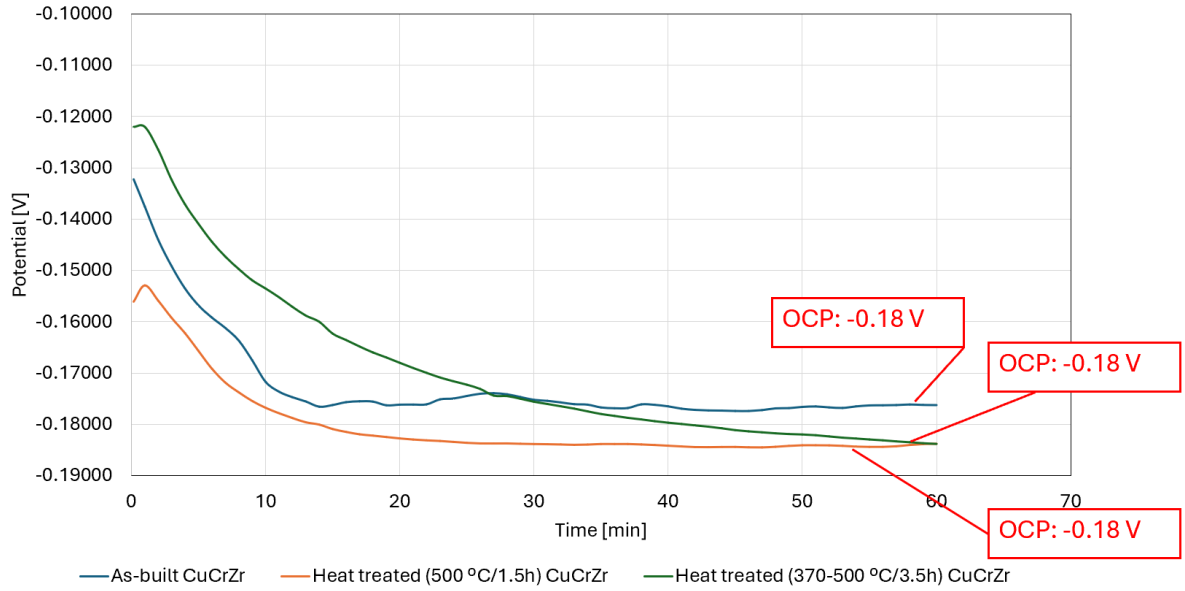

Figure 37. *OCP* graphs of as-built, HT1 and HT2 CuCrZr bulk materials.

As Figure 37 shows, the *OCP* graphs and values of all the CuCrZr bulk materials are close to each other, resulting in values near -0.18 V. The only difference between the measurements was the marginal decrease of the *OCP* after heat treatment. This indicates that the heat treatment would have had a slight decreasing effect on the corrosion resistance of CuCrZr and making the material less noble. However, as the *OCP* decrease is so small, it could also be caused by other factors, such as surface roughness, impurities or surface oxidation, which could have happened in between the polishing and testing. Another potential factor causing changes in the *OCP* could be the cracking of the CuCrZr bulk after heat treatment (see Figure 24). These results are similar to the *OCP* value of -0.19V measured by Kwok et al. (2009) from as-built CuCrZr, which indicates that the OCP value is universal for this particular material (see Table 3).

The *OCP* measurements of the as-built, HT1 and HT2 interface parts are collected in Figure 38

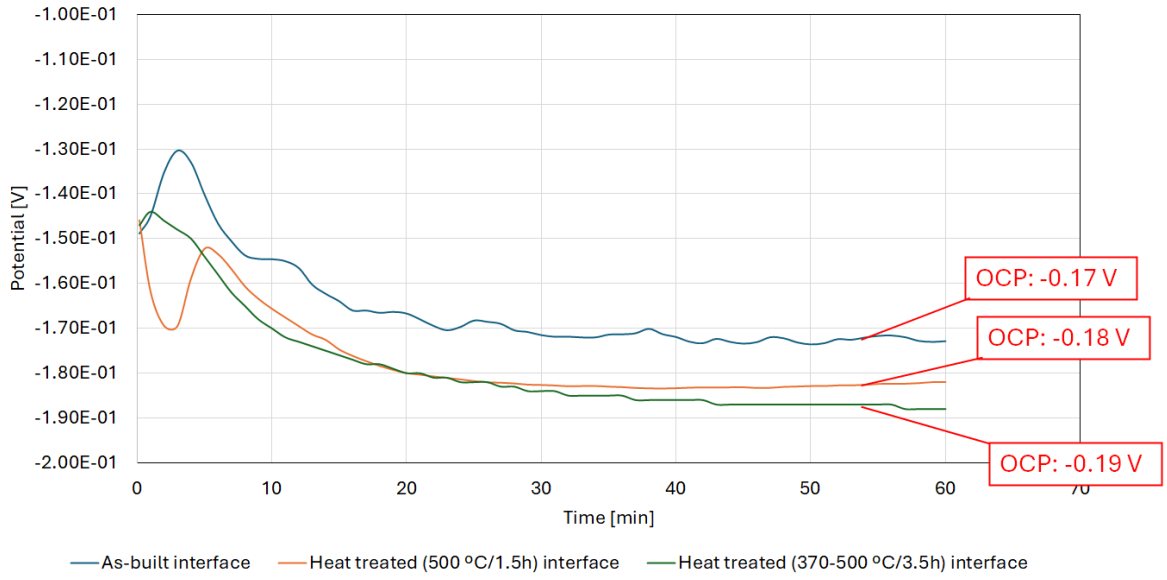

Figure 38. *OCP* graphs of the as-built, HT1 and HT2 316L-CuCrZr interface materials.

Figure 38 shows that the *OCP* evolution of the interface material resembles the results of CuCrZr bulk material (see Figure 37). The *OCP* of the as-built interface has the highest *OCP* value of -0.17 V, which is slightly above the -0.18V of the as-built CuCrZr. Interestingly, the influence of the low *OCP* value of the as-built 316L material (-0.28V) has no decreasing effect on the *OCP* value of the 316L-CuCrZr interface (see Figure 36). This could indicate that the corrosion resistance of the 316L-CuCrZr multi-materials is caused primarily by the CuCrZr rather than the 316L. However, this hypothesis of the corrosion properties of multi-materials being determined by one material would require further research. The *OCP* value of the HT1 interface is almost -0.18 V, and the *OCP* value of the HT2 interface is -0.19V. This decrease in the *OCP* values after HT1 and HT2 would mean that the heat treatments increase the corrosion potential of the multi-material 316L-CuCrZr. This corrosion potential increasing effect is hypothesised by the author to be caused by the cracking in the 316L-CuCrZr interface caused by heat treatment, which would increase the surface area exposed to a corrosive environment.

The E_{corr} values of all the tested materials are collected in Figure 39.

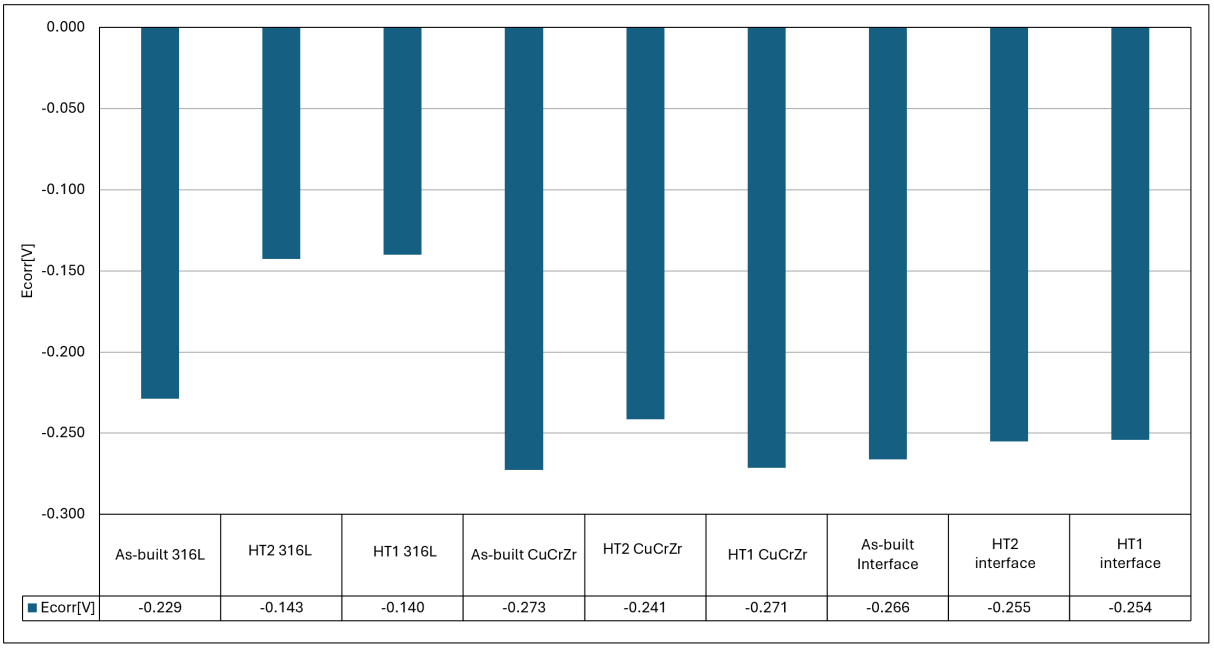

Figure 39. Corrosion potential values (E_{corr}) of all the as-built, HT1 and HT2 variants of 316L bulk, CuCrZr bulk and 316L-CuCrZr interface materials, respectively.

As Figure 39 shows, E_{corr} values of the 316L are generally more positive compared to those of CuCrZr or the 316L-CuCrZr interface, indicating that the 316L is more noble than the other materials. The E_{corr} values of the 316L were observed to increase after heat treatment. This increase in nobility of 316L after heat treatment was also seen in the *OCP* measurements of the 316L (see Figure 36). The increase in the E_{corr} values could be caused by the phase changes in the 316L microstructure during heat treatment. It was also observed that the E_{corr} values were more positive compared to the corresponding results of Hemmasian Ettefagh et al. (2018) (see Table 3).

All of the CuCrZr and the 316L-CuCrZr interface materials measured E_{corr} values relatively close to each other (see Figure 39), which aligns with the hypothesis that the corrosion behaviour of the 316L-CuCrZr multi-material is largely determined by the properties of CuCrZr. Unlike in 316L or the *OCP* measurements of the CuCrZr and 316L-CuCrZr multi-material, heat treatment doesn't seem to have any clear effect on the corrosion potential of the CuCrZr or the 316L-CuCrZr interface. The reason for this requires further study, as the previously conducted research on the effects of heat treatments on the corrosion resistance of the CuCrZr is limited.

The I_{corr} values and corrosion rates of all the materials and post-processes are collected in Figure 40.

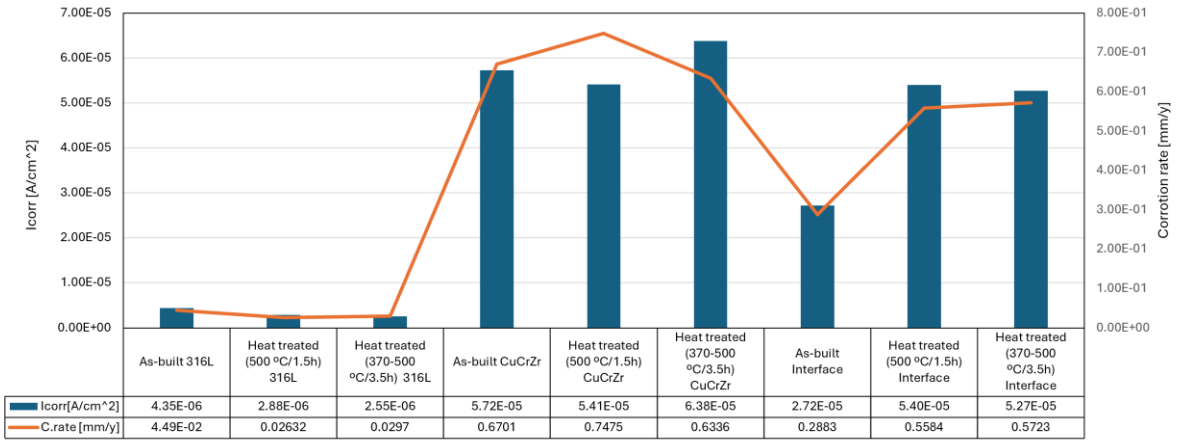

Figure 40. The I_{corr} and corrosion rate [mm/y] values for all the as-built, HT1 and HT2 variants of 316L bulk, CuCrZr bulk and 316L-CuCrZr interface materials, respectively.

As Figure 40 shows, the values of I_{corr} and corrosion rates seem to correlate with each other, with the exception of HT2 CuCrZr. The I_{corr} values are lowest with 316L materials and decrease after heat treatment, similarly to the results of Hemmasian Ettefagh & Guo (2018) (see Table 3). The I_{corr} values of CuCrZr and the 316L-CuCrZr interface materials are visibly higher than those of 316L and do not seem to be affected by any of the performed heat treatments. The I_{corr} values of the CuCrZr are similar to those measured by Dongfang et al. (2024) (see Table 3).

Figure 40 also shows that the corrosion rates of the 316L bulk are lower than CuCrZr bulk or 316L-CuCrZr interface materials. During comparison, it was noticed that the corrosion rate of the 316L decreases from 0.04 mm/y to approximately 0.03 mm/y after heat treatment. The CuCrZr measured in the range of 0.63-0.75 mm/y, with the HT1 CuCrZr bulk having the highest corrosion rate. The corrosion rate of the interfaces increased after heat treatment from 0.29 mm/y to 0.56-0.57 mm/y (see Figure 40). This increase in corrosion rate could be caused by the increased difference in the E_{corr} values of the respective 316L and CuCrZr bulk materials after heat treatment. The E_{corr} values of the heat-treated 316L and CuCrZr bulk materials have a higher difference compared to their as-built counterparts (see Figure 39). When materials are combined into multi-materials, materials with a smaller difference in their individual E_{corr} values also have a smaller corrosion rate as a multi-material (*2019 Department of Defense - Allied Nations Technical Corrosion Conference COMPUTATIONAL CORROSION ANALYSIS GUIDES MATERIAL CHOICE FROM DESIGN THROUGH SUSTAINMENT*, n.d.).

8.2.5 Thermal conductivity test

The results of the thermal conductivity measurements of all the analysed materials are gathered in Figure 41.

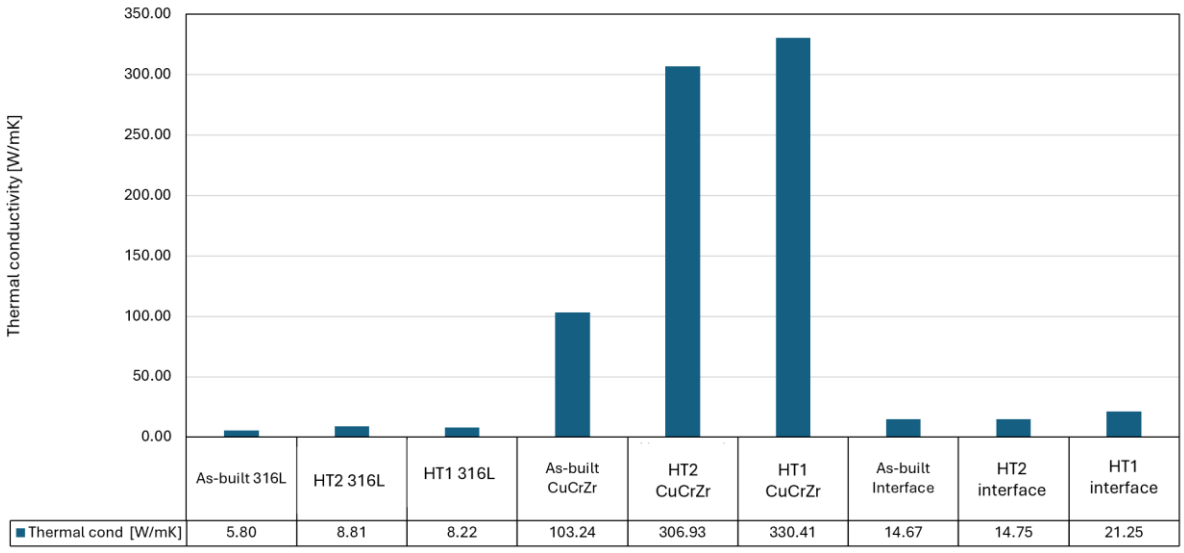

Figure 41. Average values of computed thermal conductivities of all the measured materials and post-processes.

As shown in Figure 41, the CuCrZr bulk materials exhibited the highest thermal conductivity, ranging between 103 and 330 W/mK. The 316L bulk and 316L-CuCrZr interface materials have relatively similar thermal conductivities, ranging between 5.80 and 8.22 W/mK and 14.7 and 21.3 W/mK, respectively. The thermal conductivities of the 316L bulk and CuCrZr bulk correlate with values found in the literature (see Table 4), which indicates that the PBF-LB/M and thermal conductivity measurement processes were successful and repeatable. The literature review findings exhibited a similar, about 200 W/mK, increase in thermal conductivity of CuCrZr bulk material after heat treatment. This increase in thermal conductivity was found to be caused by the precipitation of Cr and Zr atoms, which reduces the dislocation density and the scattering effect in the Cu-matrix (see Chapter 4.5) It is hypothesised by the author that the increase in thermal conductivity of the 316L-CuCrZr interface materials compared to the 316L bulk materials (see Figure 41) is caused by the presence of the highly conductive CuCrZr material. It is also hypothesised by the author that this increase in conductivity is limited by the scattering effect caused by cracking, porosity, phase changes and other microstructural aspects present in the 316L-CuCrZr material interface.

9 Conclusions

In this thesis, the manufacturing and properties of PBF-LB/Med 316L-CuCrZr multi-material were successfully studied through a literature review and empirical experimentation.

Literature on previous multi-material stainless steel-copper PBF-LB/M studies was reviewed to compile information about relevant process parameters, post-processing techniques, sample preparation workflow, material testing methods and material properties. AMing CuCrZr using process parameters with an *LED* of around 0.67 J/mm was found to be able to produce the most dense and defect-free 316L-CuCrZr interface. DAH at 500 °C for 1.5 h was found to be the most suitable post-processing method to increase microhardness and corrosion resistance of CuCrZr without losing the high tensile strength and other properties of AMed 316L.

The preliminary parameter optimisation tests aimed to find a PBF-LB/M process parameter combination able to produce the densest 316L-CuCrZr interface. This parameter combination was then used to manufacture the 316L-CuCrZr parts used in the material tests. The samples were divided into three groups: as-built, and the samples heat-treated with the 1st and the 2nd heat treatment methods, referred to as HT1 and HT2, respectively.

The 316L-CuCrZr parts were then used to conduct metallurgical analysis, geometrical accuracy measurements, corrosion resistance tests and thermal conductivity tests. After completing the experimental work, the original research questions could be answered thusly:

- The metallographic analysis revealed information about how different heat treatment methods affected the 316L bulk, CuCrZr bulk and 316L-CuCrZr interface. As-built 316L bulk was observed to be visibly exhibiting porosity, which seemed to increase after heat treatment, possibly due to trapped gas expansion and “stretching” of the pore borders. The as-built CuCrZr bulk exhibited minor cracking, which was also expanded after heat treatment. The as-built interface was observed to be relatively defect-free apart from minor porosity. After heat treatment, the 316L side of the interface started to crack, starting from Cu-rich phases. It was hypothesised that this cracking was caused by differences in the thermal expansion of CuCrZr and 316L, causing accumulation of residual stresses.
- The microhardness testing was conducted using the Vickers microhardness HV0.2 measurement method with a 1.964 N load and a dwell time of 10 seconds. The as-built, HT1 and HT2 316L-CuCrZr multi-materials were tested 4 times in a line of 10 measurement points lined across the interface. According to the results, all of the 316L measured a

hardness of 200-250 HV0.2 and were not changed by the heat-treatment. The hardness of the CuCrZr material increased after heat-treatment from 100 HV0.2 to 150 HV0.2. This increase in CuCrZr hardness was hypothesised to be caused by precipitation from the age hardening heat treatment process.

- Geometrical accuracy was measured from as-built and heat-treated (HT1) 316L-CuCrZr multi-material parts. A 3D microscope was used to measure the material offset by measuring the height changes across the interface, the width of the sample from the sides of both materials and the precision of the surface details by measuring the heights of the lettering embedded on the inspected surface. The results of both materials implied that the heat treatment did not affect the measured geometrical properties. The offset height difference between the materials measured 0.20-0.29 mm, in a way that suggested that the build plate twisted slightly during the PBF-LB/M process. The material widths measured around 9.88-9.99 mm, having a marginal difference from the 10 mm width of the original CAD. The heights of the surface details measured to be 0.17-0.29 mm, which were also very close to the 0.3 mm lettering height in the original CAD.

- Corrosion testing was conducted in two parts: first by measuring the *OCP*, and then E_{corr}, I_{corr} and corrosion rate values derived from a Tafel extrapolation. As-built, HT1 and HT2 316L-CuCrZr multi-materials were cut and measured as three parts: CuCrZr bulk, 316L bulk and interface. It was observed that the corrosion tendencies of the CuCrZr and the interface materials were similar (E_{corr} values approximately -0.25 V) and not affected by heat treatment. The corrosion potential measured from the 316L decreased from -0.23 V to -0.14 V after both of the heat treatments. The corrosion rates exhibited more variance between the materials, with the 316L having the lowest (0.03-0.04 mm/y) and the CuCrZr material having the highest corrosion rates (0.67-0.75 mm/y), with the interface falling between these (0.30-0.57 mm/y).

- The thermal conductivities of the CuCrZr bulk, 316L bulk and 316L-CuCrZr interface materials were derived by measuring their electrical resistivity with a resistometer and converting using Wiedemann-Franz law. The results showed that CuCrZr materials had the highest thermal conductivities of 300-330 W/mK, the 316L bulk had the lowest thermal conductivities of 5.80-8.81 W/mK, and the 316L-CuCrZr interface material had thermal conductivities in between 14.7-21.2. W/mK. Overall, the thermal conductivities increased in all materials after heat treatment. This increase in thermal conductivity was hypothesised

by the author to be caused by stress relief and precipitation of the Cr and Zr impurities, which decreases the scattering of the thermal energy in the material.

9.1 Further Studies

The literature review and material testing done in the thesis were done to lay a groundwork for further research on the multi-material PBF-LB/M of the 316L-CuCrZr material. However, the full understanding of the subject requires further research into the material characteristics and the manufacturing process itself. Due to time and resource constraints faced during the production of the thesis, many intended material property tests needed to be cut, including wear resistance and tensile testing. Additionally, the number of 316L-CuCrZr testing parts was limited, which made the validation challenging and dependent on other literature on the subject. In future studies, validation of the measurements and material tests would therefore be necessary.

9.1.1 PBF-LB/M process and sample preparation and post-processing

The process parameter optimisation of PBF-LB/M of CuCrZr was concentrated on the production of the interface and optimal bonding of the 316L and CuCrZr. However, as was noticed during the metallographic analysis (see Chapter 7.3.1), these optimal parameters produced a highly cracked CuCrZr bulk material. Therefore, the parameters should be different and optimised separately for the 316L-CuCrZr interface and CuCrZr bulk to produce dense and crack-free multi-material. Additionally, different scan strategies should be researched in the production of the 316L-CuCrZr interface and the CuCrZr bulk.

The heat treatment of the 316L-CuCrZr multi-materials was done in a room atmosphere without any shielding gas, due to constraints on resources. This predictably caused oxidation and flaking of the sample surfaces. To preserve the surface quality, heat treatment should be conducted in a shield gas atmosphere. Additionally, the used heat treatment methods were observed to succeed in improving the microhardness of the CuCrZr as well as to have caused cracking in the material interface. Therefore, additional optimisation studies on the heat treatment of 316L-CuCrZr materials would be necessary. In Chapter 8.2.2, it was noticed that remelting of the CuCrZr near the interface achieved a similar increase in microhardness to the heat treatment without observable cracking of the CuCrZr bulk or interface.

The polishing and grinding processes of the multi-material were also found to be challenging due to the different material properties. It was suspected that the removal of the 316L and CuCrZr caused a type of contamination in the grinding and polishing equipment, thus creating scratches or porosity in the same surface. Therefore, the preparation of the 316L-CuCrZr multi-material requires further optimisation and possibly even implementation of more precise grinding and polishing techniques.

9.1.2 Material testing

Due to the constraints of time and resources during the thesis's production, all of the material tests would benefit from further and more in-depth research. The metallographic analysis of 316L-CuCrZr material was done using an optical microscope, which makes analysing the grains and crystal structures challenging. Therefore, in-depth analysis using SEM and EBSD would be needed.

Microhardness measurement revealed more than optimal variation, especially with the 316L. This was suspected to be due to problems with the measured materials, unpredictable material properties, or defects. The most notable change recommended by the author for future research on the microhardness would be to increase the number of samples used in each of the tests and to improve sample preparation to produce an even tested surface.

Geometrical accuracy tests conducted in the thesis were successful, and were able to compare the differences in the real-life features and the original CAD. To the best knowledge of the author, no standardised method of measuring the geometrical accuracy of the PBF-LB/Med components exists. Therefore, other more precise methods could be used for measuring the geometrical accuracy of the PBF-LB/M. Additionally, measurements could also be conducted on more than one side of the sample, revealing beneficial information on larger-scale 3-dimensional geometry distortion.

Corrosion resistance tests, especially tests for the *OCP,* are often run for long periods of time (1 h or longer). Due to time constraints, the *OCP* was measured for only 1 h in the thesis, possibly not giving enough time for the results to stabilise. Corrosion tests would also benefit from having more repeatability, as some of the samples simply did not perform as they would likely otherwise have performed. Sample preparation must be carried out with greater precision and standardisation to ensure the production of samples that are as dimensionally identical as

possible. Also, other types of corrosion, such as pitting corrosion, would be interesting to include in future research.

Thermal conductivity tests would also benefit from a standardised and precise sample preparation, which was not available during the production of the thesis. Additionally, the interface samples should be manufactured with more precision by leaving even amounts of both materials on the inspected multi-material.

References

2019 Department of Defense -Allied Nations Technical Corrosion Conference COMPUTATIONAL CORROSION ANALYSIS GUIDES MATERIAL CHOICE FROM DESIGN THROUGH SUSTAINMENT. (n.d.). ResearchGate. Retrieved August 18, 2025, from https://www.researchgate.net/publication/335260941_2019_Department_of_Defense_-Allied_Nations_Technical_Corrosion_Conference_COMPUTATIONAL_CORROSION_ANALYSIS_GUIDES_MATERIAL_CHOICE_FROM_DESIGN_THROUGH_SUSTAINMENT

Bedmar, J., García-Rodríguez, S., Roldán, M., Torres, B., & Rams, J. (2022). Effects of the heat treatment on the microstructure and corrosion behavior of 316 L stainless steel manufactured by Laser Powder Bed Fusion. Corrosion Science, 209, 110777. https://doi.org/10.1016/j.corsci.2022.110777

Chen, J., Yang, Y., Bai, Y., Wang, D., Zhao, C., & Ying Hsi Fuh, J. (2022). Single and multiple track formation mechanism of laser powder bed fusion 316L/CuSn10 multi-material. Materials Characterization, 183, 111654. https://doi.org/10.1016/j.matchar.2021.111654

Chen, J., Yang, Y., Song, C., Zhang, M., Wu, S., & Wang, D. (2019). Interfacial microstructure and mechanical properties of 316L /CuSn10 multi-material bimetallic structure fabricated by selective laser melting. Materials Science and Engineering: A, 752, 75–85. https://doi.org/10.1016/j.msea.2019.02.097

Chen, X., Dong, P., Zeng, Y., Yao, H., & Chen, J. (2024). Effect of heat treatment on the microstructure and properties of CuCrZr prepared by laser powder bed fusion. Materials Characterization, 214, 114103. https://doi.org/10.1016/j.matchar.2024.114103

Chu, F., Zhang, K., Shen, H., Liu, M., Huang, W., Zhang, X., Liang, E., Zhou, Z., Lei, L., Hou, J., & Huang, A. (2021). Influence of satellite and agglomeration of powder on the processability of AlSi10Mg powder in Laser Powder Bed Fusion. Journal of Materials Research and Technology, 11, 2059–2073. https://doi.org/10.1016/j.jmrt.2021.02.015

Deillon, L., Abando Beldarrain, N., Li, X., & Bambach, M. (2024). Coupling hot isostatic pressing and laser powder bed fusion: A new strategy to manufacture defect-free CuCrZr-316L steel multi-material structures. Materials & Design, 241, 112914. https://doi.org/10.1016/j.matdes.2024.112914

Dongfang, K., Fan, H., Sui, S., Li, H., Liu, H., Li, Y., & Liu, P. (2024). Effect of Laser Powder Bed Fusion Process Parameters on the Microstructures, Mechanical Properties, and Conductivity of CuCrZr Alloy. Journal of Materials Engineering and Performance. https://doi.org/10.1007/s11665-024-10026-3

Fathi, P., Rafieazad, M., Mohseni-Sohi, E., Sanjari, M., Pirgazi, H., Shalchi Amirkhiz, B., Ghonchech, M., Nasiri, A., & Mohammadi, M. (2021). Corrosion performance of additively manufactured bimetallic aluminum alloys. Electrochimica Acta, 389, 138689. https://doi.org/10.1016/j.electacta.2021.138689

Han, G., Xie, Z. J., Li, Z. Y., Lei, B., Shang, C. J., & Misra, R. D. K. (2017). Evolution of crystal structure of Cu precipitates in a low carbon steel. Materials & Design, 135, 92–101. https://doi.org/10.1016/j.matdes.2017.08.054

Hemmasian Ettefagh, A., & Guo, S. (2018). Electrochemical behavior of AISI316L stainless steel parts produced by laser-based powder bed fusion process and the effect of post annealing process. Additive Manufacturing, 22, 153–156. https://doi.org/10.1016/j.addma.2018.05.014

Hu, Z., Ma, Z., Yu, L., & Liu, Y. (2023). Functionally graded materials with grain-size gradients and heterogeneous microstructures achieved by additive manufacturing. Scripta Materialia, 226, 115197. https://doi.org/10.1016/j.scriptamat.2022.115197

Huang, G., Wei, K., Deng, J., Liu, M., & Zeng, X. (2022). High-power laser powder bed fusion of 316L stainless steel: Defects, microstructure, and mechanical properties. Journal of Manufacturing Processes, 83, 235–245. https://doi.org/10.1016/j.jmapro.2022.08.066

Ibrahim, K. A., Wu, B., & Brandon, N. P. (2016). Electrical conductivity and porosity in stainless steel 316L scaffolds for electrochemical devices fabricated using selective laser sintering. Materials & Design, 106, 51–59. https://doi.org/10.1016/j.matdes.2016.05.096

Jadhav, S. D., Goossens, L. R., Kinds, Y., Hooreweder, B. V., & Vanmeensel, K. (2021). Laser-based powder bed fusion additive manufacturing of pure copper. Additive Manufacturing, 42, 101990. https://doi.org/10.1016/j.addma.2021.101990

Javaid, M., Haleem, A., Singh, R. P., Suman, R., & Rab, S. (2021). Role of additive manufacturing applications towards environmental sustainability. Advanced Industrial and Engineering Polymer Research, 4(4), 312–322. https://doi.org/10.1016/j.aiepr.2021.07.005

Krasniqi, M., Löffler, F., & Tutsch, R. (2025). Influence of scanning strategies on dimensional accuracy in laser powder bed fusion. Measurement: Sensors, 38, 101840. https://doi.org/10.1016/j.measen.2025.101840

Kuai, Z., Li, Z., Liu, B., Chen, Y., Li, H., & Bai, P. (2023). Microstructure and mechanical properties of CuCrZr/316L hybrid components manufactured using selective laser melting. Journal of Alloys and Compounds, 955, 170103. https://doi.org/10.1016/j.jallcom.2023.170103

Kuai, Z., Li, Z., Liu, B., Chen, Y., Lu, S., Tang, X., & Liu, T. (2022). Selective laser melting of CuCrZr alloy: Processing optimisation, microstructure and mechanical properties. Journal of Materials Research and Technology, 19, 4915–4931. https://doi.org/10.1016/j.jmrt.2022.06.158

Kwok, C. T., Wong, P. K., Man, H. C., & Cheng, F. T. (2009). Effect of pH on corrosion behavior of CuCrZr in solution without and with NaCl. Journal of Nuclear Materials, 394(1), 52–62. https://doi.org/10.1016/j.jnucmat.2009.08.006

Laleh, M., Sadeghi, E., Revilla, R. I., Chao, Q., Haghdadi, N., Hughes, A. E., Xu, W., De Graeve, I., Qian, M., Gibson, I., & Tan, M. Y. (2023). Heat treatment for metal additive manufacturing. Progress in Materials Science, 133, 101051. https://doi.org/10.1016/j.pmatsci.2022.101051

Li, Y., Ma, C., Qin, F., Chen, H., Zhao, X., Liu, R., & Gao, S. (2023). The microstructure and mechanical properties of 316L austenitic stainless steel prepared by forge and laser melting deposition. Materials Science and Engineering: A, 870, 144820. https://doi.org/10.1016/j.msea.2023.144820

Liu, Z. H., Zhang, D. Q., Sing, S. L., Chua, C. K., & Loh, L. E. (2014). Interfacial characterization of SLM parts in multi-material processing: Metallurgical diffusion between 316L stainless steel

and C18400 copper alloy. Materials Characterization, 94, 116–125. https://doi.org/10.1016/j.matchar.2014.05.001

Lodhi, M. J. K., Deen, K. M., Greenlee-Wacker, M. C., & Haider, W. (2019). Additively manufactured 316L stainless steel with improved corrosion resistance and biological response for biomedical applications. Additive Manufacturing, 27, 8–19. https://doi.org/10.1016/j.addma.2019.02.005

Lowrie, W., & Fichtner, A. (2020, January 2). Fundamentals of Geophysics. Cambridge Aspire Website; Cambridge University Press. https://doi.org/10.1017/9781108685917

Mao, S., Zhang, D. Z., Ren, Z., Fu, G., & Ma, X. (2022). Effects of process parameters on interfacial characterization and mechanical properties of 316L/CuCrZr functionally graded material by selective laser melting. Journal of Alloys and Compounds, 899, 163256. https://doi.org/10.1016/j.jallcom.2021.163256

Martendal, C. P., Esteves, P. D. B., Deillon, L., Malamud, F., Jamili, A. M., Löffler, J. F., & Bambach, M. (2024). Effects of beam shaping on copper-steel interfaces in multi-material laser beam powder bed fusion. Journal of Materials Processing Technology, 327, 118344. https://doi.org/10.1016/j.jmatprotec.2024.118344

MDS EOS CopperAlloy CuCrZr. (n.d.). EOS GmbH. Retrieved August 6, 2025, from https://www.eos.info/metal-solutions/metal-materials/data-sheets/mds-eos-copperalloy-cucrzr

Merz, B., Nilsson, R., Garske, C., & Hilgenberg, K. (2023). Camera-based high precision position detection for hybrid additive manufacturing with laser powder bed fusion. The International Journal of Advanced Manufacturing Technology, 125(5), 2409–2424. https://doi.org/10.1007/s00170-022-10691-5

Metallographic Procedures and Analysis – A review. (n.d.). ResearchGate. Retrieved June 11, 2025, from https://www.researchgate.net/publication/307205219_Metallographic_Procedures_and_Analysis_-_A_review

Meyer, I., Messmann, C. O., Ehlers, T., & Lachmayer, R. (2025). Additive manufacturing of multi-material parts – Effect of heat treatment on thermal, electrical, and mechanical part properties

of 316L/CuCrZr. Materials & Design, 252, 113783. https://doi.org/10.1016/j.matdes.2025.113783

Meyer, I., Oel, M., Ehlers, T., & Lachmayer, R. (2023). Additive manufacturing of multi-material parts – Design guidelines for manufacturing of 316L/CuCrZr in laser powder bed fusion. Heliyon, 9(8). https://doi.org/10.1016/j.heliyon.2023.e18301

Nikon SLM Solutions Steel-based Alloys. (n.d.). Retrieved May 13, 2025, from https://nikon-slm-solutions.com/materials/steel/

OLAFSSON, P., SANDSTROM, R., & KARLSSON, Å. (1997). Comparison of experimental, calculated and observed values for electrical and thermal conductivity of aluminium alloys. Journal of Materials Science, 32(16), 4383–4390. https://doi.org/10.1023/A:1018680024876

Reijonen, J., Revuelta, A., Metsä-Kortelainen, S., & Salminen, A. (2024). Effect of hard and soft re-coater blade on porosity and processability of thin walls and overhangs in laser powder bed fusion additive manufacturing. The International Journal of Advanced Manufacturing Technology, 130(5), 2283–2296. https://doi.org/10.1007/s00170-023-12853-5

Riener, K., Albrecht, N., Ziegelmeier, S., Ramakrishnan, R., Haferkamp, L., Spierings, A. B., & Leichtfried, G. J. (2020). Influence of particle size distribution and morphology on the properties of the powder feedstock as well as of AlSi10Mg parts produced by laser powder bed fusion (LPBF). Additive Manufacturing, 34, 101286. https://doi.org/10.1016/j.addma.2020.101286

Salman, O. O., Gammer, C., Eckert, J., Salih, M. Z., Abdulsalam, E. H., Prashanth, K. G., & Scudino, S. (2019). Selective laser melting of 316L stainless steel: Influence of TiB2 addition on microstructure and mechanical properties. Materials Today Communications, 21, 100615. https://doi.org/10.1016/j.mtcomm.2019.100615

Salvan, C., Briottet, L., Baffie, T., Guetaz, L., & Flament, C. (2021). CuCrZr alloy produced by laser powder bed fusion: Microstructure, nanoscale strengthening mechanisms, electrical and mechanical properties. Materials Science and Engineering: A, 826, 141915. https://doi.org/10.1016/j.msea.2021.141915

Schaeffler Aerosint—Multi-Material L-PBF. (n.d.). Schaeffler Aerosint. Retrieved October 6, 2025, from https://aerosint.com/multi-material-3d-printing-bundle/

Sharma, S. K., Singh, A. K., Mishra, R. K., Shukla, A. K., & Sharma, C. (2024). Processing Techniques, Microstructural and Mechanical Properties of Additive Manufactured 316L Stainless Steel: Review. Journal of The Institution of Engineers (India): Series D, 105(2), 1305–1318. https://doi.org/10.1007/s40033-023-00497-4

Simmons, J. C., Chen, X., Azizi, A., Daeumer, M. A., Zavalij, P. Y., Zhou, G., & Schiffres, S. N. (2020). Influence of processing and microstructure on the local and bulk thermal conductivity of selective laser melted 316L stainless steel. Additive Manufacturing, 32, 100996. https://doi.org/10.1016/j.addma.2019.100996

Sundararajan, G., & Roy, M. (2001). Hardness Testing. In K. H. J. Buschow, R. W. Cahn, M. C. Flemings, B. Ilschner, E. J. Kramer, S. Mahajan, & P. Veyssière (Eds.), Encyclopedia of Materials: Science and Technology (pp. 3728–3736). Elsevier. https://doi.org/10.1016/B0-08-043152-6/00665-3

Tang, X., Chen, X., Sun, F., Li, L., Liu, P., Zhou, H., Fu, S., & Li, A. (2022). A study on the mechanical and electrical properties of high-strength CuCrZr alloy fabricated using laser powder bed fusion. Journal of Alloys and Compounds, 924, 166627. https://doi.org/10.1016/j.jallcom.2022.166627

Tang, X., Chen, X., Sun, F., Liu, P., Zhou, H., & Fu, S. (2022). The current state of CuCrZr and CuCrNb alloys manufactured by additive manufacturing: A review. Materials & Design, 224, 111419. https://doi.org/10.1016/j.matdes.2022.111419

Vukkum, V. B., & Gupta, R. K. (2022). Review on corrosion performance of laser powder-bed fusion printed 316L stainless steel: Effect of processing parameters, manufacturing defects, post-processing, feedstock, and microstructure. Materials & Design, 221, 110874. https://doi.org/10.1016/j.matdes.2022.110874

Wallis, C., & Buchmayr, B. (2019). Effect of heat treatments on microstructure and properties of CuCrZr produced by laser-powder bed fusion. Materials Science and Engineering: A, 744, 215–223. https://doi.org/10.1016/j.msea.2018.12.017

Wang, D., Liu, L., Deng, G., Deng, C., Bai, Y., Yang, Y., Wu, W., Chen, J., Liu, Y., Wang, Y., Lin, X., & Han, C. (2022). Recent progress on additive manufacturing of multi-material structures with laser powder bed fusion. Virtual and Physical Prototyping, 17(2), 329–365. https://doi.org/10.1080/17452759.2022.2028343

Wei, C., Zhang, Z., Cheng, D., Sun, Z., Zhu, M., & Li, L. (2020). An overview of laser-based multiple metallic material additive manufacturing: From macro- to micro-scales. International Journal of Extreme Manufacturing, 3(1), 012003. https://doi.org/10.1088/2631-7990/abce04

Wen, Y., Wu, X., Huang, A., Narayan, R. L., Wang, P., Zhang, L., Zhang, B., Ramamurty, U., & Qu, X. (2024). Laser powder bed fusion of immiscible steel and bronze: A compositional gradient approach for optimum constituent combination. Acta Materialia, 264, 119572. https://doi.org/10.1016/j.actamat.2023.119572

Xie, H., Tang, X., Chen, X., Sun, F., Dong, L., Tan, Y., Chu, H., Zhou, H., Liu, P., & Fu, S. (2023). The effect of build orientations on mechanical and thermal properties on CuCrZr alloys fabricated by laser powder bed fusion. Journal of Materials Research and Technology, 23, 3322–3336. https://doi.org/10.1016/j.jmrt.2023.01.218

Ye, H., Wang, X., Niu, J., Xing, S., Yu, W., Liu, T., Nan, Y., Xu, W., Xu, H., Zhou, H., Wu, Y., & Sun, H. (2024). Visualization and simulation investigation of Copper-Nickel alloy and carbon steel galvanic corrosion in marine environment. Journal of Electroanalytical Chemistry, 953, 118013. https://doi.org/10.1016/j.jelechem.2023.118013

Zhou, S., Xie, M., Wu, C., Yi, Y., Chen, D., & Zhang, L.-C. (2022). Selective laser melting of bulk immiscible alloy with enhanced strength: Heterogeneous microstructure and deformation mechanisms. Journal of Materials Science & Technology, 104, 81–87. https://doi.org/10.1016/j.jmst.2021.06.062

Appendices

Appendix 1 Homebrew defect analysis program

A homebrew pixel darkness computing program was created to streamline the analysis of multiple microscope images. At the start of running the program, the user inputs the name of the folder containing the processable images, defines the cropping percentage and sets a preliminary threshold value. The cropping percentage is the proportion by which all processed images are trimmed from the outer borders to reduce the pixel darkness sorting error produced by the dark vignette of microscope images.

The program evaluates the processed images based on the darkness of their pixels. When the program is run, the images are imported from the marked folder, converted into greyscale and their outer borders are cropped based on the inputted cropping percentage value. Each pixel in the greyscale images is then assigned a numerical darkness value from 0, meaning completely black, and 255, meaning completely white. The darkness values found in each image are then plotted into a histogram, which shows the amounts of each of the darkness values in the image. Figure 42 shows an example of a typical histogram.

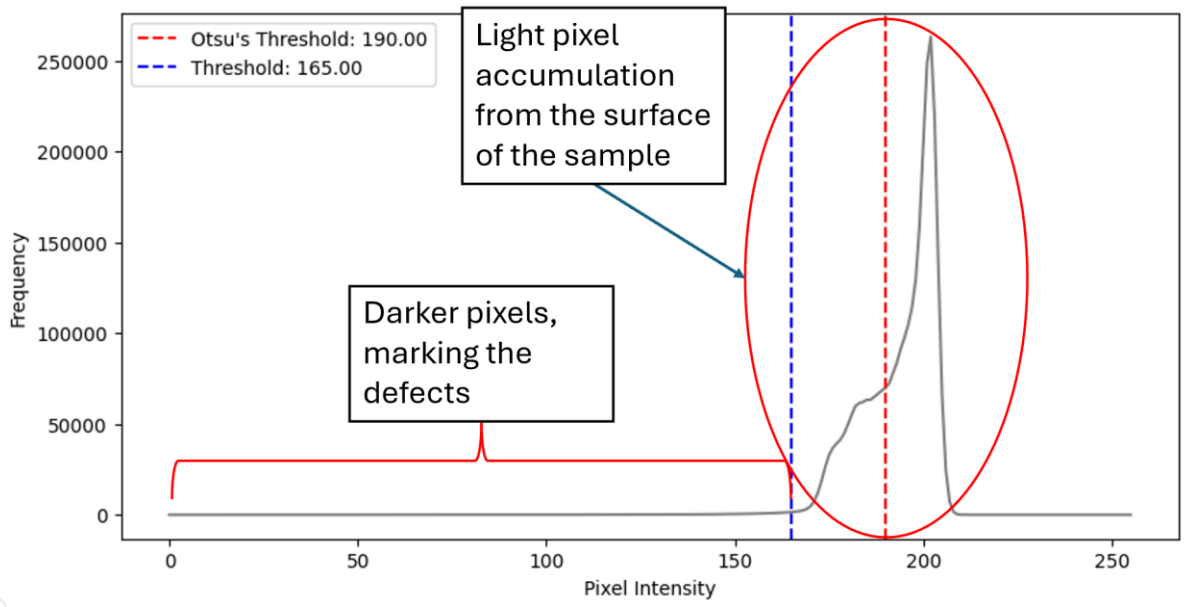

Figure 42. An example pixel intensity histogram, illustrating the lighter pixel accumulation, the intensity range where all the defects likely reside and the manually set and Otsu's threshold values

As Figure 42 shows, the histograms illustrate the frequency of the different pixel intensities, or pixel darknesses. The majority of the microscope images consist of the lighter background of the metal surface, which is seen in the accumulation of pixel intensities in the histogram in the range of 165-210. The pores and other defects are seen as darker pixels below the pixel accumulation. The program also calculates Otsu's threshold and plots it in the histogram. However, Otsu's thresholding method was not seen as suitable for the images in this thesis, as it was consistently calculated in the middle of the accumulation of lighter pixel intensities. Therefore, a threshold value was chosen manually for each image batch and placed below the accumulation of lighter pixels. The chosen threshold value, 165 in the case of the example image, replaces the preliminary threshold value, and the code is run again.

The program produces analysed images as well as different types of graphs. To compare the analysed data with the original microscopic images, the processed grayscale images are exported. To highlight the detected pores, all the pixels which fell under the threshold were colored red. The images are also used to collect numerical data, namely the percentages of the pixels that fall under the threshold value. The program calculates the average percentages of all the images of the same process parameters, post-processing and the imaged materials, and plots the results into a graph. This graph was useful when comparing the different parameter combinations. All of the images and graphs were then exported as JPG files.

Appendix 2 Example calculations of thermal conductivity tests

Electrical resistance measurement was repeated five times on each material by readjusting the clamps to the part. Data on the following aspects were gathered on each measurement:

- Electrical resistance R (Ω)
- The room temperature T (°C)
- The length of the material between the clamps l (mm)
- The width of the tested part w (mm)
- The depth of the tested part d (mm)

The example measured resistances R, lengths between the clamps l, as well as the widths w and depths d of the measured material part, are listed in Table 10.

Table 10. Example values for electrical resistivity calculation

Measurement number n	R [$m\Omega$]	l [mm]	w [mm]	d [mm]
1	0.67	8	5.05	2.7
2	0.59	6.75	5.05	2.7
3	0.70	7.7	5.05	2.7
4	0.62	6.4	5.05	2.7
5	0.64	7.05	5.05	2.7

The average electrical resistivity was calculated using Equation 5, which applies Equation 4 (see Chapter 7.3.5).

$$Average\ \rho\ [\Omega\text{m}] = \left(\frac{\sum \frac{R_n}{l_n}}{5}\right) w * d \tag{5}$$

$$= \left(\frac{\frac{0.67}{8} + \frac{0.59}{6.75} + \frac{0.70}{7.70} + \frac{0.62}{6.4} + \frac{0.64}{7.05}}{5}\right) 5.05 * 2.7 * 10^{-6}$$

$$= 1.23 * 10^{-6}\ \Omega\text{m}$$

Table 11 lists the example ρ, T and L values.

Table 11. thermal conductivity convertion example calculation

Average ρ [Ωm]	$1.23 * 10^{-6}$
T [K]	295
L [ΩWK^{-2}]	$2.41 * 10^{-8}$

The thermal conductivity was calculated using the Franz-Wiedemann law, as shown in Equation 6, which applies Equation 3 (see Chapter 4.5) where the Lorentz number L is multiplied by room temperature T and divided by the average electrical resistivity ρ

$$\lambda = \frac{L\,T}{\rho} = \frac{2.41*10^{-8}*295}{1.23*10^{-6}} = 5.80\ \text{W/mK} \tag{6}$$

All the electrical resistance measurement results (R, l) and their corresponding Average resistivity and Thermal conductivity values are listed in Figure 43.

	As-built 316L		316L HT1		316L HT2	
Measurement number	R[mOhm]	l[mm]	R[mOhm]	l[mm]	R[mOhm]	l[mm]
1	0.67	8.00	0.51	9.95	0.52	8.20
2	0.59	6.75	0.49	7.90	0.58	8.80
3	0.70	7.70	0.50	8.95	0.52	9.30
4	0.62	6.40	0.47	7.70	0.54	9.05
5	0.64	7.05	0.52	9.15	0.52	7.80
A[mm^2]	13.64		16.25		14.75	
Average Resistivity [Ωm]	1.23E-06		8.08E-07		8.66E-07	
Thermal conductivity [W/mK]	5.80		8.81		8.22	

	As-built CuCrZr		CuCrZr HT1		CuCrZr HT2	
Measurement number	R[mOhm]	l[mm]	R[mOhm]	l[mm]	R[mOhm]	l[mm]
1	0.05	8.60	0.01	9.00	0.01	8.50
2	0.04	8.40	0.01	8.65	0.01	9.00
3	0.05	9.05	0.01	7.60	0.01	7.25
4	0.05	9.40	0.01	9.40	0.01	7.70
5	0.05	8.35	0.01	8.80	0.01	7.45
A[mm^2]	12.76		27.32		21.29	
Average Resistivity [Ωm]	6.89E-08		2.32E-08		2.15E-08	
Thermal conductivity [W/mK]	103.24		306.93		330.41	

	As-built Interface		Interface HT1		Interface HT2	
Measurement number	R[mOhm]	l[mm]	R[mOhm]	l[mm]	R[mOhm]	l[mm]
1	0.23	5.35	0.26	7.50	0.14	5.05
2	0.23	6.40	0.26	7.55	0.15	6.05
3	0.23	5.20	0.29	8.00	0.16	6.80
4	0.25	6.70	0.26	6.85	0.15	6.35
5	0.25	6.20	0.28	7.80	0.16	6.35
A[mm^2]	12.00		13.30		11.78	
Average Resistivity [Ωm]	4.85E-07		4.82E-07		3.35E-07	
Thermal conductivity [W/mK]	14.67		14.75		21.25	

Figure 43. All the results of the resistance and length measurements, and their corresponding electrical resistivity and thermal conductivity values. *R*=resistance, *l*=distance between the clamps, *A*=area of the sample surface perpendicular to the *l*.